INFORMATION TO USERS

This manuscript has been reproduced from the microfilm master. UMI films the text directly from the original or copy submitted. Thus, some thesis and dissertation copies are in typewriter face, while others may be from any type of computer printer.

The quality of this reproduction is dependent upon the quality of the copy submitted. Broken or indistinct print, colored or poor quality illustrations and photographs, print bleedthrough, substandard margins, and improper alignment can adversely affect reproduction.

In the unlikely event that the author did not send UMI a complete manuscript and there are missing pages, these will be noted. Also, if unauthorized copyright material had to be removed, a note will indicate the deletion.

Oversize materials (e.g., maps, drawings, charts) are reproduced by sectioning the original, beginning at the upper left-hand corner and continuing from left to right in equal sections with small overlaps. Each original is also photographed in one exposure and is included in reduced form at the back of the book.

Photographs included in the original manuscript have been reproduced xerographically in this copy. Higher quality 6" x 9" black and white photographic prints are available for any photographs or illustrations appearing in this copy for an additional charge. Contact UMI directly to order.

U·M·I

University Microfilms International
A Bell & Howell Information Company
300 North Zeeb Road, Ann Arbor, MI 48106-1346 USA
313/761-4700 800/521-0600

Order Number 9207088

Positron transport in solids and the interaction of positrons with surfaces

Kong, Yuan, Ph.D.

City University of New York, 1991

U·M·I
300 N. Zeeb Rd.
Ann Arbor, MI 48106

A

POSITRON TRANSPORT IN SOLIDS
AND
THE INTERACTION OF POSITRONS WITH SURFACES

by

Yuan Kong

A dissertation submitted to the Graduate Faculty in Physics in partial fulfillment of the requirements for the degree of Doctor of Philosophy, The City University of New York.

1991

This manuscript has been read and accepted for the Graduate Faculty in Physics in satisfaction of the dissertation requirement for the degree of Doctor of Philosophy.

9/24/91
Date

Martin Kramer Martin A. Kramer
Chair of Examining Committee

9/26/91
Date

Joseph Kreiger Joseph Kreiger
Executive Officer

Joseph L. Birman Joseph L. Birman

Kelvin G. Lynn Kelvin G. Lynn

Marvin Mittleman Marvin Mittleman

Myriam P. Sarachik Myriam P. Sarachik
Supervisory Committee

The City University of New York

Abstract

Positron Transport in Solids and the Interaction of Positrons with Surfaces

by

Yuan Kong

Supervisor: Kelvin G. Lynn

In studying positron transport in solids, a two-stream model is proposed to account for the epithermal positrons. Thus positron implantation, thermalization, and diffusion processes are completely modeled. Experimentally, positron mobility in thermally grown SiO_2 is measured in a sandwiched structure by using the Doppler broadening technique. Positron drift motion and the electric field configuration in a Si surface buried under overlayers are measured with the positron annihilation γ-ray centroid shift technique. These studies are not only important in measuring positron transport and other properties in complicated systems, they are also of practical significance for material characterizations.

In studying positron interactions with surfaces, a multiple-encounter picture is proposed of thermal positrons participating in the surface escape processes. Positron trapping into the surface image potential is also studied considering the long range nature of the image potential. Experimentally, the positron annihilation induced Auger electron spectroscopy (PAES) is used to study an ionic insulator surface KCl(100). Temperature dependent as well as positron energy dependent measurements are carried out. The experimental evidence suggests that the Auger electrons are possibly associated with positrons bound to Cl ions in the near surface region. The surface sensitivity and the non-destructiveness of the PAES technique are also examined for measuring the KCl(100) surface sputtering damage and the annealing behavior.

Acknowledgement

I wish to express my sincere gratitude to my supervisor Dr. Kelvin Lynn for his excellent direction and inspiring encouragement, which have been instrumental in fostering my approach and affection for physics. Thanks are also due to him for his concern for my general welfare. Professor L.O. Roellig is gratefully thanked for introducing me to the wonderful institution of Brookhaven National Laboratory, and for his kind help during my stay here. Professor R.M. Nieminen and Dr. A. Walker are thanked for their hospitality and many discussions during my visits to the Helsinki University of Technology and the University of East Anglia. In the last three exciting years at Brookhaven, I have greatly benefited from the interactions with Drs. A. Schwab, J. Throwe, B. Nielsen, A. Vehanen, A. Weiss, M. Weber, and K.F. Canter as well as my fellow students. The daily support from Eileen Morello, Mike Carroll (gravity waves), Don Baker, Harry Hacker, and Marilyn McKeown will always be remembered.

As a CUSPEA student, I wish to extend my many thanks to Professor T.D. Lee of Columbia University for sponsoring the program, and Professor Qin Ming Hua of Tsinghua University in helping me to succeed in the first phase of CUSPEA. The two years at the City College of New York have also been my most enjoyable times through the interactions with the professors and the students there.

Finally, for making my goals part of their life, I am indebted to my wife Xue Ning and my parents Mei Ping and Guang Gin Kong. I shall forever treasure their love, faith and patience for me during these years.

This work was supported by the U.S. Department of Energy, Office of Basic Energy Research under Contract No. DE-AC02-76CH00016.

To my wife

Xue Ning and

our newborn baby

Daniel.

Table of Contents

Abstract iii

Acknowledgement iv

Table of Contents vi

List of Tables viii

List of Figures ix

Chapter 1: Introduction 1

§1.1 Historical Backgrounds 1

§1.2 Positron Transport in Solids 10

§1.3 Positron Interaction with Surfaces 23

Chapter 2: Experimental 33

§2.1 The Slow Positron Beam 33

2.1.1 General Descriptions 33

2.1.2 The Cone-geometry Positron Energy Moderator 38

2.1.3 The Magnetic Transport of Positron beams 41

2.1.4 Signal Detection in Positron Experiments 43

2.1.5 Sample Preparation and Treatment in PAES 47

2.1.6 An Apparatus for Variable Energy Positron Lifetime Measurement 48

§2.2 Data Acquisition and Analysis 61

2.2.1 The Computer Interfacing System 61

2.2.2 Data Analysis in Positron Transport and PAES Measurements 64

2.2.3 The Maximum Entropy Deconvolution 68

Chapter 3: Positron Transport in Solids 81

§3.1 Transport Model of Thermal and Epithermal Positrons in Solids 81

3.1.1 Two-level and Two-stream Model of Positron Transport 82
3.1.2 Many-level and Two-stream Model of Positron Transport 93
3.1.3 Application to Metal Bilayer Systems 101
§3.2 Measurement of Positron Mobility in Thermally Grown SiO_2 108
§3.3 Centroid Shift Measurement of Positron Transport at a Si Surface 116
Chapter 4: Positron Interaction with Surfaces 127
§4.1 The Multiple-encounter of Thermal Positrons with Surfaces 127
§4.2 Positron Trappings into the Surface Image-Potentials 133
4.2.1 Positron Rydberg-like States at Surfaces 136
4.2.2 Trapping through the Electron-hole and Phonon Processes 138
4.2.3 Results and Discussions 140
§4.3 PAES Study of KCl(100) Surface 145
4.3.1 The Experimental Aspects 146
4.3.2 Positron Incident Energy Dependent Measurements 147
4.3.3 Temperature Dependent Measurements 154
4.3.4 Discussions and Conclusions 156
§4.4 Positron Study of Ion Sputtering Damage of KCl(100) surface 166
4.4.1 The Experimental Aspects 166
4.4.2 Results and Discussions 170
Chapter 5: Summary 180
References 184

List of Tables:

Table 4.1 141

List of Figures:

Fig.1.1 The energy and angular relation of the positron annihilation γ-rays 3

Fig.1.2a and b Schematics and examples of ACAR and DB measurements 4

Fig.1.2c Positron lifetime measurements 6

Fig.1.3 Energy distribution of positrons after moderation and from β-decay 8

Fig.1.4 The energy distribution of γ-rays from the Ps decay 14

Fig.1.5 Measurements of thermal positron diffusion coefficients in metals 16

Fig.1.6 Measurements of positron internal surface reflection 17

Fig.1.7 Schematics of positron surface processes 24

Fig.1.8 Schematics of the principle of PAES 31

Fig.2.1 Schematics of the PAES beam 34

Fig.2.2 UHV system for the PAES experimental chamber 37

Fig.2.3 Na^{22} decay scheme; β^+ particle energy distributions; and schematics of the cone-geometry moderator 40

Fig.2.4 $E \times B$ energy dispersion system 46

Fig.2.5 Positron lifetime set-up and the electronics for data acquisition 49

Fig.2.6 Afterpulsing correction circuit for the PMT signal 53

Fig.2.7 An example of measured positron lifetime spectrum 55

Fig.2.8 Lifetime spectrum with 90 Gauss magnetic field 55

Fig.2.9 Lifetime spectrum when secondary electrons are accelerated by 10 V ... 57

Fig.2.10 Secondary electrons are not accelerated 57

Fig.2.11 CEMA count rate vs sample bias 58

Fig.2.12 Schematics for the computer interfacing 62

Fig.2.13 PAES spectra for the Cl(LMM) 181 eV Auger electrons 67

Fig.2.14 Example 1 of positron annihilation γ-ray energy peak 75

Fig.2.15 Example 2 of positron annihilation γ-ray energy peak 75

Fig.2.16 Residual of the deconvoluted spectrum vs the original spectrum 77
Fig.2.17 Difference spectrum of example 1 and 2 before deconvolution 79
Fig.2.18 Difference spectrum of example 1 and 2 after deconvolution 79
Fig.3.1 Fraction of positrons returning to the surface 90
Fig.3.2 Ratio of epithermal positron current to total positron current 92
Fig.3.3 Thermalizaed positron fraction vs positron incident energy 92
Fig.3.4 Source profiles for a three-level model 99
Fig.3.5 Reemitted positron fractions for a three-level model 99
Fig.3.6 Experimental data corresponding to a three-level model 100
Fig.3.7 Schematics of a bimetallic structure 102
Fig.3.8 Epithermal positron currents from a bilayered system for different thicknesses of the overlayers 105
Fig.3.9 Thermal positron current from a bilayered system for different thicknesses of the overlayers 105
Fig.3.10 The differences of reemitted positron fractions 107
Fig.3.11 Comparison of an exponential and a derivative Gaussian profile 107
Fig.3.12 Schematics of a MOS structure 109
Fig.3.13 Measurement of S-parameter as a function of gate biasing 114
Fig.3.14 Model calculation of S-parameter vs gate biases 114
Fig.3.15 The centroid shift vs positron incident energy for the n-type MOS 120
Fig.3.16 The centroid shift vs positron incident energy for the p-type MOS 120
Fig.3.17 Model calculation for centroid shifts vs positron incident energy 123
Fig.4.1 Measurements of positrons trapping at Ag(111) surface 134
Fig.4.2 The surface potential for calculating the positron surface trapping 137
Fig.4.3 Electron-hole trapping rate 142
Fig.4.4 Phonon mediated trapping rate into the n=2 state 143

Fig.4.5 Schematics of a two-stage trapping model.....143
Fig.4.6 Positron incident energy dependent measurements of KCl(100) 148
Fig.4.7 Transformation of the energy-dependent features 151
Fig.4.8 The temperature-dependent measurement.....155
Fig.4.9 Surface contamination effects in the temperature dependence of PAES 157
Fig.4.10 Model calculation of positron energy difference in solid and at surface vs positron workfunctions.....160
Fig.4.11 The PAES spectra for damaged KCl(100) surface 171
Fig.4.12 The time-dependent annealing behavior of KCl(100) surface when ion sputtering energy is 400 eV.....175
Fig.4.13 The time-dependent annealing behavior of KCl(100) surface when ion sputtering energy is 2 keV.....177
Fig.4.14 The temperature-dependent defects annealing behavior 179

Chapter 1
INTRODUCTION

§1.1 Historical Background

Positron solid state physics started more than 40 years ago when DeBenedetti et al (1949) discovered that the two emitted γ-rays from a positron annihilation with an electron in solids were not exactly colinear. Thereafter, this field grew rapidly and the positron technique has been established as an unique probe for studying the many aspects of condensed matter (see, e.g., West, 1973, for a general review of positron solid state physics before the advent of positron beams). The positron can be a stable probe of solids since its annihilation time ($\sim 10^2$ ps) is much longer than the characteristic times of electronic ($\sim 10^{-4}$ ps), or ionic ($\sim 10^{-2}$ ps) processes in the solids. Energetic positrons will thermalize in solids (Kubica and Stewart, 1975) in a matter of pico-seconds, and they have negligible momenta at annihilations compared with their electron counterparts. In the center-of-mass system of the annihilating positron-electron pair, the two annihilation γ-rays will be emitted 180° from each other, with exactly the same energy E_{CM}

$$E_{CM} = m_0 c^2 - \epsilon_B/2, \tag{1.1}$$

where m_0 is the rest mass of the positron or electron, c is the speed of light, and ϵ_B is the binding energy of the positron-electron pair before annihilation.

In the laboratory system, the center-of-mass system will be moving at half of the annihilating electron velocity (v_-) neglecting the thermal positron contribution to the center-of-mass momentum. The γ-rays from the annihilation will no longer

be colinear nor will they possess the same energy in the laboratory system because of the Doppler shift effect. In the laboratory system, the two annihilation photons will possess energies E_1 and E_2, and angles θ_1 and θ_2 with respect to the direction of $\mathbf{v}_-$ (fig.1.1). They are evaluated as (West, 1973)

$$E_{1,2} = E_{CM}(1 \pm v_- \cos\theta_0/2c)/(1 - v_-^2/4c^2)^{1/2}, \tag{1.2}$$

and

$$\cot\theta_{1,2} = (\cos\theta_0 \pm v_-/2c)/[(1 - v_-^2/4c^2)^{1/2}\sin\theta_0], \tag{1.3}$$

where θ_0 is the angle of the emitted photons with respect to $\mathbf{v}_-$ in the center-of-mass system.

Since v_-/c is usually of the order 10^{-2} for most solids, (1.2) and (1.3) can be simplified, from which the angular deviation ($\delta\theta$) and energy difference (δE) of the two annihilation photons are obtained

$$\delta\theta = \theta_1 - \theta_2 \approx \frac{p_t}{m_0 c}, \tag{1.4}$$

$$\delta E = E_1 - E_2 \approx cp_l, \tag{1.5}$$

where p_t, p_l are the annihilating electron momentum components transverse to and along the emission direction of the annihilation photons.

Figs.1.2a and 1.2b show the two positron techniques that have been developed based on observing the angular deviation from colinearity and the energy shifts of the annihilation γ-rays. The angular correlation of the annihilation radiation (ACAR) technique makes use of two photon detectors to measure the two annihilation photons in coincidence when evaluating $\delta\theta$. The Doppler broadening (DB) lineshape measurement makes use of one or two photon detectors in observing the

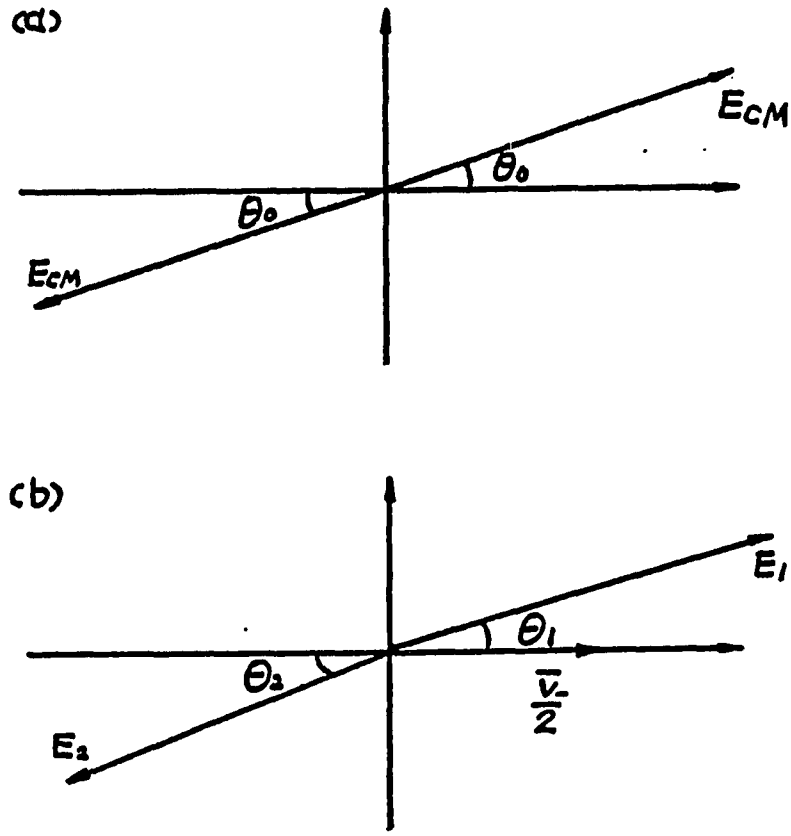

Fig.1.1 Schematics of the energy and angle relations of two annihilation γ-rays a) in the center-of-mass system of the annihilating positron-electron pair, and b) in the laboratory system.

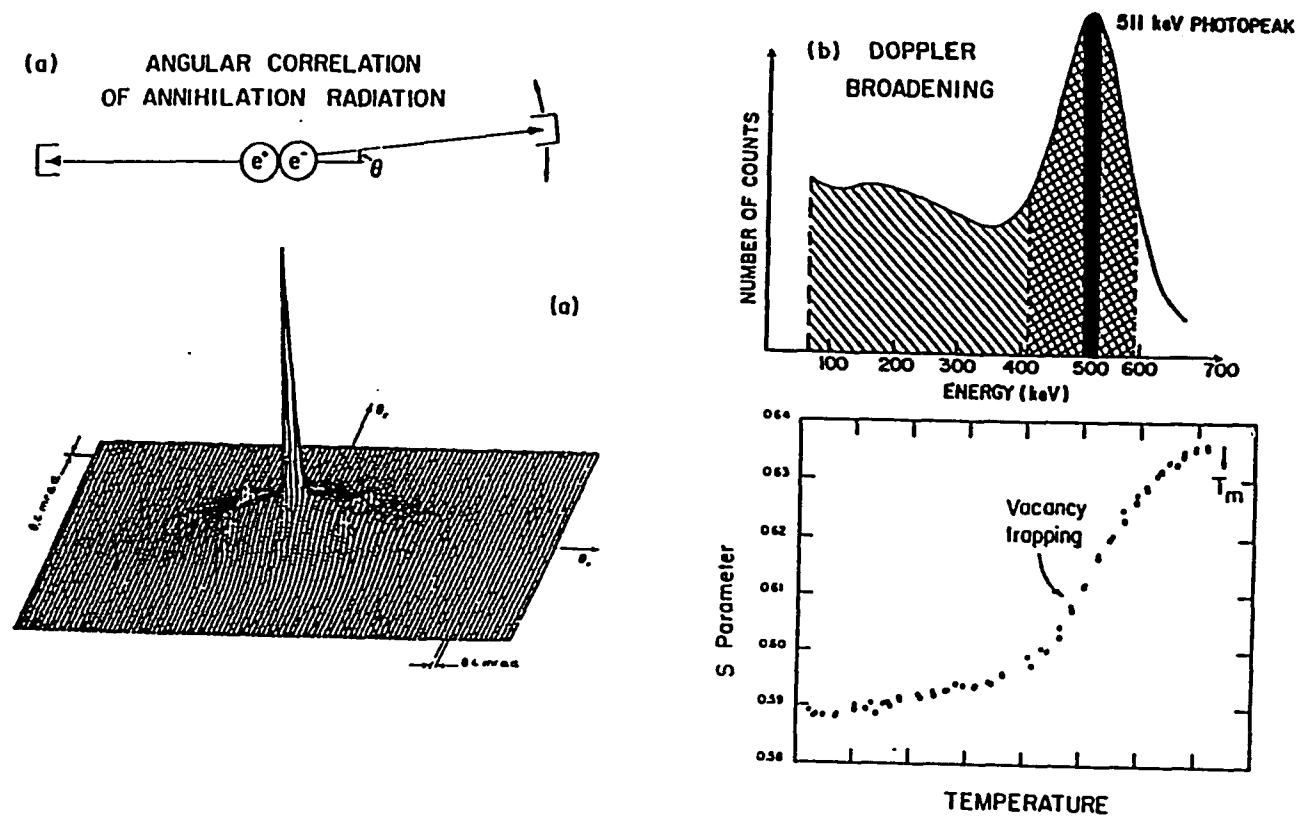

Fig.1.2 Schematics of the conventional positron techniques: a)ACAR, where a 2D-ACAR measurement of quartz sample is shown; b) Doppler broadening S-parameter, where a measurement of CuZn thermal vacancy generation is shown.

energy spectra of the annihilation photons. This lineshape is usually characterized by the so-called S-parameter which qualitatively indicates the width of the electron momentum distributions. The S-parameter is defined as the ratio of the darkened region with the crosshatched region in fig.1.2b. Examples of ACAR and DB measurement results are also shown in fig.1.2a and 1.2b: the two dimensional ACAR data is from a single crystal quartz (Manuel, 1983); the DB data is from a case of thermal vacancy generation in CuZn alloy (Schultz and Lynn, 1988).

The ACAR and DB techniques measure the electron momentum distribution in the solids. There is yet another well-developed positron technique popular for material characterizations, i.e., the positron annihilation lifetime measurement which is sensitive to the electronic spatial density. For example, positron lifetimes τ in free-electron-like metals are given empirically as (Brandt, 1983)

$$\tau \approx \frac{r_s^3}{2(16+r_s^3)} ns, \tag{1.6}$$

where r_s is related to the electron density n and Bohr radius a_0 as $(3/4\pi n)^{1/3}/a_0$, ranging from 2.07 for Al to 5.62 for Cs. Positron lifetimes vary consequently from $\sim$ 163 ps for Al to 418 ps for Cs. Fig.1.2c shows the positron lifetimes in free-electron-like metals as a function of r_s.

The positron techniques described above are mostly probing bulk solids, because the positrons utilized are from the β-decays of radioisotopes with energies of several hundreds keV, and they will penetrate the solids deeply up to the millimeter range (Brandt and Paulin, 1977). Information is obtained only after positron annihilations with the host electrons through the annihilation γ-rays. Thus it is difficult to envisage further possibilities of positron solid state physics. It was hoped almost from the beginning that the positron energies would be variable (Madanski and

(c) LIFETIME

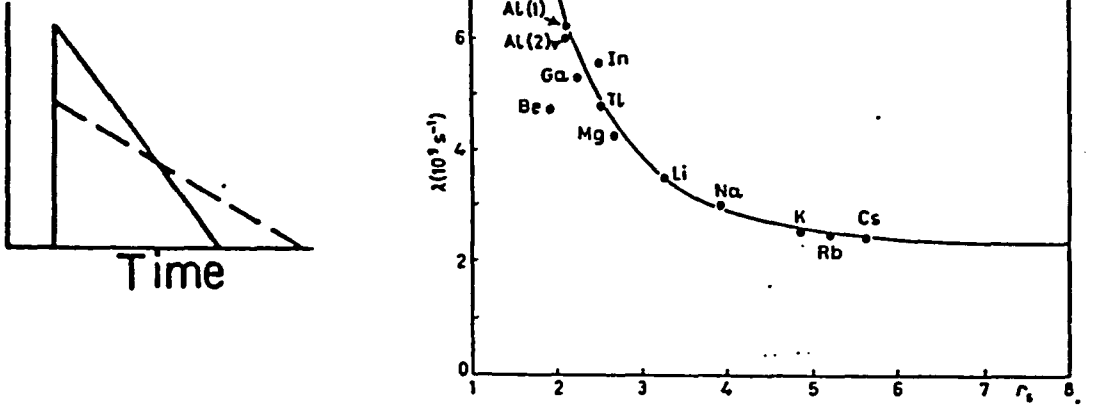

Fig.1.2c) Positron lifetime, where the positron lifetime as a function of the electron gas density r_S is shown.

Rasetti, 1950), but it was only about 30 years later that practical positron energy moderators were developed to enable the construction of slow positron beams (Mills, 1978; Lynn, 1979). Fig.1.3 shows the energy distribution of moderated positrons vs positron energy distributions from the radioisotope Co^{58}.

The fundamental principle of the solid state positron moderator relies on the fact that fast positrons will slow down in solids and reemit into vacuum with a much narrower energy distribution. The positron reemission from solids is made possible either due to the *negative* positron workfunctions on many metal or semiconductor surfaces (Tong, 1973); or in case of rare gas solids(Mills and Gullikson, 1986), it is due to the inefficient energy loss channels in the solids, so that positrons can still be sufficiently energetic to escape the solids before they come to equilibrium or annihilate in solids. Other methods, such as the β-ray spectrometer (Ito et al, 1980) have also been examined for producing mono-energetic positron beams, but the solid state moderator still provides the best efficiency available.

The positron energy moderation process is characterized by the moderation efficiency. This quantity is defined as the number of slow positrons escaping the moderator divided by the number of positrons emitted by the radioisotope. It should be noted that this figure of merit also includes the effects of the self-adsorption of the source, and source-moderator geometry. The first effort in generating slow positrons attained an efficiency of 10^{-8}(Cherry, 1958). A practical efficiency of 10^{-5}(Canter et al, 1972) was not realized until the development of MgO coated moderator. Over the last ten years, there have been many efforts in improving the moderation efficiency for the ever-expanding applications of slow positron beams. The rare gas solid Ne moderator currently provides the best efficiency of $\sim 5 \times 10^{-3}$ (Khatri et al, 1990).

The development of slow positron beams in the late 1970s provided exciting

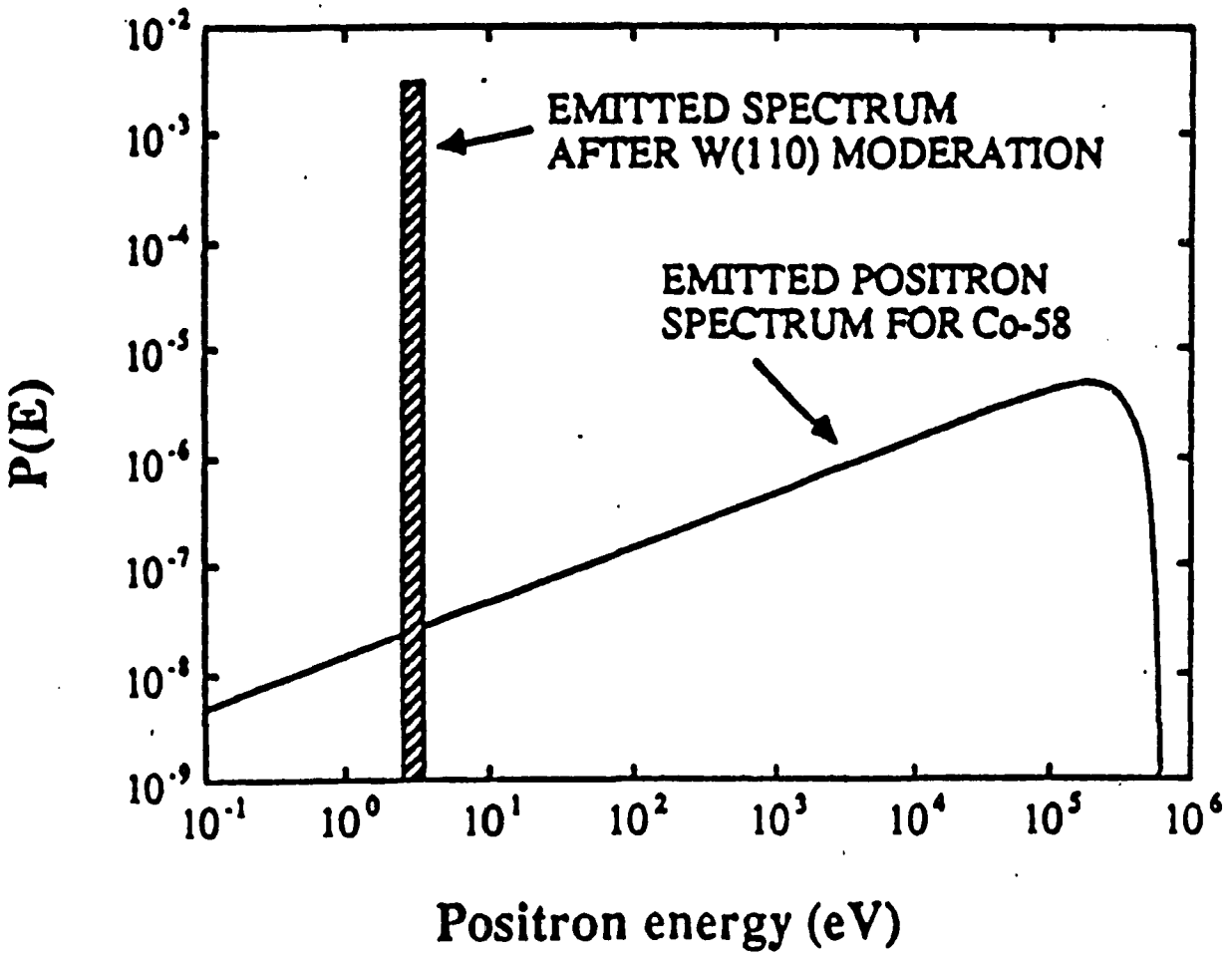

Fig.1.3 Schematics of β^+ particle energy distribution from Co^{58} and the moderated positron energy distributions.

possibilities for new experiments. Much progress has already been made in the last decade in advancing the knowledge of positron solid state physics (Schultz and Lynn, 1988). On the one hand, the basic processes of slow positron interactions with solids have been well studied both experimentally and theoretically. Examples include positron slowing down in solids (Mills and Wilson, 1982; Valkealahti and Nieminen, 1984); epithermal positron effects (Nielsen et al, 1987; Kong and Lynn, 1990); and thermal positron processes at solid surfaces (Nieminen and Oliva, 1980). On the other hand, the positron technique itself has been increasingly refined and its applications expanded. As a direct extension but with much more versatile capabilities, the existing bulk techniques are combined with slow positron beams. We have seen variable energy 2D-ACAR measurement of positron surface states (Lynn et al, 1985); variable energy positron lifetime measurement of defect depth-distributions (Schödlbauer et al, 1987); and many surface and interface studies carried out with the energy turnable Doppler broadening measurement (e.g., Schultz et al, 1988). Unique positron probes have also been established which can provide information otherwise difficult to obtain: for example, low energy positron diffraction (LEPD) (Canter, 1991) has been demonstrated to be superior over low energy electron diffraction (LEED) in a recent measurement of compound semiconductor CdSe surface; reemitted positron energy loss spectroscopy (REPELS) showed its promise of identifying the vibrational energy losses at surfaces (Fischer et al, 1986); positron microscopes have been developed which may facilitate studies such as the spatial distributions of monovacancies (Brandes et al, 1988); another technique that the present thesis will be discussing is the positron annihilation induced Auger electron spectroscopy (PAES) (Weiss et al, 1988). PAES provides a highly surface sensitive probe without the secondary electron background such as found in the electron collisionally induced Auger electron spectroscopy (EAES).

In this thesis, we will focus on the slow positron technique. Our study will be concerned with positron transport in solids and their interactions with surfaces. The background and motivation for the present thesis researches will be introduced in the next two sections.

§1.2 Positron Transport in Solids

Slow positron beams have been widely applied towards the near-surface inhomogeneties studies (Lynn, 1983). In contrast to the positron studies carried prior to the 1970s, the variable energy positron technique provides a depth-profiling capability which can be utilized in studying defects distributions, or the interfaces of multilayered structures. Quantitative knowledge about the bulk inhomogeneties probed by slow positron techniques, however, depends to a large extent on the understanding of the positron implantation processes into the solids and their subsequent transport in relation to the defects, surfaces, and interfaces. During the last decade, the widely adopted approach has been, first, to obtain an energy dependent stopping profile for the assumed thermalized positrons, and then to model their subsequent transport by a diffusion approximation. We shall refer to this approach hereafter as the "implantation-diffusion" model.

Positrons of several hundreds or thousands electron volts will initially experience inelastic energy losses at a rate of $dE/dt \sim 10^{17}$ eV/sec due to ionizations, and to collective and quasi-particle excitations (Nieminen, 1983). In insulators, exciton formation and Ps formation also play an important role at the lower energy range for positrons slowing down to a few eV. The time scale for this process is on the order of 10^{-13} seconds with positrons of primary energy E (keV) traversing a mean depth (Mills and Wilson, 1982)

$$x_i = \frac{A}{\rho} E^{1.6} \text{Å}, \tag{1.7}$$

where $A \sim 350$, ρ is the target density in g/cm^3.

At a few electron volts, in addition to quasi-particle scatterings, positron-phonon scattering becomes important for positrons to reach thermal equilibrium with the solids (Perkins and Carbotte, 1970). A typical time scale for thermalization is $\sim 10^{-12}$seconds, and positrons have traversed a path of 10^2Å.

Experimentally, a positron stopping profile has to be assumed for interpreting slow positron measurements. Many efforts have been devoted towards evaluating this positron stopping profile in solids. A derivative Gaussian distribution

$$P(x) = \frac{2x}{x_i^2} \exp[-(x/x_i)^2], \tag{1.8}$$

is agreed to give the best approximate description. This agreement was obtained from Monte Carlo simulations (Valekealahti and Nieminen, 1984), as well as from experimental evidence (Vehanen et al, 1987). Some recent theoretical simulations and experiments, however, indicated deviations from eq.(1.8) (Baker et al, and references therein, 1991).

The interpretation of slow positron beam experiments often assumes that the "stopped" positrons described by eq.(1.8) are completely thermalized. The energy spread of the thermalized positrons obeys the Maxwell-Boltzman distribution (Bergersen and Pajanne, 1974; Fischer et al, 1986). Their subsequent transport in solids is described by a one-dimensional diffusion equation

$$D_+ \frac{d^2 n_t(x)}{dx^2} - \lambda_{eff} n_t(x) + P_t(x) = 0, \tag{1.9}$$

where D_+ is the thermal positron diffusion coefficient, $n_t(x)$ is the steady-state thermal positron spatial distribution, λ_{eff} is the sum of the positron annihilation

and trapping rate in bulk solids, and $P_t(x)$ is the thermal positron spatial distribution at time zero, which is given by eq.(1.8) in the implantation-diffusion model. For clean metals, the time scale for the diffusion is $\sim 10^{-10}$seconds with a diffusion length $L_{eff} = \sqrt{D_+/\lambda_{eff}} \sim 10^3$Å. The equilibrium positron states are delocalized Bloch-like waves in most metals and semiconductors.

Theoretically, the average angular deflection for thermal positrons was calculated to be about 120°(Nieminen and Oliva, 1980), thus a random-walk model can be applied to positron transport in solids over long time scales. The validity of the random walk model thus requires that the positron penetration depth is much larger than the elastic mean free path. The diffusion length should also be smaller than this penetration depth in order for the diffusion approximation to be valid in a semi-infinite medium. According to the semiclassical argument for electron transport in solids (Aschcroft and Mermin, 1976), the uncertainty principle is not considered to be violated if the accuracy for specifying the momentum and position does not exceed that required by the uncertainty principle. The wave character of the positrons would limit the accuracy of evaluating the thermal positron spatial distribution to its de Brogile wavelength value. This wavelength at temperature T (K) is $\sim 62\text{Å}\sqrt{300/\text{T}}$ (Brandt, 1983), which can be compared to the positron implantation depth of 10^3Å. The classical diffusion equation (1.9) should be accepted only as a phenomenological description of a host of positrons moving in solids. The extracted results from the implantation-diffusion model with depth resolutions exceeding that of positron de Brogile wavelengths should be viewed with caution. One point which should be noted here is that for positrons trapped into spatially localized states, the limits derived from the uncertainty principle are less stringent than for spatially extended delocalized positrons. The practice of depth-profiling the defects distribution with slow positrons is thus justified in most circumstances.

With the obtained positron implantation profile and proper boundary conditions, the diffusion equation (1.9) can be solved to obtain the fraction of positrons returning to the surface. Experimentally, this fraction can be deduced from, e.g., the 3-γ decay of the positron-electron bound state, i.e., the positronium (Ps). Ps can only form on the surfaces of most metals and semiconductors but not in their bulks, thus Ps provides signals of positrons returning to the surfaces.

The 3-γ decay mode is actually attributed to the triplet state Ps, also referred to as ortho-Ps (o-Ps). The lifetime of o-Ps in vacuum is 142 ns, and its predominant 3-γ decay mode is due to the conservation of charge conjugation. The energy distribution of the o-Ps annihilation γ-rays ranges from 0 up to 511 keV as shown in fig.1.4a because of the 3-body interactions involved. Ps may also form in the singlet state with a lifetime of 125 ps in vacuum, and decay predominantly via the 2-γ decay mode. The singlet state Ps is also referred to as para-Ps (p-Ps) and is one-third of the o-Ps fraction in vacuum.

By studying the fraction of Ps (fig.1.4b) formed at the metal or semiconductor surfaces as a function of positron implantation energies, positron transport and trapping properties in solids can be studied. Assuming a total absorbing boundary condition at the surface, the fraction of positrons returning to the surface is (Schultz and Lynn, 1988)

$$F_s = [1 - \pi^{1/2}\sigma_g \exp(\sigma_g^2)\mathrm{erfc}(\sigma_g)] \tag{1.10}$$

where $\sigma_g = x_i/2L_{eff}$, and erfc is the complementary error function.

There are, however, some inconsistencies between theoretical predictions and experimental results evaluated with the implantation-diffusion model. For example, in the deformation potential and long-wavelength approximations, positron diffusion

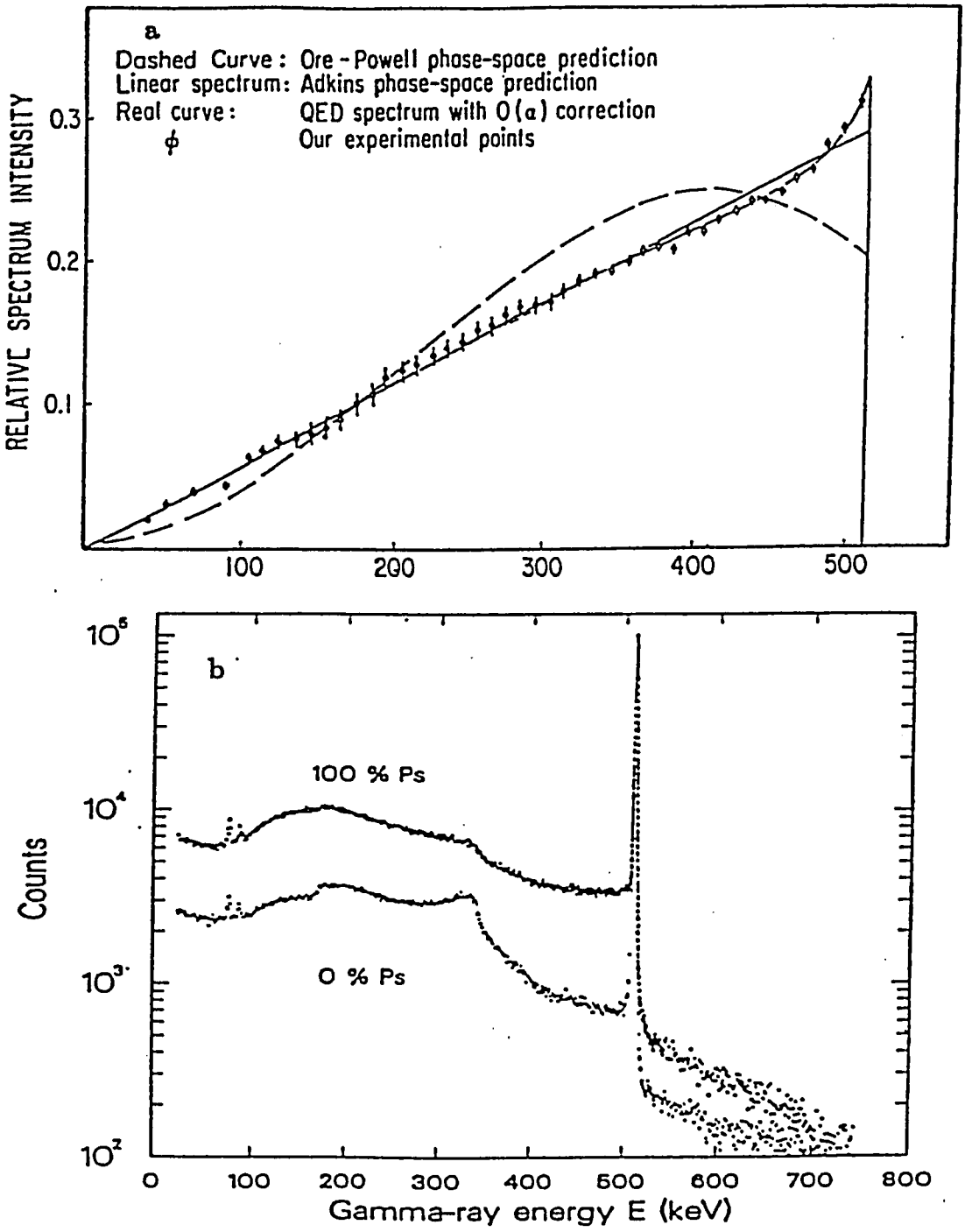

Fig.1.4 a) The energy distribution of γ-rays from the o-Ps 3-γ decay; b)annihilation γ-ray energy distribution measured with a Ge detector when there is zero and 100% Ps formation.

in clean metals should be governed by acoustic phonon scattering, introducing a temperature dependence $D_+ \propto T^{-1/2}$ (Bergersen et al, 1976). Initial experimental results (fig.1.5a), however, indicated no such temperature dependence for a variety of metals. The temperature exponent can not be consistently described by a single value over the measured temperature range, and it varied from -0.68 at an Al(110) surface to -2.6 at a Cd($11\bar{2}0$) surface (Schultz et al, 1985). Another example is that thermal positrons returning to the surface can be reflected back to bulk solids by the positron surface potentials (Nieminen and Oliva, 1980). The experimental measurements shown in fig.1.6a again disagreed with this theory assertion, where Ps fraction indicating the probability of positrons returning to surfaces levels at low temperatures instead of approaching zero, as shown by the solid line.

These inconsistencies have been discussed in many contexts. Possibilities for more complicated positron scattering channels are suggested (Singh et al, 1989). Inelastic scattering of positrons at the surface potential was also proposed to explain the finite Ps fraction at decreasing temperatures (Wilson, 1983). Huomo et al (1987) and more recently, Soininen et al (1990) arrived at a better agreement with theory predictions for positron transport in metals. They argued that part of the implanted positrons at low primary energies can escape the solids before they come to equilibrium with the host solids , the measured Ps fraction or other parameters are thus not totally due to thermalized positrons returning to the surfaces. In their data analysis, only the higher($\geq$ 4 keV) energy positron measurements are considered with the implantation-diffusion model. Thus obtained D_+ is proportional to $T^{-0.4} - T^{-0.6}$ consistently over the measured temperature ranges for several metals (fig.1.5b). With the same data analysis method, experiment also indicated that the theoretically predicated total reflection of positrons at the surface potential does occur as $T \rightarrow 0K$ (Britton et al, 1989) as shown in fig.1.6b.

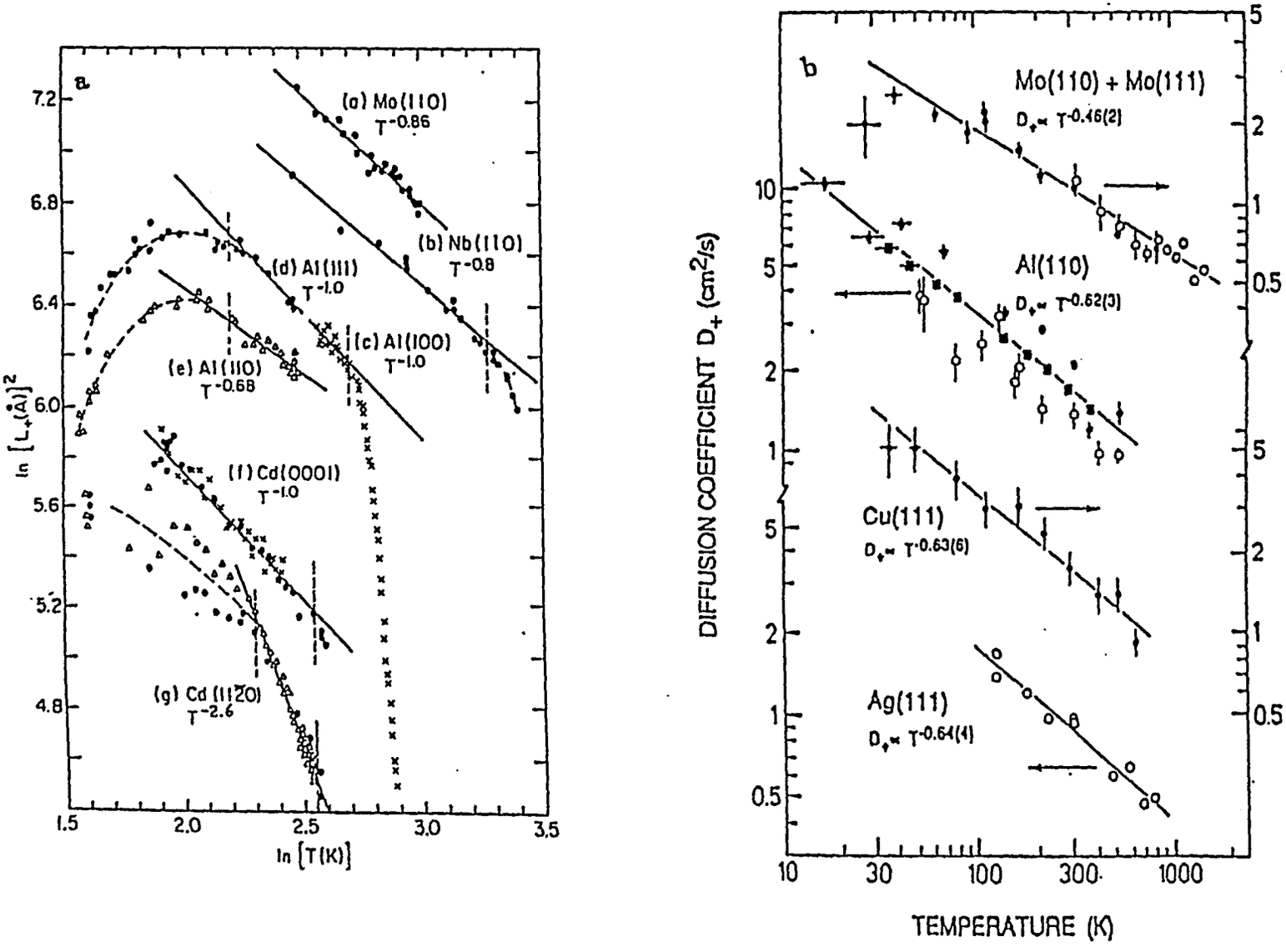

Fig.1.5 Measurement of thermal positron diffusion coefficients in metals a) from Schultz et al (1982) and b) from Soininen et al (1990).

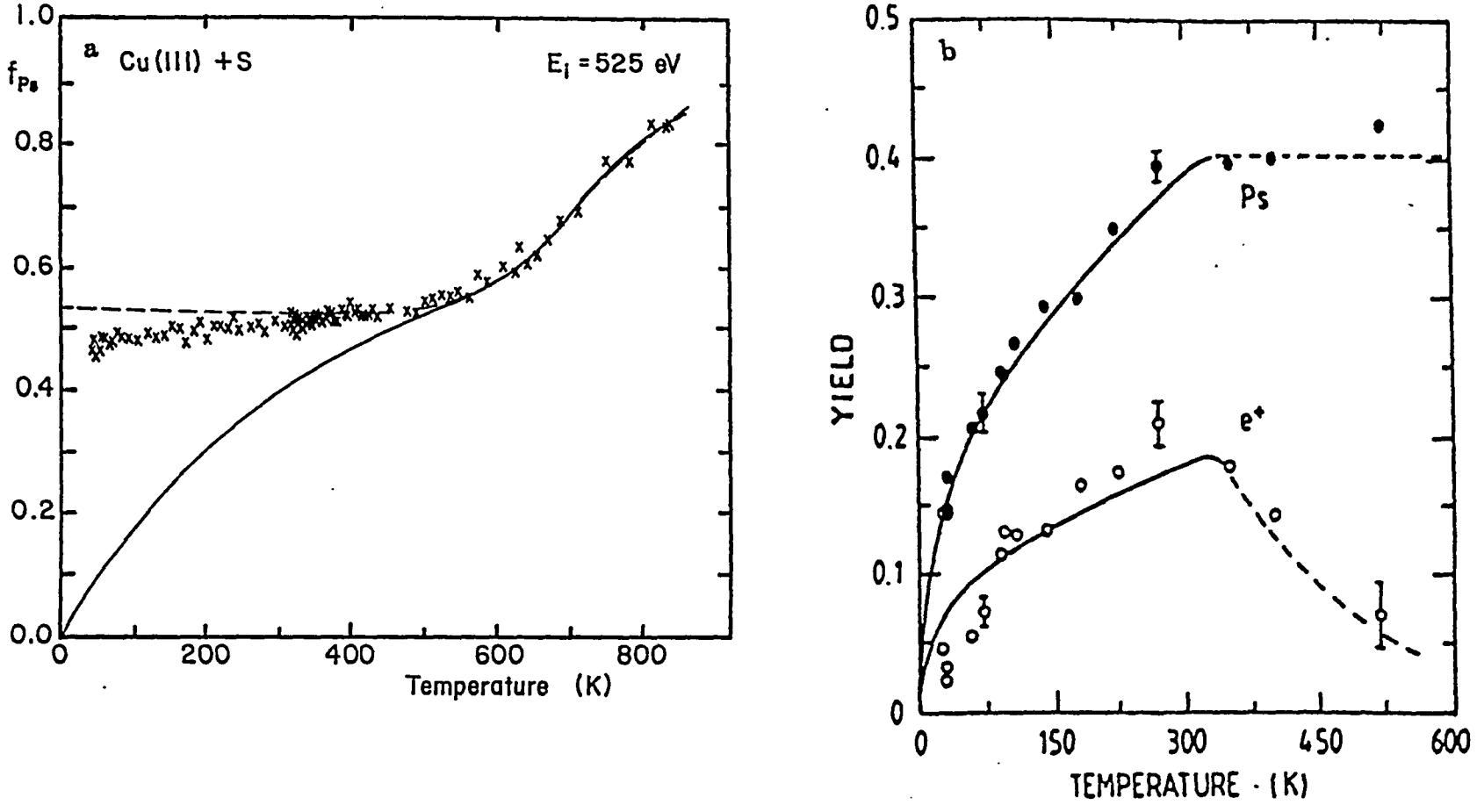

Fig.1.6 Measurement of positron internal surface reflection from a) Schultz and Lynn (1985) and b) Britton et al (1989).

However, there is a lack of quantitative assessments of the epithermal positron effects in solids and the justifications of the way that they are treated by Huomo et al (1987). There are also questions such as at which implantation energy will positrons be considered as essentially thermalized inside the solids, and will the " stopping" profile for thermal positrons be distorted because of epithermal positron emission. Experimentalists are also interested in using the epithermal positrons as a probe for surface or near surface phenomena. For example, epithermal positrons may trap into near surface vacancies resonantly as suggested by Nielsen et al (1986). This phenomena may provide a potentially sensitive probe for near surface defects. In another case, the energy spectra of energetic positrons emitted from ionic (Mills and Crane, 1984) and rare gas solids (Gullikson and Mills, 1986) were found to possess characteristic features which have not yet been further probed. Back-scattered positrons can also pick up electrons at the exit surfaces to form Ps (Howell et al, 1986), this may contribute greatly to our understanding of the positron charge-exchange process at different energies. Most recently, energetic positron emissions from thin metal overlayers (Gidley and Frieze, 1988) presented yet another interesting case which desires an understanding of epithermal positron transport behaviors in solids.

There have been some previous efforts in treating the epithermal positrons. Howell et al (1986) scaled the available data for electron total backscattering in order to fit their nonthermal Ps measurement. This yielded approximately a E^{-1} dependence on the incident positron energy for nonthermal Ps fractions. Britton and Rice-Evans (1988) took the surface returned positron fractions as composed of epithermal and thermal positrons. The positron energy dependence of the two fractions are assumed to be given by eq.(1.10) but with different effective diffusion lengths for epithermal and thermal positrons. The obtained expression is then fitted

to experimental data evaluating the quantities of interest. This approach is inappropriate in several aspects. For example, the effective "stopping" profiles for epithermal positrons and thermal positrons were not distinguished nor discussed; the depletion of thermal positron population because of epithermal positron emission was not considered; further, they obtained a mean free path for elastic scattering of 20Å to characterize the escape depth of epithermal positrons, which should rather be related to inelastic thermalization processes as will be seen later.

Considering this situation, a more plausible model will be developed including epithermal positron effects in the present thesis. The developed model can consistently fit into the previous implantation-diffusion approach. The inclusion of nonthermal positron effects shall present a more complete treatment of positron implantation and thermalization in solids, and their subsequent diffusion as thermal positrons. It will thus enable us to interpret the slow positron measurements more properly.

The epithermal positron effects would require that only the high primary positron energy data be evaluated for positron transport studies, as have been done by Huomo et al (1987). Other considerations also require that the low positron incident energy data be neglected. For example, the conditions for the validty of thermal positron diffusion approximation, and recent results on the implantation profile (Baker et al, 1991) all give more confidence to the results obtained at high positron incident energies. This, however, presents problems in measuring positron transport when the effective positron diffusion length L_{eff} is less or comparable to the thermalization length of positrons. Since at higher positron incident energies, the fraction of thermalized positrons that may return to the surfaces will not vary much because the positron implantation depth is much larger than L_{eff} , reliable extraction of positron transport properties then becomes difficult. The many pa-

rameters and assumptions involved in the implantation-diffusion model give rise to further uncertainties about the evaluated physical quantities. Further, although Ps does not form in bulk metals and semiconductors due to the strong electron screening effects, it does form in many insulating solids. In such cases, the above approach for extracting positron transport characteristics will no longer be valid since Ps transport effects will be present in the obtained results (it is noted that ortho-Ps formed in solids may have pick-off annihilations via two γ-rays which will not be detected by the usual peak-to-valley method of detecting o-Ps; see section 2.1 for more detail). These considerations necessitate other experimental approaches for measuring the positron transport characteristics in solids. This thesis will describe some of our efforts in this area.

We have first of all chosen SiO_2 in a metal-oxide-semiconductor (MOS) structure as our subject. The SiO_2 is of interest not only because we are interested in measuring positron transport in an insulating sample, it is also because MOS is of technological importance. The understanding of the insulating thin film SiO_2 and its growth on the semiconductor substrate are crucial to the device quality for the microelectronics industry (Rubloff, 1990). It is imaginable that positron transport behavior will depend on the characteristics of the oxide, such as the defect concentration, thus it may provide a potential probe for monitoring the oxide quality. Further, a knowledge of positron transport in the oxide is also desired in conjunction with other systematic positron studies of MOS structures being carried in Brookhaven National Laboratory (Leung et al, 1991).

There are some previous measurements of positron mobility in SiO_2. One ACAR measurement of the electric field effect (Sueoka and Koide, 1976) on a single crystal quartz resulted only an upper limit for positron mobility of 15 $cm^2/sec \cdot V$, due possibly to low statistics. Recently, there was a positron energy dependent S-

parameter measurement on a MOS structure (Uedono et al, 1988). From fitting to an implantation-diffusion model in a multilayered structure, the authors obtained a room temperature positron diffusion coefficient of 3.1 $\times 10^{-2}$ cm^2/s or a corresponding mobility 1.2 $cm^2/$ s·V. Apart from the difficulties mentioned above, the result of this S-E measurement will be subject to the knowledge of positron implantation profile in a multilayered structure, and also to the fact that the positrons in the oxide layer contribute only a small signal towards the measured S-parameters at most energies. Thus the obtained mobility of 1.2 $cm^2/s \cdot V$ needs to be examined further.

In our experimental studies of positron transport in the oxide, positrons will be implanted predominantly into the metal and oxide overlayers. For positrons in the oxide where electric field is present due to the external bias, the relative fractions of positrons annihilating at the metal/oxide and oxide/semiconductor interfaces will be affected by the electric field because of the drift motion of positrons in the oxide layer. This drift motion can be detected by the Doppler broadening technique since the two interfaces possess different Doppler broadening lineshapes. The present measurement is sensitive to the small positron mobilities, but is insensitive to the exact stopping profile of positrons in the solids because only one positron energy is used in the experiment. Application of the electric field also guarantees that the immobile positron states can be distinguished from the mobile ones. It should be noted that Ps formation, however, can be affected by the electric field. There are two established mechanisms for Ps formation in insulating solids (Dupasquier, 1983). One is the Ore model, where a valence electron is captured directly by a positron that has insufficient energy to create an electron-hole pair or exciton. Ps formation will thus be the predominant process in an energy gap, the Ore gap,

defined as

$$E_g + E_+ - E_B < E < E_g + E_+, \tag{1.11}$$

where E is the positron kinetic energy, E_B is the Ps binding energy in the solids, E_+ is the positron zero-point energy, and E_g is the band-gaps of the solids. Another Ps formation mechanism is the so-called spur model, where thermalized positrons capture electrons excited during their slowing down process and form Ps. In SiO_2, Ore mechanism for Ps formation has been found to be important (e.g., Chen et al, 1988). It has been suggested (Dupasquier, 1983) that positrons may gain energies to overcome the Ore energy gap when driven by an electric field, thus Ps formation cross section can be dependent on the electric field strength. Caution should be exercised when interpreting the electric field effects in measuring positron mobility in SiO_2.

The complication caused by electric field-induced Ps formation can be minimized with another technique that the present thesis research will be making use of, i.e., the positron annihilation γ-ray energy centroid shifts. From eq.(1.2), the energies of positron annihilation γ-rays will be Doppler-shifted upward and downward by an equal amount in the laboratory system. When one photon energy detector is utilized for measuring the Doppler shifts due to electron momentum distribution in solids, the 511 keV photopeak is Doppler broadened because of the isotropic electron momentum distributions. Although it should be noted that the actually measured γ-ray energy spectrum will not have an exact isotropic broadening around 511 keV. Some of the reasons are: 1) photons will scatter in the detector or elsewhere introducing low energy spreads; 2) the many positron-electron annihilation systems may possess different binding energies ϵ_B which will also cause an anisotropy in the 511 keV broadening; 3) if ortho-Ps forms which may decay through 3-γ, the γ-ray en-

ergy distributions will have the characteristical distribution of a 3-body interaction (as shown in fig.1.3).

The Doppler broadening of the positron annihilation photopeak is true for thermalized positrons in random walk in solids. In case there exists positron drift motion under an electric field, a Doppler shift of the Doppler broadened 511 keV γ-ray energy peak will occur by an amount $\Delta E \approx 511$ keV $\times(v/2c)$ for positron drift velocity v (Mills and Pfeiffer, 1977). In determining the positron annihilation γ-ray centroid shifts, the positron transport characteristics and the electric field configurations can be decided. Since the centroid shift measurement will only reflect positrons in drift motion at annihilation times, it will not be sensitive to positrons in the states not affected by the electric field, e.g., trapped positrons, or positrons in bulk metals. This technique is different from some other positron techniques which will nondiscreminantly measure signals from all the states in which positrons annihilate. Quantitative information may thus be obtained about the mobile or nonmobile states because of this distinguishability of positron states.

§1.3 Positron Interaction with Surfaces

In the past decade, many experimental and theoretical efforts have been devoted to the understanding of the positron interaction with surfaces. Metal and semiconductor surfaces are among the most studied where complications such as Ps formation in bulk solids do not occur. After slow positrons are implanted into the solid and thermalize, a fraction will return to the vacuum-solid interface. Upon reaching the surface, positrons have one of the four possible fates (i.e., positron emission, Ps emission, surface trapping, and surface reflection), presenting an interesting picture of a quantum impurity interacting with the solid surface (fig.1.7).

Thermal positrons returning to the surfaces may, first of all, be reflected back

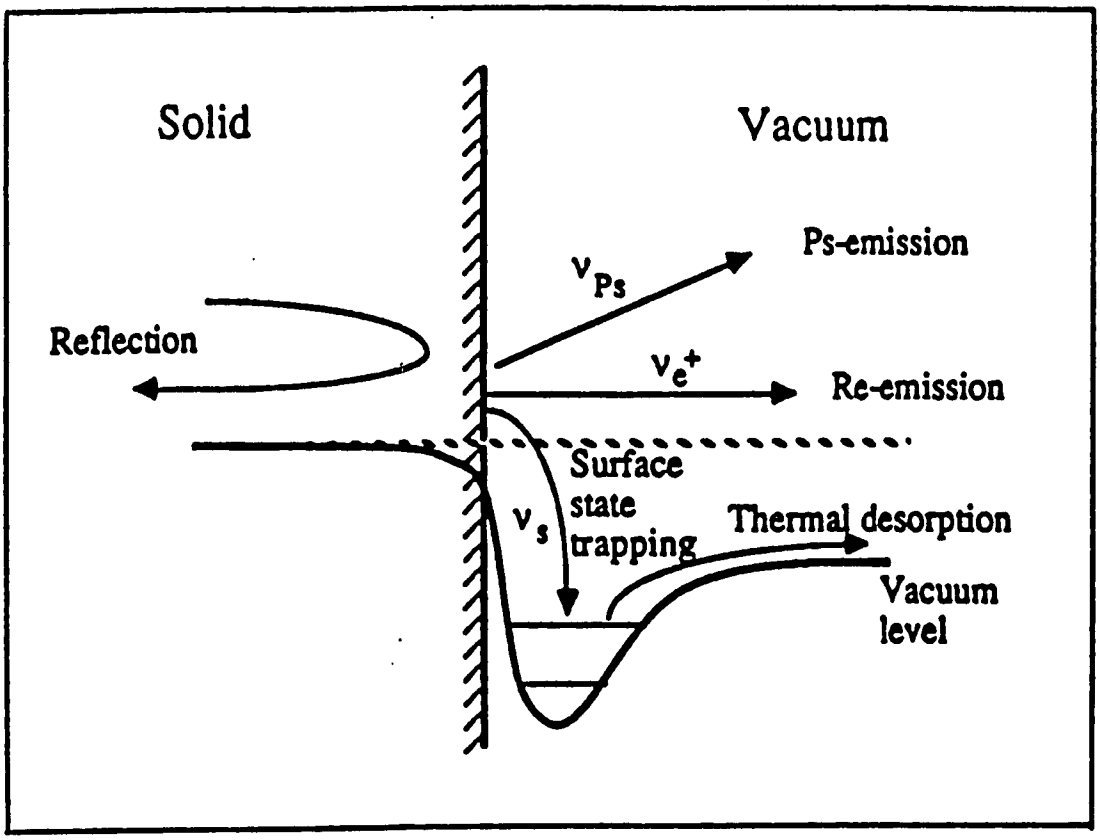

Fig.1.7 Schematics of positron surface processes.

into bulk solids. In the simplest potential well model for positrons represented by plane waves, this quantum reflection is due to the wave-number mismatch of positron wavefunctions inside and outside the solids. The reflection is enhanced for thermalized positrons at low temperatures where unity reflection has been deduced as T$\rightarrow$ 0 K (Britton et al, 1989). Ps sticking on surfaces has also been discussed from thermal Ps desorption measurement on Al(111) surfaces (Mills et al, 1989). Ps failed to exhibit the expected perfect reflection of a very slow particle from a cold surface similar to thermal positrons. The authors suggested that this effect is associated with the breakdown of the perturbation expansion for the Ps reflection probability. It is interesting to compare this sticking behavior difference of Ps and positrons with their difference in producing shake-up events during their emission from solids, though the Ps in the latter case is the workfunction Ps instead of the thermal ones (see below).

The second possibility for positrons is to be reemitted from the solids through the positron channel. Thermalized positron reemission is possible at surfaces with negative positron workfunctions ($\phi_+ < 0$). The positron surface workfunction is determined by the positron chemical potential in the solid and the dipole potential at the surface, the latter is the same in magnitude but opposite in sign to that of electrons. The positron bulk chemical potential depends on positron energy at the bottom of the positron band (the zero point energy) and the positron-electron correlation energy accounting for the attraction between positrons and electrons. Since Ps vacuum binding energy (6.8 eV) is lower than most of the electron workfunctions on metal surfaces, positron reemission will be a non-adiabatic process. It becomes more so when the magnitude of the negative positron workfunction is increased. Theoretically, the Newns-Anderson ion-neutralization model capable of treating non-equilibrium processes has been utilized for deducing the fraction of

positrons reemitted without forming Ps (Nieminen and Oliva, 1980). Gullikson et al (1988) measured the reemitted positron fractions as a function of positron surface workfunctions; their results fitted well with both the ion neutralization model, as well as a density of state model. The energy distribution of the reemitted positrons was also measured (Fischer et al,1986), and it was found that positrons are mostly reemitted elastically in contrast to Ps emission.

It is noteworthy that non-thermalized positron reemission has been found to be important at low primary positron energies, especially for non-metals (Mills and Crane, 1985). Electron pick-up by these fast positrons is also evidenced in Ps measurement (Howell et al, 1986). The energy distribution of reemitted positron from insulators is usually characteristic of the larger band-gaps and the inefficient energy loss processes below the band-gap in these solids (e.g., Gullikson and Mills, 1986). Another interesting case is that of metal bilayers, where energetic positron emission is essentially elastic (Gidley and Frieze, 1988)

The third channel, Ps emission, can be through electron pick-up from the solids by the thermal positrons returning to the surface. Thus formed Ps are energetic and are referred to as workfunction Ps. There may also be thermal Ps emission due to the desorption of surface image-potential trapped positrons. They are referred to as the thermal Ps, and will be discussed later in relation to the positron surface state. The workfunction Ps emission will possess a maximum energy decided by $-\phi_{P_s} = -\phi_+ - \phi_- + 6.8$ eV, where ϕ_+, ϕ_- are the positron and electron workfunctions defined with respect to the crystal zero. $-\phi_{P_s}$ is usually about 2-3 eV which is small when compared with the Fermi energy or plasmon energy for most metals, workfunction Ps emission is thus expected to be strongly adiabatic. However, Ps momentum distribution has been measured with Time-of-Flight (TOF) technique which showed broad distributions (Howell et al, 1987). In the case of Al, there

is less than 0.1% Ps component agreeing with the adiabatic predication (Mills et al, 1990). These findings indicate that shake-up events are important during Ps formation and emission, where the solids are left in an excited state.

Another branch for positrons at the surface is becoming trapped into a surface state. Hodges and Stott (1973) were the first to suggest that the extremely large changes in positron annihilation characteristics in void-containing samples could be accounted for by positron surface state at the void internal surfaces.

The positron surface state is localized in the direction perpendicular to the surface. The surface potential responsible for the surface state is due to the image potential on the vacuum side which saturates when close to the solid. The repulsive potential in the solid side is mostly due to the surface dipole reversed in sign with respect to that of electrons.

Experimentally, the positron surface state is usually evidenced by:

i). The anomalous positron annihilation characteristics such as detected in ACAR or positron lifetime measurements. Lynn et al (1984) carried the first lifetime measurement for positrons trapped in an image-potential of an Al(110) surface. The obtained 580 ps lifetime is far greater than the Al bulk lifetime of 163 ps.

ii). The most direct evidence for positron surface states, however, is the temperature dependent thermal Ps fractions escaped into the vacuum. Thermal Ps emission from some metal or semiconductor surfaces exhibits an Arrhenius desorption behavior. This thermally activated process is attributed to surface trapped positrons picking up electrons from the solids forming Ps. The workfunction value of the electron is usually smaller than the Ps vacuum binding energy, which lowers the energy barrier for the efficient Ps activation process to occur. The TOF technique can be employed for measuring this thermal Ps desorption. Characteristics such as the surface state binding energies can be deduced by studying the desorption

behavior (Schultz and Lynn, 1988).

The Ps desorption rate can be obtained based on detailed balance principle (Chu et al, 1981; Manninen and Nieminen, 1981). For positron surface state with binding energy E_b, the activation energy is deduced as

$$E_a = E_b + \phi_- - 6.8eV, \tag{1.12}$$

which is 0.33 eV for Al(111) surface (Lynn, 1980).

iii). The branching ratios in Ps fraction or the S-parameter measurement. For targets which reemit positrons, the positrons can be repelled or attracted to the surface through a grid system. The changes in Ps formation or S-parameters are associated with the surface state trapping, among other things. The positron trapping branching ratio can thus be approximately deduced (Schut et al, 1988).

iv). The LEPD surface resonance phenomena is another means to study the positron surface potentials (Jennings, 1988). Here, positrons scattering between the image-potential well will introduce fine-structures in the diffraction pattern. It should be noted, however, that such resonance phenomena do not necessarily indicate the existence of a bound positron ground state at the surface, nor the possibility of populating the surface state by positrons even if there does exist a ground level.

Positron trapping into a surface bound state is an inelastic process accompanied mostly by electron-hole excitations in the solids. This is because the energy released during positron trapping is mostly of 1-2 electron volts, phonon emission would have to render a multiphonon process having a much smaller cross section than that of the e-h processes. Because of this energy scale, other more energetic elementary excitations such as plasmons need not to be considered.

There is, however, some evidence that phonon mediated trapping can be im-

portant for certain surfaces with positive workfunctions at low temperatures (Kong et al, 1991). This situation is made possible mostly by the long-range nature of the image potential which introduces Rydberg-like states lying close to the positron energy level in solids so the energy liberated during positron trapping can be absorbed by one-phonon processes. The Rydberg-like states may both serve as positron trapping centers where positrons will annihilate or as precursor states for positrons to trap into more deeply bound states. These shallow surface traps, however, are rendered ineffective at elevated temperatures as detrapping becomes dominant over phonon-assisted trapping. As part of the present thesis, we shall examine the Rydberg states and the possible phonon contributions towards positron trapping. Thus a more complete picture for positron trapping into the image-potential can be obtained.

The above description of positron interaction with surfaces so far has mostly been concerned with metal or semiconductor materials. There has only been a few attempts to assess the situation on an insulator surface. For example, evidence for surface resonance effects in LEPD were observed on NaF, LiF surfaces (Horsky et al, 1989), but it is not clear whether positron surface states exist. In another example, a linear increase of Ps fraction was detected for a quartz sample as the temperature increased (Sferlazzo et al, 1985). The authors interpreted the observation as being due to Ps trapped at a van der Waals potential at the surface. This conclusion , however, is very much debatable considering that Ps can also form in bulk insulators. Thus thermal Ps effects may not only be associated with the possible surface desorption process, they can also be related to bulk Ps transport or trapping behaviors. In fact, Ps formation in bulk quartz was also observed to increase with temperature (Ikari and Fujiwara, 1979), the authors interpreted their findings as positrons thermally activated over the Ore gap forming Ps. Because of

the large band gaps in insulators, questions such as the energy release mechanisms, and the possible surface state desorption channels need also to be answered. The positron wavefunction modulation by the ion potential at ionic solid surfaces is also interesting to examine which may introduce different natures of the positron surface state from the elemental metal or semiconductor surfaces.

Since other techniques such as the Ps fraction measurement will be difficult to indicate the existence of positron surface states for insulators, we will carry a search of positron surface states on KCl(100) surface using the PAES technique. The PAES technique is developed which utilizes the positron annihilation with core electrons of surface atoms (Weiss et al, 1988). The core holes thus created can be filled through Auger deexcitation processes producing Auger electrons (fig.1.8). It has been shown in case of metals and semiconductors, positrons contributing to PAES signal are predominantly associated with those trapped at the surface potential (Mehl et al, 1990; Jensen and Weiss, 1990). The most direct experimental evidence is the temperature dependent measurement of PAES signals (Mayer et al, 1990; Sonninen et al, 1991) where a desorption behavior complementary to Ps fraction is detected indicating the PAES origin from the surface trapped positrons.

The study of positron-surface interaction is not only of interest from the point of view of studying the physics of a quantum impurity many-body interaction with solid surfaces, it is also of practical significance in relation to the many recently developed slow positron probes for surface and thin film analysis (Schultz and Lynn, 1988). Köymen et al (1987) studied metal surface defects created by ion bombardment or metal vapor deposition, where Ps formation is found to be sensitive to the surface defects concentration and annealing conditions. Since Ps forms in most bulk insulating solids, the Ps fraction measurement will no longer provide the necessary surface sensitivity for insulator surface studies. PAES , however, presented with us

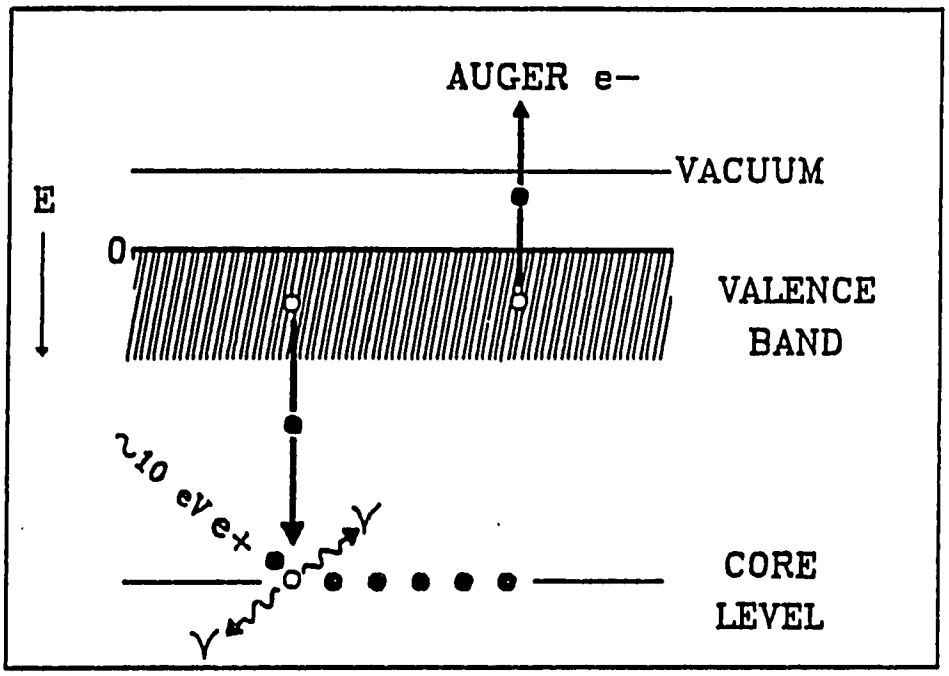

Fig.1.8 Schematics of the principle of positron annihilation induced Auger electron spectroscopy (PAES). The example corresponds to Cu ($M_{2,3}VV$) Auger transition.

another surface sensitive signal with which the insulator surfaces can be studied.

Insulator surfaces have been difficult to examine because of the non-passive nature of the many popular electron, ion, or even photon probes. Electron beams incident on insulators are known to cause electronic sputtering and surface dissociation (Panata and Madey, 1981). Such damage is mostly related to the electron currents and energies that are employed . The characteristic positron beam energy ($0 - 100$ eV) and current (10^{-13} A) utilized in PAES , however, enable the evaluation of fragile samples with minimized charging and radiation damage. The surface sensitivity of PAES will at least be defined by the short escape depth of Auger electrons, and it can also be further improved if positrons producing PAES are trapped in a surface image potential and are predominantly sampling the topmost atomic layers (Mehl et al, 1990). PAES is thus of significance considering the limited surface sensitive techniques for evaluating insulating or fragile systems with minimized damage. In this thesis, we examine experimentally the non-invasiveness of PAES to characterize the KCl surface after non-equilibrium defects are generated by ion sputtering.

Chapter 2
EXPERIMENTAL

With the development of efficient positron energy moderators, variable energy positron beams can be constructed for a variety of solid state experiments. In the present chapter, we shall discuss the positron beam facilities employed for this thesis research (section 2.1), as well as the related data acquisition and analysis techniques (section 2.2).

§2.1 The Slow Positron Beam

Since the author has been involved with the developments and modifications of several positron set-ups in Brookhaven National Laboratory, and the experimental projects of this thesis are carried with two positron beams, the discussions in this section will be concentrating on the general features of a slow positron beam centering around the PAES facility. Some of the details will be discussed in association with the specific experiments in the following chapters.

The general description of the positron beam is given in subsection 2.1.1. The details from the cone-geometry moderation to the electron energy detection system are given in the subsections that follow. In subsection 2.1.6, an apparatus for variable energy positron lifetime measurement is described. The author has been responsible for this setup.

2.1.1 General descriptions

Fig.2.1 shows the PAES beam, the positron source is a $\sim$ 0.4 millicurie Na^{22} with a 4 mm diameter and 5 μm thick Titanium seal. It is thermally coupled to and electrically isolated from the third stage of a closed cycle RMC Cryosystems

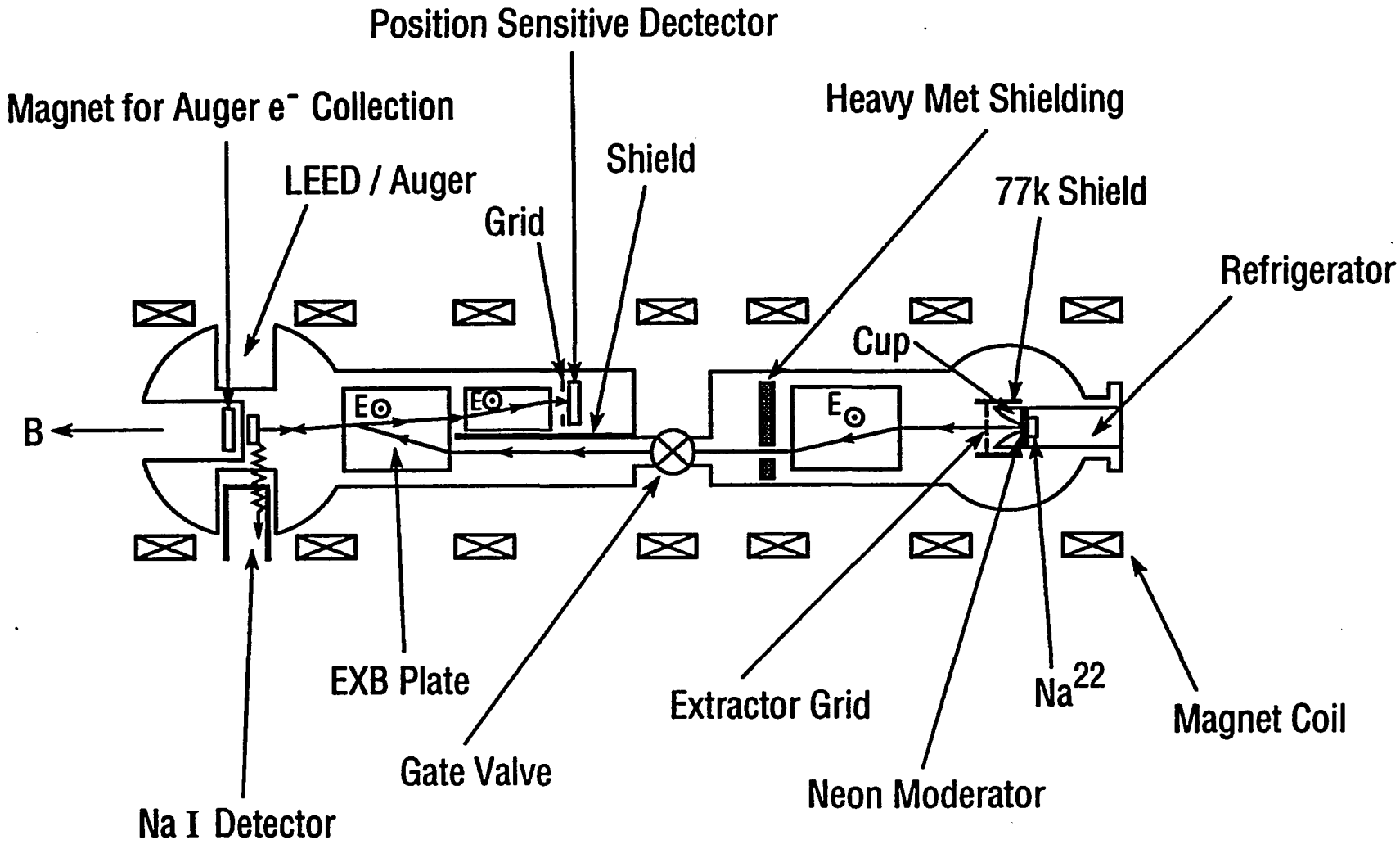

Fig.2.1 Schematics of the PAES beam.

Helium refrigerator. The source is cooled to $\sim$ 5K during the operation. Neon gas is injected through a leak valve and eventually deposited onto an oxygen free high conductivity copper (OFHC) cone-shaped cup.

The slow positrons emitted from the Ne moderator are extracted by the negatively biased extractor grid located before the grounded moderator. They are transported by the magnetic field generated by a group of current coils with an axial field strength of $\sim$ 40 Gauss.

The source chamber contains high energy β^+ particles, and γ ray radiations from the radioisotope which should be shielded from the experimental chamber. A $E \times B$ velocity filter is utilized for this purpose. While fast positrons and photons will be blocked by a heavy metal (Teledyne Power Alloys) shielding (fig.2.1), slow positrons are transversely deflected and feed through an off-center hole in the heavy metal. A tube (not shown) concentric with the hole is located immediately after the heavy metal. It is negatively biased to prevent the electrons in the source chamber from entering the experimental chamber, thus the background when measuring the electron spectra can be reduced.

Positrons leaving the source chamber are guilded by the magnetic field to another $E \times B$ region in the vicinity of the target. They are deflected back to the axial position after passing the $E \times B$ region and subsequently strike the target. The overall beam transport efficiency is $\sim$ 40% (Mayer et al, 1990). The nominal energy with which the positron enters the target is determined by the extractor bias and the sample bias. The role played by a permanent magnet will be discussed in section 2.1.3.

The PAES beam provides capabilities of measuring the 3-γ decay and the Auger electrons simultaneously. The positron annihilation γ-rays are detected by a NaI (TI) scintillator photomultiplier. The Auger electrons are transported from

the target to a one-dimensional position-sensitive detector (1D-PSD) consisting of a channel electron multiplier array (CEMA) with resistive anode encoding (RAE). An energy window for Auger electrons can be set up with a negatively biased grid before the 1D-PSD. For example, to detect Cl (LMM) 181 eV Auger electrons, a low pass energy of 150 eV will separate the Cl signal from the backgrounds of the secondary electrons; and a high pass energy of 210 eV will single out any higher energy components. The difference in the two spectra is taken as the measured Cl (LMM) PAES signal. There is another positively biased grid in front of the negatively biased grid to prevent positrons from reaching the CEMA, it also shields the high voltage biasing on the CEMA and the negative grid from the target region. The secondary or Auger electrons passing these two grids are guilded towards the CEMA detector. A third $E \times B$ region before the CEMA will deflect electrons transversely, the transverse displacements are dependent on the electron energies. This energy dispersion capability of the $E \times B$ field, combined with the RAE function of the CEMA, forms the 1D-PSD for the electron energy analysis carried here (Mayer et al, 1990).

The UHV pumping system after the source chamber is shown in fig.2.2. It is composed of a Balzers TSU050 turbo molecular pump near the gate valve separating the source chamber; an ion pump, a titanium sublimation pump, and a Balzers TSU1500 turbo molecular pump in the experimental chamber. The small diameter of the pipe connecting the source and the experimental chamber enables differential pumping of the two chambers. The ion pump and any ionization gauges can not be operated during the data acquisition. Since the CEMA is sensitive to ionizing electrons and ionized ions. Thus to obtain the UHV environment in the duration of measurements, only the turbo pumps will be operated which will normally maintain the vacuum in the range of 10^{-8} to 10^{-9} torr after about 24 hours of baking.

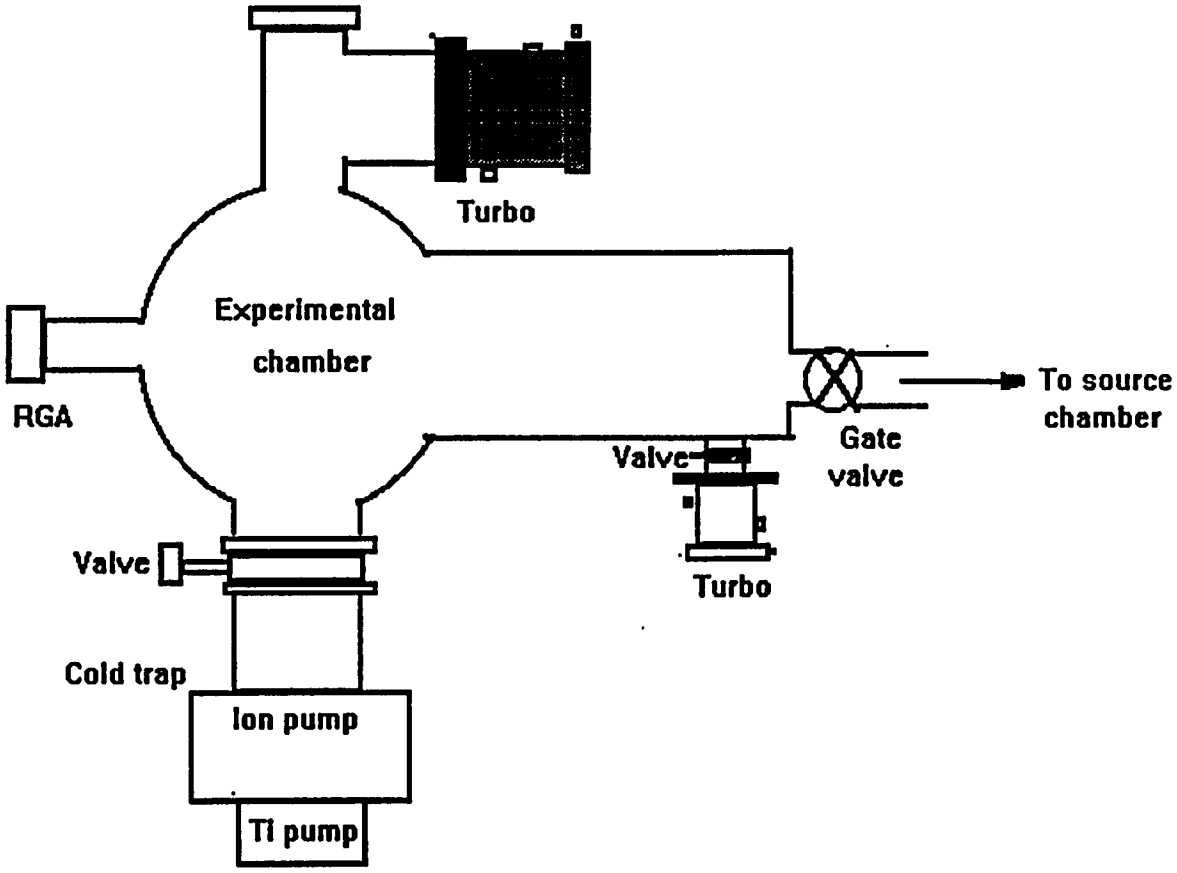

Fig.2.2 Schematics of the UHV system for the PAES experimental chamber.

Residual gas composition in the UHV system can be monitored through a quadruple residual gas analyzer. It should be realized that the present vacuum is not as good as it should be for surface science experiments, care needs to be taken of the possible contamination effects when interpreting the measured results.

2.1.2 The cone-geometry positron energy moderator

For the positron source, Na^{22} is used here because of its relative long half-life. The decay of Na^{22} can be through either electron capture or positron emission. As seen in Fig.2.3a, positron emission when Na is decayed into the excited state of Ne is predominant over other branches. The γ-ray emission due to the nuclear deexcitation of the Ne possesses an energy of 1.28 MeV and acts as a starting signal in conventional positron annihilation lifetime measurements (see, e.g., West, 1973).

Because a neutrino is also emitted during the positron emission or electron capture, the positron energy distribution is continuous as shown in fig.2.3b. To obtain monoenergetic positrons, the PAES beam utilizes one of the currently most efficient solid Ne moderator with an efficiency of $\sim 5 \times 10^{-3}$(Khatri et al, 1990). Rare gas solids such as Ne have large band gaps, thus inelastic processes will be ineffective once the positron energy is below the electron-hole or exciton excitation thresholds. Positrons can thus escape the solids before they annihilate or come into equilibrium with the solids (Mills and Gullikson, 1986).

Moderators using thin foils are usually either in the transmission or the reflection mode (Schultz and Lynn, 1988). Transmission moderator efficiency depends critically on such parameters as the foil thickness and surface conditions which are difficult to control; the efficiency of the reflection geometry is limited by the shadowing of the source in front of the moderator. Lynn et al (1989) proposed a cone-geometry moderator which is used with the PAES beam. It is similar to the reflection type moderator in that moderated positrons are mostly extracted from

the same surface that they are striking, but it avoids the shadowing problem by locating the moderating medium in front of the source. The reemitted positrons are extracted by the appropriate combination of electric (the biasing of the moderator and the extractor grid) and magnetic fields (coils). Thus the efficiency of such a moderator will depend on the accompanying field configuration apart from other factors.

Fig.2.3c shows the geometry of the cone moderator. Constant electric field in the direction parallel to the cone axis will be assumed. The guiding magnetic field will also be assumed to be parallel to the same axis.

The parameter defining the cone geometry is the opening angle β_0 in fig.2.3c. To maximize the solid angle extended by the cone over the source, β_0 should be as small as possible. However, the cyclotron motion of the reemitted positrons in the magnetic field may intersect with the inner cone surface, inhibiting the positrons from being extracted. For this reason, the angle β_0 would preferably be 90^o if positrons are reemitted perpendicular to the surface. The solid angle of the cone over the source for $\beta_0 = 90^o$, however, will be approaching zero, thus little β^+ particles will ever be hitting the moderator. The optimum design of a cone geometry moderator should then compromise between 0 and 90^o to provide the maximum efficiency. The following simple calculations present the electric and magnetic field configurations deciding the cone opening angle.

Suppose a positron reemitted from the cone has a velocity v_0, it can be decomposed into two components perpendicular and parallel to the E-field, v_t^0 and v_l^0. The longitudinal positron movement depends on the electric field with its velocity at time t as

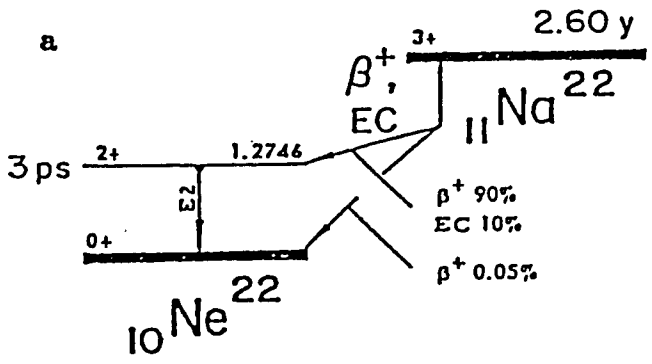

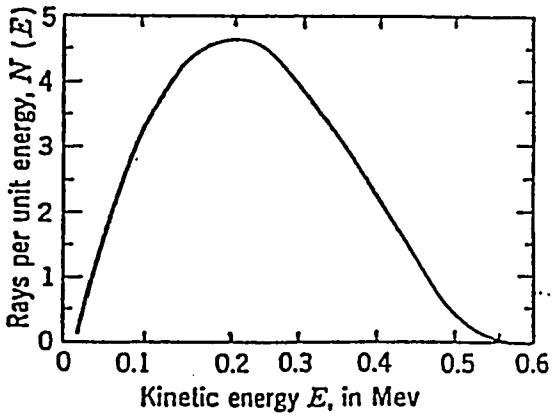

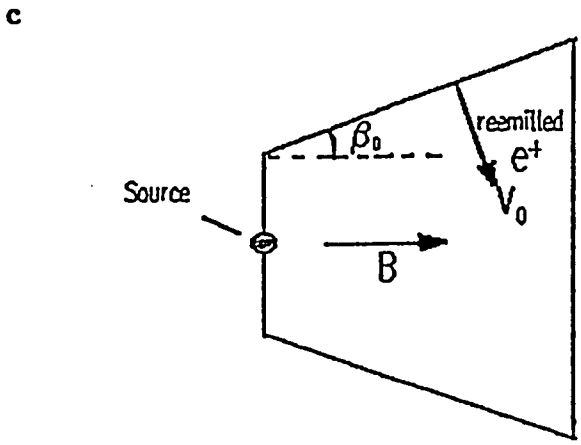

Fig.2.3 a) Na^{22} decay scheme; b) β^+ particle energy distributions from Na^{22} decay; and c) schematics of the cone-geometry moderator.

$$v(t) = v_l^0 + \frac{eE}{m}t, \tag{2.1}$$

and the travelled distance

$$L = v_l^0 t + \frac{eE}{2m}t^2. \tag{2.2}$$

The transverse motion of the positrons depends on the magnetic field. To avoid the reemitted positrons hitting the cone again, the cone angle β_0 should be no less than a critical angle β_c whose *tan* is given by the ratio of the positron cyclotron radius a over a distance L_c travelled during one cyclotron period $1/\omega_B$, i.e.,

$$\beta_0 \geq \arctan[\frac{v_0 \cos\beta_0}{\omega_B}/(\frac{v_0 \sin\beta_0}{\omega_B} + \frac{eE}{2m\omega_B^2})]. \tag{2.3}$$

In case of $E = 0$, β_0 should at least be 45° from eq.(2.3); when E is non-zero and positive, β_0 can be smaller because of the acceleration of positrons in the longitudinal direction. Thus to maximize the solid angle of the CEMA over the target, E-field strength should be increased as much as possible.

The above calculation is concerning extraction of the reemitted positron with an E-field in a constant B-field. It is also possible to minimize β_0 with a spatially varying magnetic field alone. If the magnetic field at L_c is enhanced by a factor ϵ with respect to the point where positrons are reemitted, the terms inside the bracket on the right hand side of eq.(2.3) should multiply $1/\sqrt{\epsilon}$ in the adiabatic limit. For example, in case of zero electric field, the critical angle becomes $arctan(1/\sqrt{\epsilon})$ which is less than 45° for $\epsilon > 1$.

2.1.3 The magnetic transport of positron beams

Once the moderated positrons are generated, they have to be transported to the target region. Magnetic field is a simple way of guilding charged particles. Current carrying coils are employed in the PAES beam. The axial field varies only

a few percent over a distance much larger than the distance travelled by, e.g., a 60 eV positron during one cyclotron period. Thus the adibatic invariant Ba^2 would hold and ensure that the distortion of the beam profile be negligible compared with the original beam size on the order of 1 cm.

The above discussion is for positrons moving along the axis of the guilding magnetic field. In PAES beam, however, off-axis drifts have to be considered. These drifts are sometimes needed, as in case when the moderated positrons are filtered from the radiation backgrounds. The off-axis drifts are sometimes undesired, as they may introduce beam distortions and resolution degradations. Transverse drift of charged particles in a magnetic field will occur, e.g., when the B-field possesses longitudinal or transverse gradient (Jackson, 1955). It is seen from fig.2.1 that the moderated positrons transversely drifted at the first $E \times B$ region will be transported in an off-axis position until they reach the second $E \times B$ region close to the target. Thus the off-axis magnetic field characteristics such as its uniformity, its curvature, etc. have to be considered. They can be the major reasons limiting the present beam transport efficiency.

Fig.2.1 shows also a permanent magnet located behind the sample. It is needed for the total energy analysis of the Auger electrons in a magnetic transport system (Lei, 1988). The 1D-PSD will only be detecting the longitudinal energies of the incoming electrons, while the Auger electron angular distribution is almost isotropic at the target. The permanent magnet will introduce magnetic field gradient which transforms the total energy of the electron mostly into its longitudinal energy once the electron reaches the 1D-PSD. This is the so-called total energy measurement in the PAES beam.

There are other consequences as well due to the gradient of the magnetic field. First of all, the beam spatial spread as indicated by the Lamour radius will be

increased at the 1D-PSD position due to the magnetic field gradient. Assume the magnetic field at the 1D-PSD (B_0) is 40 Gauss, and that at the target position (B_1) is 1000 Gauss. Under the adiabatic approximation , if the outgoing Auger electrons are from a target area with radius about 1 mm, it would correspond to an area of diameter 1 cm at the 1D-PSD. This as compared with the dimension of the 1D-PSD $\sim$ 5cm will introduce serious energy resolution degradations when measuring Auger electrons. Another consequence of the magnetic field gradient is that the energy peaks of the detected electron longitudinal energy distributions will be shifted downward, as discussed by Lei et al (1988).

The permanent magnet will not only affect the outgoing electrons, it will also affect the incoming positrons. Since the positrons are travelling from a weak magnetic field region ($B_0 \sim 40$ Gauss) to a strong field region ($B_1 \sim 1000$ Gauss) , there will be a longitudinal-to-transverse energy conversion as opposed to the process for outgoing electrons. When incident positrons reach the target position, they will have a wider angular distributions with lower longitudinal energies than that determined by the extraction voltage and sample biasing. The positron longitudinal energy at the target position neglecting other effects is

$$E_l = E^0 - \frac{B_1}{B_0} E_t^0, \tag{2.4}$$

where E^0 is the positron total energy which will be a constant in a magnetic field, E_t^0 is the initial transverse part of E^0. This equation is valid when $B_1/B_0 < E^0/E_t^0$, or an initial azimuthal angle for positrons defined by $\theta \leq arcsin\sqrt{B_0/B_1}$ with respect to the beam axis. Positrons outside this angular range will not be able to reach the sample due to the magnetic mirror effects.

2.1.4 Signal detection in positron experiments

In PAES beam, the γ-rays are detected by a NaI (TI) photomultiplier as men-

tioned earlier. The requirement for such γ-ray detection is usually its energy resolution and in our case, its susceptibility towards the magnetic field. Since in order to obtain the maximum solid angle for the scintillator over the target, the photomultiplier should be placed as close to the target as possible. It will thus be close to the magnetic field system. The energy resolution and detection efficiency of the photomultiplier are thus degraded. However, since only the peak-to-valley ratio is evaluated for the 3-γ decay of Ps, the energy resolution is not a critical issue here. The decrease in detection efficiency can be partly compensated by increasing the gain of the spectroscopy amplifier.

The NaI detector, however, is not suitable for Doppler broadening lineshape measurements because of its poor energy resolution. Semiconductor Ge detector is used instead which possesses a resolution function with a FWHM $\sim$ 1.3 keV, yet the magnetic field will not affect its performance. The Doppler broadening measurement and the centroid shift measurement of the positron annihilation 511 keV photopeak described in chapter 3 are taken with the Ge detector.

For the secondary or Auger electron detections in PAES, the CEMA is employed because of its high gain, immunity to magnetic field, sensitivity to charged particles and the possibility of position sensitive detection. The background in PAES spectrum is mostly associated with dark counts; secondary particles or radiations induced from the sample, grids and other regions. In the ideal situation, this background should be independent of the pass energy set by the grid before the CEMA. Experimentally, the background is decided by setting the pass energy above the Auger electron energies of interest.

The energy dispersion in the 1D-PSD for detecting Auger electrons is achieved by spatially dispersing electrons of different energies, which are then measured by the CEMA with RAE function. This spatial dispersion is done with a $E \times B$ method

in the present PAES beam (Mayer et al, 1990).

An electrostatic field is applied between the two parallel plates (fig.2.4a) in a direction perpendicular to the magnetic field direction. The crossed E and B fields will cause the gyration centers of the incoming charged particles to drift transversely with a constant velocity

$$\mathbf{v} = \frac{\mathbf{E} \times \mathbf{B}}{B^2}, \tag{2.5}$$

Positrons of different longitudinal energies will take different transit times to pass the $E \times B$ region, which will then experience varying transverse displacements upon exiting the $E \times B$ region. There is, however, a distortion problem with the parallel electrodes in fig.2.4a. Since the typical beam diameter $\sim$ 1cm spans an appreciable part of the electrode separation (2.5 cm), the electrostatic potential across the beam will produce a spread of longitudinal energies even for incoming particles of the same energy. This transverse spread is of 10% as discussed by Hutchins et al (1986). Thus when the $E \times B$ is used for spatial dispersion of the electron energies, the beam distortion can cause energy resolution degradations.

Hutchins et al (1986) have proposed a pair of curved electrodes to replace the parallel plates in fig.2.4a for positron energy filter purposes. Fig.2.4b shows the curved plates. In the cylindrical coordinate system, the B and E fields are

$$\mathbf{B} = B\mathbf{e}_Z, \tag{2.6}$$

$$\mathbf{E} = \frac{2V}{ln(r_2/r_1)}\frac{1}{r}\mathbf{e}_r = \frac{K}{r}\mathbf{e}_r, \tag{2.7}$$

where K is a constant. With the curved electrodes, though positron longitudinal velocities will still be affected by their transverse coordinates because of the potential gradient across the beam, the beam distortion is decreased because the positron

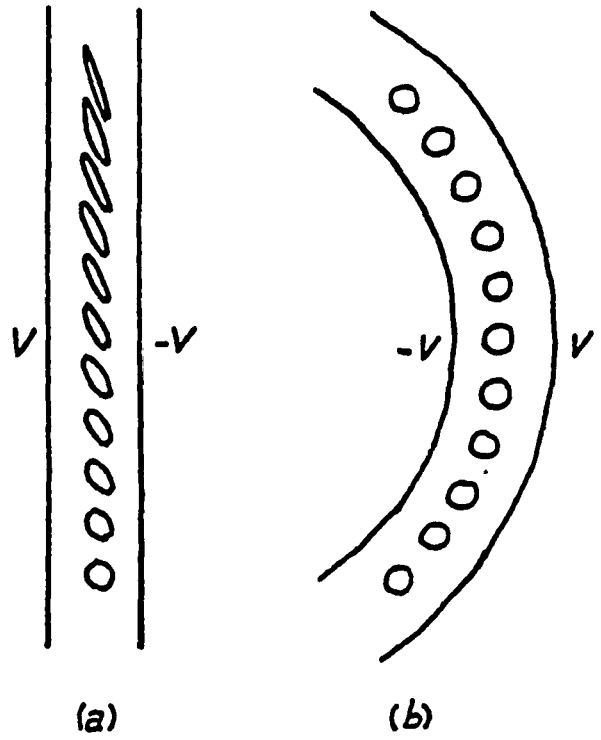

Fig.2.4 a)The parallel plates for producing the $E \times B$ region; and b) the curved plates.

drift velocity will also be dependent on the positron transverse motion as seen in eq.(2.7). For $V > 0$ in fig.2.4b, the drift velocity will be larger if the positron possesses a smaller r, thus compensating the effects of a shorter transit time for the positron to pass the $E \times B$ region. Numerical estimation (Hutchins et al, 1986) shows that the beam spatial distortion is reduced by an order of magnitude with the curved $E \times B$ scheme relative to the parallel plates. Thus if the current planar plates energy dispersion system in the PAES beam are replaced by the curved plates, the energy resolution of the 1D-PSD can also be improved. Although it is noted that the spatial distortion of the Auger electrons due to, e.g., the magnetic field gradient can be more severe (see subsection 2.1.3).

2.1.5 Sample preparation and treatment in PAES

The PAES beam is equipped with an ion gun for surface sputtering cleaning if necessary. Sample cleanness can be monitored with an electron Auger spectroscopy. Heating of the sample is performed by a heater in direct contact with the sample. The basic requirements for the heater are that 1) no emission of thermal electrons within the CEMA detector solid angle from the heater when the experiment is underway; 2) the thickness of the sample heater should be as thin as possible so the distance of the sample surface to the permanent magnet is minimized.

The usual sample surface cleaning procedure is the repeated sputtering annealing over a long time depending on the specific sample and the rate of annealing, etc. The subject of our study with PAES beam, potassium chloride , is an insulator and susceptible to damages by ion or electron beams (Pantano and Madey, 1981). We have cleaved our samples in air before putting them into vacuum. PAES is utilized for examining the surface cleanness. Carbon and oxygen are detected before any treatment is done on the sample. After sputtering with Ar^+ ions of $\sim$ 200-500 eV, the sample is clean with no detectable carbon or oxygen anymore,

only potassium and chloride Auger electrons are seen. After prolonged heating of 10 hours or more at higher temperatures , there will only be Cl 181 eV peak left indicating the annealing of the sputtering damages. The details of ion sputtering damage and annealing study will be discussed in section 4.4.

2.1.6 An apparatus for variable energy positron lifetime measurement

The development of the variable energy positron beam technique has greatly expanded the positron solid state researches. Some of the developed techniques are the direct extensions of the existing bulk techniques developed since the 1950's. For example, 2D-ACAR has been used for measuring positron annihilation at the Al surface image-potential (e.g., Lynn et al, 1985); so is the positron lifetime technique (Lynn et al, 1984); another positron means — the Doppler broadening measurement has had far more popular use in a variety of near surface and interface studies (e.g., Lynn, 1983). However, 2D-ACAR measurement has many stringent requirements such as a large flux of slow positrons that is often not practical for a benchtop beam (e.g., with ^{22}Na as the β particle source). The Doppler broadening technique, though popular and simple to implement, lacks the quantitativeness provided by the ACAR and lifetime techniques. Thus lifetime technique is hoped to provide a compromise which may provide more detailed study of positron states in solids with relatively simple implementations. Previous developed variable energy positron lifetime beams can be divided into two categories: time-tagging with an electrostatic positron beam (Lynn et al, 1984) and the pulsed positron beam (Schödlbauer et al, 1987). Pulsed beam needs advanced beam chopping and bunching capabilities. Electrostatic beam is also more technically challenging than, e.g., a magnetically guilded positron system.

In this work, we'll describe a lifetime setup by time-tagging with a magnetically guided positron beam. Fig.2.5 shows the cross-sectional view of the present lifetime

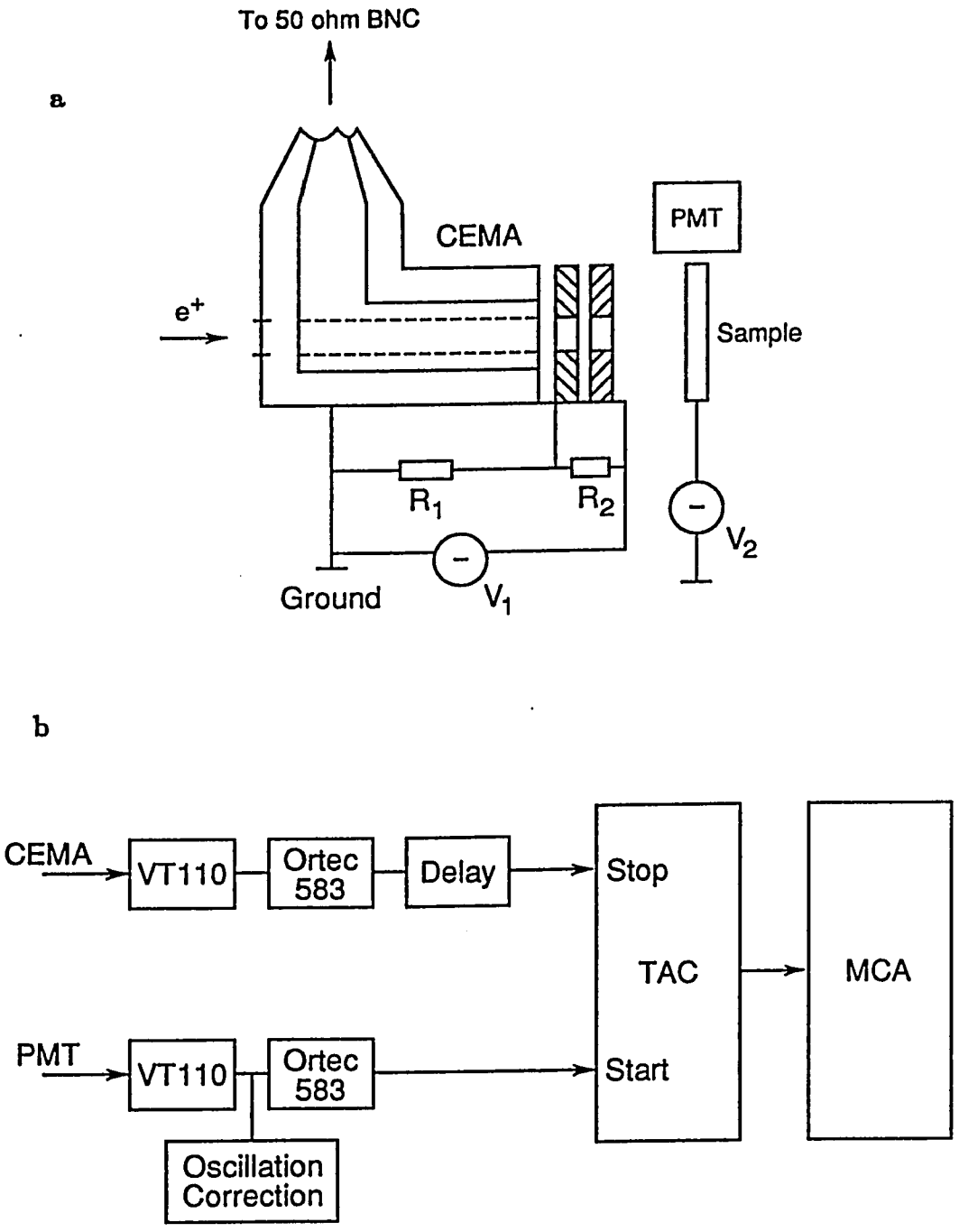

Fig.2.5 a) Schematics of the positron lifetime measurement set-up; b) the electronics for data acquisition.

setup. It consists of a CEMA which is separated about 4 cm from the sample. The CEMA and the sample are both supported and controlled by a UHV manipulator. Once positrons hit the sample, secondary electrons will be generated and detected by the CEMA as a start signal. The subsequent positron annihilation γ-rays in solids are detected by a photomultiplier (PMT) as a stop signal. In practise, however, the CEMA count rate is about two orders of magnitude larger than the PMT count rate, thus the CEMA signal is delayed to serve as the stop signal and the PMT provides the start signal. An inverted time spectrum will thus be obtained.

The CEMA is used for its high efficiency of detecting electrons and its fast timing response. It is of a chevron type CEMA (Galileo Electroptics, model 3025) with a $\sim$ 6 mm diameter hole in the center and an active area $\sim$ 4.9 cm^2. The chevron geometry not only overcomes the possible ion-feed back problem, it also provides a fast electron transit time and an reduced transit time jitter. Positrons are incident from the left side in fig.2.5 and go through the CEMA hole in order to reach the sample.

The anode of the CEMA is originally an resistive metal plate which may cause oscillations in the timing signal and affect the performance of the lifetime system. For example, when the CEMA signal is feed into a time pick-off module, a start (or stop) signal can be triggered over the many oscillations due to the impedance mismatching. For that reason, the present CEMA anode is modified to 50Ω impedance The geometry of the anode is shown in fig.2.5, which is composed of a concentric cylinder section and a cone section. One end of the cone is matched to a BNC adapter. An in-vacuum 50 Ω cable (Ceramaseal Inc.) connects the CEMA anode to a BNC feedthrough which is connected to the rest of the electronics.

The inner-cone and the outer-cone have opening angles α_1 and α_2. The impedance of the concentric cone is (Beck, 1976) $Z = 60 \ln[\cot(1/2\alpha_1)/\cot(1/2\alpha_2)]$.

For $Z = 50\Omega$, the center-cone has the semiangle $\alpha_1 = 8.6^o$ and the outer-cone has $\alpha_2 = 19.8^o$. In order to bring the positron beam through the center hole of the CEMA, a hole of diameter 8 mm is open in the anode shown in fig.2.5. Since the impedance of the cylindrical section is decided by the ratio of the radius of the inner surface of the outer cylinder and that of the outer surface of the inner cylinder, the hole opening in the anode will have little effects on the impedance matchings. The diameter of the hole is decided by two factors among other things. First of all, the active area of the anode would be large if the diameter is small. On the other hand, positrons have to travel through a tunnel $\sim$ 8 cm length before they emerge from the CEMA. Since the major part of this length is in the anode, a too small opening would limit the transport efficiency of positrons reaching the sample. Considering the beam diameter $\sim$ 5-10 mm (depending on the positron energy and other factors), we have chosen 8 mm which is a compromise between the above discussed factors. Another feature worth noting about the CEMA is that it may not be necessary to shield the negative biasings on the CEMA plates from the positrons as in case of, e.g., an electrostatic beam, since the magnetic field would confine the positrons from hitting the CEMA. The operation of the CEMA observes a signal rise time of 1 ns essentially due to the oscilloscope bandwidth.

The photomultiplier tube is a Hamamatsu R2238 with proximity mesh design and 12-stage dynodes. The proximity mesh design is helpful for the operation of the PMT in a magnetic field, but the transit time jitter of the design is typically 800 ps. The plastic scintillator is machined into a cone shape (Kögel, 1979) and wrapped with teflon tapes to improve the system time resolution. The voltage divider for the PMT is also modified with a 50Ω termination at the anode for the timing purposes. The direct current in the PMT voltage divider is modified to be a little larger than the original specification in order to minimize the gain dropping. We have found

that the γ-ray detection efficiency is essentially zero when the PMT is perpendicular to the magnetic field direction. The use of magnetic field shielding materials such as Mu-metals or soft irons has to be careful in order not to distort the low magnetic field for the beam transport. We preferred not to use any magnetic material with the PMT, thus the PMT is titled as much as possible away from the perpendicular position, and yet it should maintain its solid angle over the sample for the maximum detection efficiency. The rise time of the PMT signal is found to be $\sim$ 5 ns. The gain of the PMT is limited because of the reduced efficiency when a magnetic field is present, the possible oscillations introduced by the magnetic field also requires that the low level discrimination in the time pick-off module be raised which will reduce the PMT count rate.

The electronics for processing the signal is schematically shown in fig.2.5b. Start and stop signals are each amplified by a VT110 EG&G fast preamplifier. The time pick-off is provided by constant fraction discriminators (EG&G Ortec 583), from which the start and stop signals are feed into the Time-to-Amplitude Converter (TAC, EG&G Ortec 467). Finally, the amplitude signal from the TAC is sent to a multichannel analyzer.

In the initial operation, while the CEMA signal is perfect with negligible ringings, afterpulsing is observed from the PMT signal. The reason for it is doubted to be intrinsic to the PMT itself. To avoid possible generation of stop (start) signals from these satellite pulses, a correction circuit in fig.2.6 is used (Candy, 1985). This circuit will invert the phase of the main pulse, reduce its amplitude and delay it so it will be overlapping with the afterpulsing. Thus the negative afterpulses can be cancelled. The circuit may overcorrect the afterpulsing introducing positive pulses, but that will not affect the time pick-off by the discriminator from the negative main pulses.

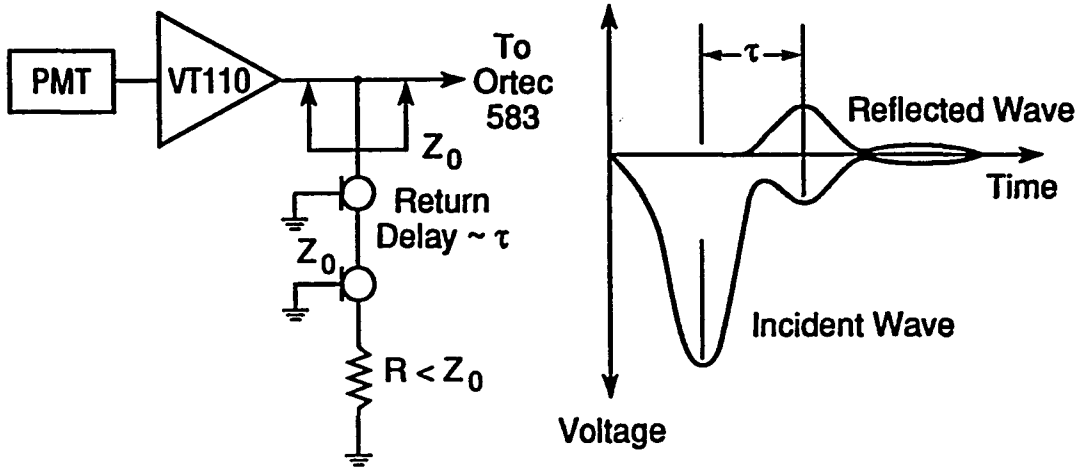

Fig.2.6 The afterpulsing correction circuit for the PMT signal.

To operate the lifetime beam, the first step is to make sure that positrons will be able to transmit through the CEMA hole and reach the sample with high efficiency. This is done by monitoring the counts of the CEMA when the sample biasing is about 1000 V more negative than the front plate of the CEMA. In this case, the CEMA count will be much enhanced due to the higher detection efficiency at the corresponding electron energies. This CEMA count will be sensitive to the CEMA position with respect to the incident positrons. The manipulator controlling the CEMA and other tuning functions may then be adjusted to optimize the operation condition. Presently, we estimate that over 50% positrons can be transmitted to the sample in the optimum case. At much higher positron incident energies, however, the transmission efficiency dropped by almost an order of magnitude. We suspected that the axial direction of the magnetic field, the accelerator, and the setup in fig.2.5 may not be aligned well, thus introducing loss of positrons, e.g., in the tunnel of the CEMA hole.

The measurement in fig.2.7a is done in a magnetic field $\sim$ 30 Gauss with the sample biased 600 V more negative than the CEMA front plate. The effective positron incident energy is 3 keV. Fig.2.7b shows the logarithemetic plot of 2.7a. The system time resolution is estimated to be around 600 ps. It is noted that the time axis is inverted in fig.2.7 because of the inverted start and stop signals.

During the testing, it has been found that the strength of the magnetic field may play an important role in properly operating the apparatus. Fig.2.8 shows the time spectrum when the sample is 1000 V more negative than the CEMA front plate at an effective positron incident energy 3.5 keV. The magnetic field strength is about 90 Gauss. Four peaks are seen in fig.2.8, the physical reasons for these peaks are deduced by adjusting the beam parameters. First of all, the second peak (fig.2.8) is associated with the first encounter of the secondary electrons from the

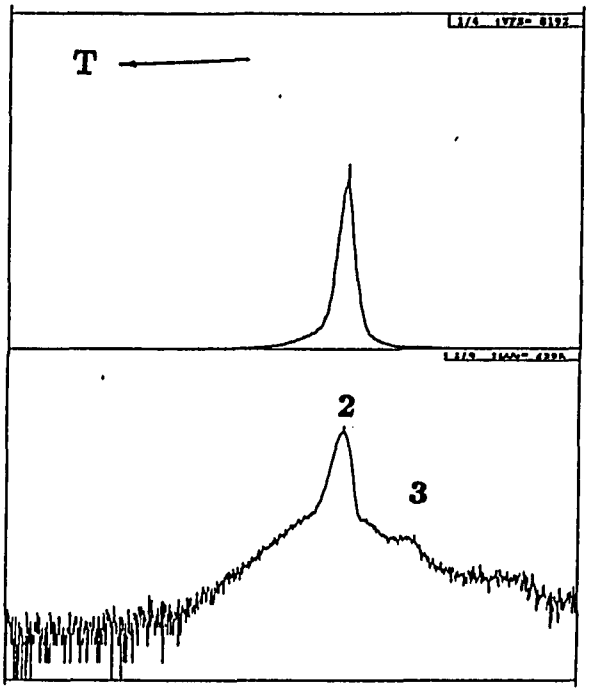

Fig.2.7 The measured lifetime spectrum a) and its logarithmic plot b).

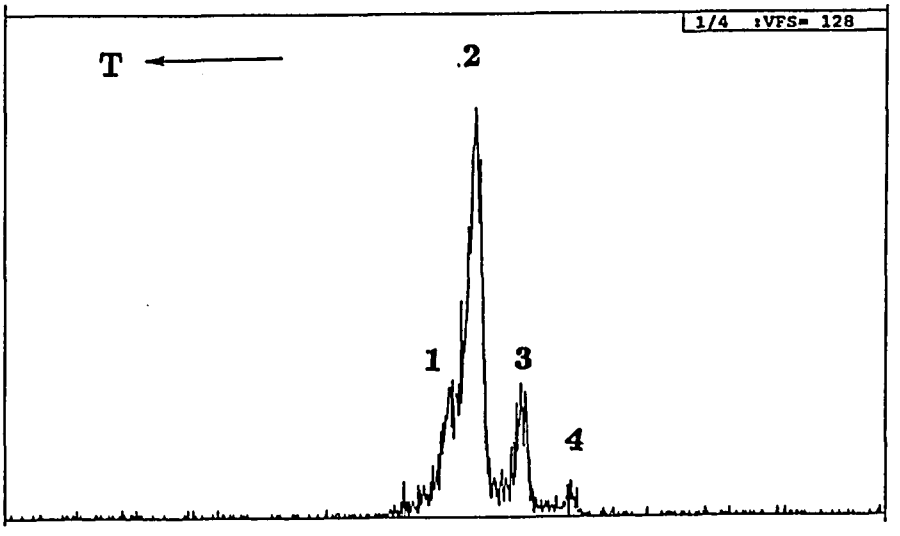

Fig.2.8 Lifetime spectrum taken when the sample is biased 1000 Volts below the CEMA in ~90 Gauss magnetic field..

target with the CEMA. The third and the fourth peaks are possibly related to secondary electrons "reflection" between the sample and the CEMA. In fact, the small peak on the right side of the main peak in fig.2.7 is corresponding to the third peak in fig.2.8. The positions of the above discussed three peaks will shift rightward as the sample biasing becomes less negative with respect to the CEMA front plate. This is explained since the outgoing secondary electrons are less accelerated and thus will register with the CEMA at later times corresponding to shifts towards the right. The intensity of these peaks are also seen to be weakened as the bias difference between the sample and the CEMA decreases. When the sample is biased only slightly negative (10 V or less) than the CEMA front plate, the "reflection" peaks essentially disappeared as seen in fig.2.9. Only the true lifetime spectrum of interest is left apart from the peak on the left side, the true peak is only present when positrons can reach the sample under proper biasings and secondary electrons can be accelerated towards the CEMA. As the sample biasing becomes a little positive compared with the CEMA front plate, only the left side peak will be present. This peak is there even when positrons are repelled from the sample by biasing the sample above the incident positron energy (fig.2.10). When the CEMA position is raised a little so positrons will no longer be able to go into the anode hole, the left side peak will disappear. Further, the position of this peak is not affected by the sample biasing changes as other peaks would in fig.2.8.

The spurious features observed in fig.2.8 will relatively decrease when the magnetic field strength is reduced as is evident in fig.2.7. This fact leads us to believe that the spurious features are related to charged particles confinement by the magnetic field along the axial position, here the charged particles can be either positrons or electrons. We suggest the following explanations for the extra peaks. The first peak is not related to secondary electrons as pointed previously, it is attributed

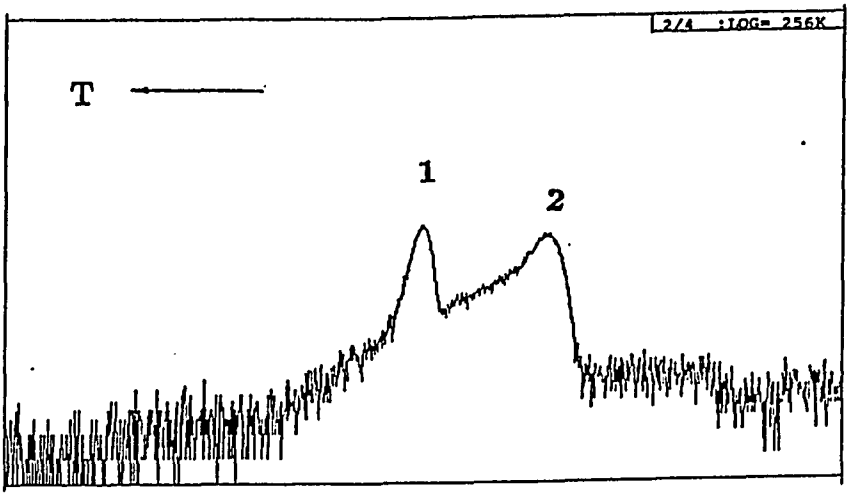

Fig.2.9 Lifetime spectrum taken when the sample is biased 10 Volts below the CEMA.

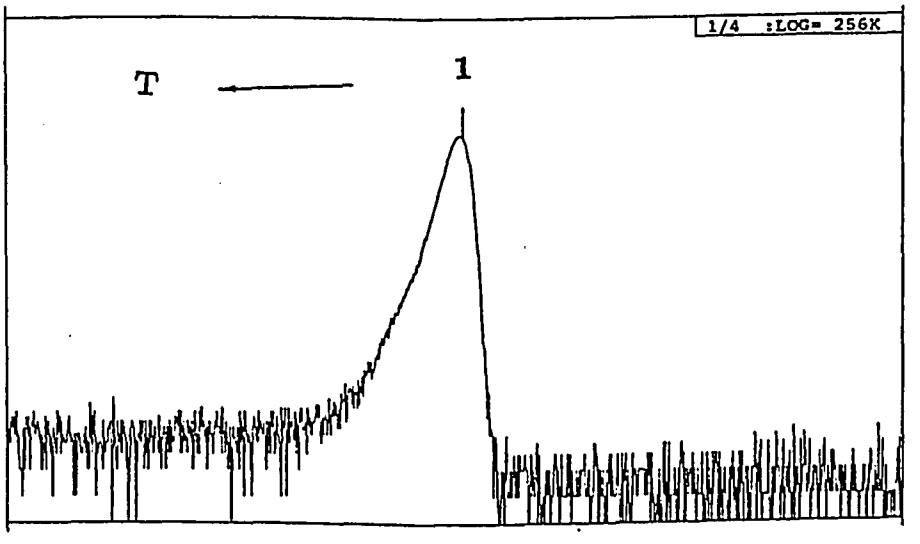

Fig.2.10 Lifetime spectrum taken when the sample is biased at +500 Volts, positron incident energy is 50 eV and the CEMA front plate biasing is −2100 V.

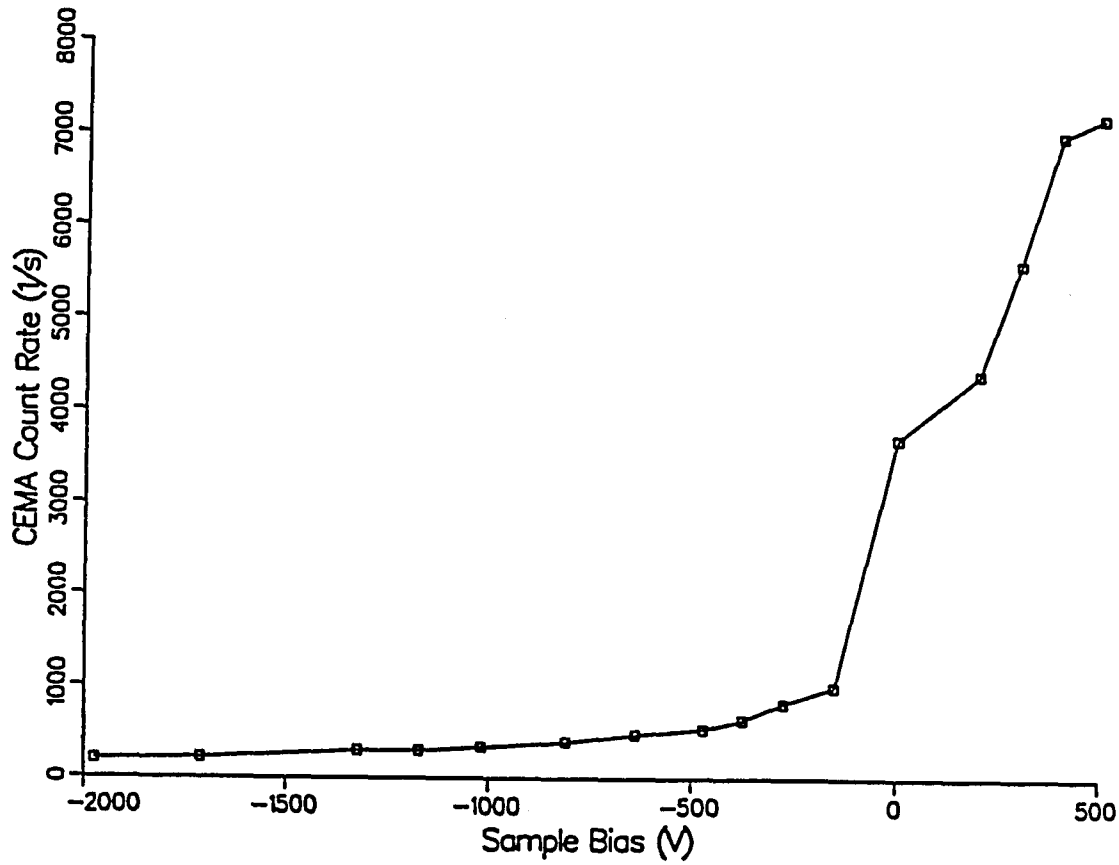

Fig.2.11 The CEMA count rate vs sample biasing at positron incident energy of 50 eV, and CEMA front plate biasing of -2100 V.

to the positrons hitting the CEMA and annihilating there, these positrons can be hitting the channel plate from the back as they emerge from the anode (electrons hitting the back channels, on the other hand, will not be generating signals due to the incomplete charge collection). Positrons can also go through the CEMA center hole and strike the front plate of the CEMA due either to backscattering from the sample or reflection by the electric and magnetic fields. The intensity of this peak increases drastically when the sample is biased above the positron incident energy indicating more positrons will be attracted to the more "negative" CEMA rather than the sample (fig.2.11). The intensity of the first peak (fig.2.8) can be suppressed when the incoming positron beam is collimated to a smaller diameter or when the PMT is better shielded from γ-rays in the CEMA region. Further, when the magnetic field decreases, though the relative intensity of this peak decreases relative to the peak of interest as shown in fig.2.7, its absolute magnitude increases. This dependence on the magnetic field strength suggests that the CEMA signal is enhanced when positron beam size increases . These positrons are registering with the CEMA at an earlier time than the secondary electrons from the sample, thus the corresponding lifetime peak appears on the left-most position in fig.2.8. On the other hand, the third and the fourth peaks are related to secondary electrons reflection between the CEMA and the sample. The "reflection" termed here, again, can be related to electric or magnetic fields induced charged particle trajectory changes, or it can be physical events such as backscattering. When the magnetic field is strong, more secondary electrons will be confined within the axial position missing the CEMA front plate, those hitting the front plate of the CEMA will be 90% detected and have little chance of backscattering. Thus the third and the fourth peaks are possibly related to secondary electrons "reflection" between the CEMA center hole region and the sample. This effect is reduced when the

secondary electrons are less confined by the magnetic field or electric field and have a larger chance of hitting the front plate of the CEMA which will increase the absolute intensity of the real lifetime peak. Since the reflected secondary electrons are detected at a later time by the CEMA, the corresponding lifetime peaks will appear on the right side of the lifetime peak.

We should note here also that the spurious features will not always be decreasing with decreasing magnetic field, since the absolute intensity of the first peak will increase due to the larger cyclotron radius of positrons. A compromise has to be made for the increase in the lifetime peak intensity considering both the collection efficiency of secondary electrons when they are less confined by the magnetic field and the decreasing intensity of the first peak at a higher magnetic field. Perfect alignment of the beam will be critical for eliminating these spurious features. On the other hand, some shielding of the CEMA may possibly eliminate the first extra peak.

In conclusion, we have studied the systematics of time-tagging with a magnetic guilded positron beam for lifetime measurement. Future possible improvements can be carried based on the current findings. For example, the sample can be replaced with a remoderating thin film, and the sample as well as the PMT can be located further down stream. Thus the starting signal will be from secondary electrons related to positrons striking the remoderator, yet the PMT will no longer be able to detect any γ-rays from positron annihilations in the CEMA. In our case, the PMT can also be placed parallel to the magnetic field thus increasing the overall efficiency of detecting γ-rays from the sample. Another note is that we have not paid much attention to improving the timing resolution of the system. Apart from the possible positron trajectory effects (Lynn et al, 1984), the limitations in the system shown in fig.2.6 can be associated with the photomultiplier, the preamplifier

VT110, etc. A channel-plate photomultiplier has been examined which obtained timing resolutions close to the above described PMT. Thus other factors affecting the timing resolution will have to be checked.

2.2 Data acquisition and analysis

There are three subsections in this section. 2.2.1 will discuss the computer interfacing system for the instrument control and data acquisition. Subsection 2.2.2 will present a general introduction to the data analysis encountered in Doppler broadening measurement, centroid shift measurement and the PAES experiment that the present thesis research is concerned. 2.2.3 will introduce our effort in deconvolution of positron annihilation γ-ray energy spectra.

2.2.1 The computer interfacing system

The computer interfacing system is shown in fig.2.12. It is a well-defined small scale project controlling the sample heating, temperature monitoring, and sample biasing, etc. Thus a "board-level" interface architecture which fits into the PC system bus expansion card slots will be the most economical and efficient approach.

The power supply for biasing the sample can be remote-controlled by an analog voltage source. The digital-to-analog (DAC) channel from a DT2811 board (Data Translation, Inc.) provides this capability. Typically, a power supply with output up to 500 Volts is controlled with a voltage source of 0-5 Volts. The resolution of the voltage output is better than 0.5 V. The actual output voltage can be monitored by, e.g., measuring the sample bias with a Keithley Model 197 digital meter, which provides an IEEE-488 interface with the host computer so the actual power supply output can always be compared with the user input and be adjusted if needed.

The next most important control in PAES system is the sample heating and temperature monitoring. The temperature sensor is a K-type (Chromel-Alumel) thermocouple which can provide a wide temperature scan at low cost.

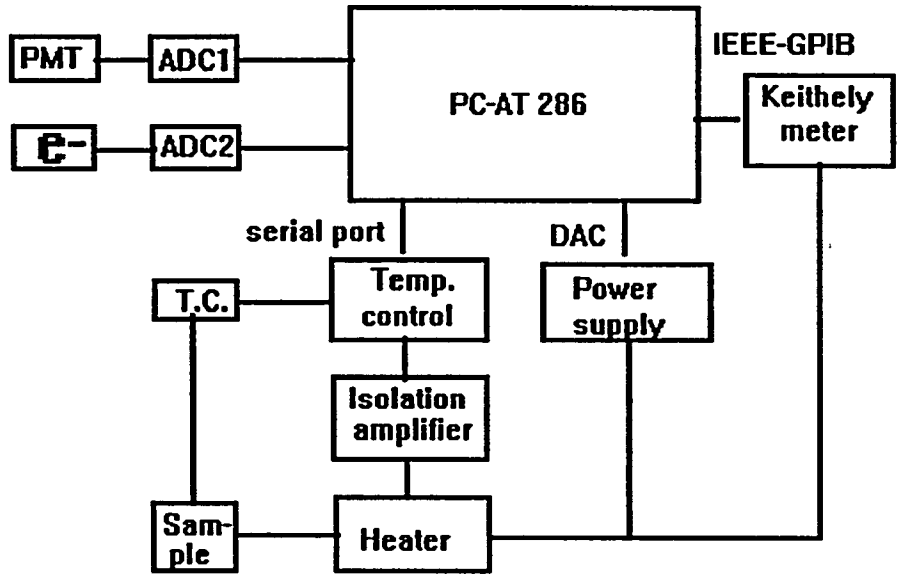

Fig.2.12 Schematics of the computer interfacing system for PAES.

The standard limits of error for the thermocouple is ± 2.2°C ("ASTM Standards on Thermocouples", American Society for Testing and Materials, E230-77, PA, 1977). Other uncertainties in the measured temperatures may arise from aging, humidity, or cold junction compensation circuitry, etc. In the temperature range of interest(< 600°C) here, type-K thermocouple should have very small aging effect because of its oxidation resistance and high melting point.

The temperature controller is an OMEGA 6070A series model. It communicates with the host computer via the RS232C interface. This module allows bi-directional data transfer through a three conductor cable consisting of Signal ground, Receive and Transmit. Thus the temperature can be set to and read from the controller by the PC AT. The control of the power supply for the heater is furnished by the microprocessor in the OMEGA 6070A model, which outputs a 4-20 mA dc current. This current is fed into an resistive load to control an analog voltage driven power supply. The current output uses the proportional algorithm, the actual output level is varied depending on the difference between the set point and the measured sample temperature. This is important for PAES experiment since the CEMA detector can be very sensitive to the on and off status of the heater.

There is a problem associated with the sample biasing when controlling the temperature with OMEGA 6070A. In RS232C standards, the digital one corresponds to a positive voltage between 5 and 15 volts; the digital zero corresponds to a negative voltage between −5 and −15 volts. However, the sample is often biased from −300 V to +30 V, and the power supply for the heater is floated. Thus without isolation of any type, the sample bias will float the power supply for the heater which in turn will float the temperature controller and the RS232C signal level. Proper communication between the computer and the controller can be disrupted. To solve the problem, an isolation amplifier is used to separate the grounds of the

heater power supply and the temperature controller. The RS232C interface works properly after this is done.

The data acquisition is through the two on-board multichannel analyzers of model S-100 by Canberra, Inc. S-100 is a stand-alone microprocessor based subsystem. Signal pulses from the spectroscopy amplifier are sent to the Canberra Model 8075 fast ADC, which is interfaced to an on-board data memory. For the communication between the S-100 and the host control program, data is transferred through I/O mapped addressing. Single word commands from PC-AT cause an interrupt to the MCA microprocessor, while the on-board direct memory access (DMA) controller monitors multi-word commands and data transfer between the PC system bus and the on-board memory.

2.2.2 Data analysis in positron transport and PAES measurements

In positron transport measurement, two techniques are employed, i.e., the Doppler broadening technique and the centroid shift of positron annihilation γ-ray energies.

The Doppler broadening lineshape is characterized as the S-parameter defined on fig.1.2. It is sensitive to the ratio of the core and valence electrons around the positron annihilation sites. Qualitatively, a larger S value indicates a narrower electron momentum distribution. When Ps is present, p-Ps annihilation will effectively increase the S-parameter, though it was noted that the S-parameter may not respond linearly to changes in Ps fraction (Huomo et al, 1989).

From fig.1.2, S is defined as P_1/P with P_1 as the area of the darkened region and P is the crosshatched region. Assume there is no correlation between P_1 and P, the statistical error when evaluating the S-parameter is then

$$\sigma_S^2 = \sigma_{P_1}^2(1/P^2) + \sigma_P^2(P_1^2/P^4) = P_1(P_1+P)/P^3, \qquad (2.10)$$

where σ_{P_1}, σ_P are the errors for P_1, P and are taken as their standard deviations.

Typically, $P \sim 10^6$counts, and $P_1 \sim 5 \times 10^5$ counts, from which σ_S will be less than 10^{-3} as compared with the corresponding S value ~ 0.5. Thus the Doppler broadening parameter can be measured with negligible statistical errors for all practical purposes.

Another technique in positron transport measurement is the centroid shift measurement of the 511 keV annihilation peak. It is estimated (see chapter 3) that this energy shift is around 10 eV for positrons in drift motion in the depletion region of the Si surface. This energy shift is far smaller than the FWHM of the resolution function of the Ge detector ($\sim$ 1.3 keV). Experimentally, the centroid position is obtained by an on-line fitting of the 511 keV peak with a Gaussian plus a background. The first moment of the Gaussian is evaluated as the centroid. The statistical error associated with the determination of the centroid can be estimated as follows. Assume the measured distribution is $[x_i, y_i|_{i=1,2,...M}]$, the centroid will be

$$C \approx \sum x_i y_i / \sum y_i. \tag{2.11}$$

The statistical error for C is then

$$\sigma_C^2 = \sum [(\delta C/\delta y_i)^2 \sigma_{y_i}^2]. \tag{2.12}$$

Considering eq.(2.11), it is obtained

$$\sigma_C = \sigma / \sqrt{\sum y_i}, \tag{2.13}$$

where σ is the variance of the measured distribution $[x_i, y_i|_{i=1,2,....M}]$, and $P = \sum y_i$.

In the measurement to be described in chapter 3, two measurements are actually carried under two opposing electric field directions. This is necessary to

minimize the possible electronic gain drift effects. The difference of the two measurements is taken as the centroid shift that is presented. Since the two measurements are not correlated with each other, the overall statistical error for the centroid shift is $\sim \sqrt{2}\sigma_C$. Take $\sigma = 0.43$(FWHM), the statistical error in deciding the centroid position will thus be less than 1 eV, centroid shifts on the order of 10 eV can be well determined with the present Ge detector.

Another important parameter which can be evaluated from the γ-ray annihilation energy spectrum is the ortho-Ps fraction . Denoting the counts in the total annihilation γ-ray energy spectrum (the hatched region in fig.1.2) as T, a R value can be defined by the ratio of $(T-P)/P$. If the R values are known for the case of zero and 100% Ps formation of the annihilating positrons (R_0 and R_1), and assume the ratio for the corresponding peak counts is P_1/P_0, the Ps fraction corresponding to the R value is then evaluated (Lynn, 1983)

$$F = (1 + \frac{P_1}{P_0}\frac{R_1 - R}{R - R_0})^{-1}. \tag{2.14}$$

Eq.(2.14) needs the calibration parameters R_0, R_1, and P_1/P_0. which will depend among other factors on the geometrical arrangement of the sample and the detector. Because this geometrical arrangement may vary from experiment to experiment in the PAES set up, and further, the exact Ps fraction is not critically required in either the positron transport and the PAES measurements, we have simply taken the R-value defined above to monitor the qualitative changes of the Ps fraction under varying experimental conditions. With the R value, no systematic errors due to the calibration parameters need to be considered, and the statistical error for R is

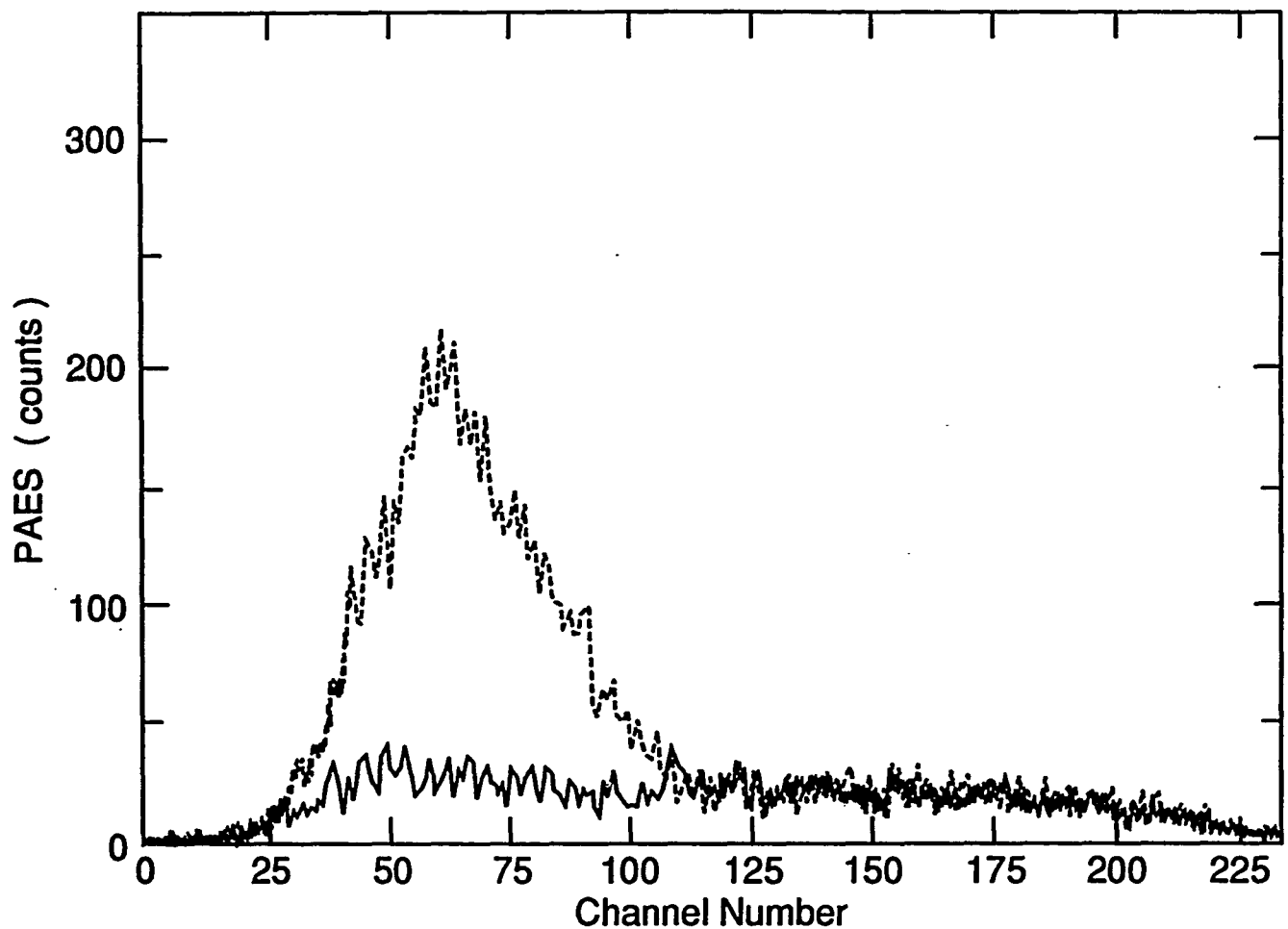

Fig.2.13 Example of PAES spectra for the Cl LMM 181 eV Auger electron measurement. The dashed line is taken with the pass energy 150 eV, and the solid line is the background with pass energy 210 eV.

$$\sigma_R^2 = \sigma_P^2(T^2/P^4) + \sigma_T^2(1/P^2). \tag{2.15}$$

σ_R is also on the order of 10^{-3} for typical measurements.

As for the Auger electron measurement in PAES beam, two energy spectra are usually recorded. One with the negatively biased grid before CEMA set at a pass energy below and the other above the specified Auger electron energy. The latter is needed for evaluating the background of the former spectrum. Fig.2.13 shows an example of the two spectra for PAES measurement of Cl (LMM) 181 eV Auger electrons. The statistical error for the Auger counts is evaluated as $\sqrt{\sigma_1^2 + \sigma_2^2}$, where σ_1 is the standard deviation of the counts of the foreground spectrum above the lower pass energy; and σ_2 is that of the background spectrum above the higher pass energy.

2.2.3 The maximum entropy deconvolution

The Doppler broadening lineshape measurement of positron annihilation γ-ray energy spectra is a popular technique. A simple S-parameter has generally been used to characterize the broadening as mentioned before. However, there exists far more information that can be extracted, e.g., the momenta carried by the annihilating electrons and positrons, Ps formation, defect content and concentrations, or even the geometrical design of the experimental chamber which scatters the γ-rays. Moreover, the quantitative evaluation of the S-parameter depends on the specific experimental setup. The S-parameter can be used in characterizing material properties, but it is difficult to make comparisons between experimental results produced in different setups. This is partly due to the specific window settings when evaluating the S-parameter, and partly due to the finite system resolution. Typical Ge energy detector in Doppler broadening system has a resolution of 1-2 keV (the typ-

ical energy resolution in ACAR experiment is an order of magnitude better, though the statistics is normally not as good due to the low count rate). Deconvolution is essential for comparing data generated in different groups. This will be significant from the practitioner's point of view , as well as for the much needed theoretical studies.

There have been many efforts to extract more interesting quantities from the annihilation spectrum (Schultz and Lynn, 1988), but it has not been very successful due to the poor resolution of the γ-ray energy measurement. For example, MacKenzie (1983) studied positron trapping effects by examining the difference between γ-ray energy spectra of defected and defect-free samples. He found that the resolving ability of the system is important to fully reveal the positron localization effects. To improve the resolution of the Doppler broadening system, deconvolution techniques have been applied to γ-ray energy spectrum (Law and Mogan, 1984; Britton et al, 1988). The Fast Fourier Transform (FFT) is one of the most recently attempted methods, which can provide non-iterative deconvolution efficiently. However, there are problems associated with FFT, as it may exaggerate the noise and introduce spurious features when filtering the power spectrum. FFT may provide a proper estimation of the centroid or even the variance of the distribution, but it is difficult to obtain reliable results for the higher moments. Further more, it is not easy to follow the propagation of errors during the FFT process, thus we may be ignorant of the confidence level for any features present in the deconvoluted distribution. The uncertainty due to the spurious features introduced by FFT will make it difficult to apply this technique in, e.g., carrying the above mentioned defects study through the difference spectrum. More reliable methods are needed if we are interested in the physical representation of the one-dimensional electron momentum density distribution. The practical method should accommodate possible

errors in the incomplete data functions, and provides a deconvoluted spectrum with information permitted by the raw data function only.

In this subsection, the recently developed maximum entropy method will be examined for the deconvolution of positron annihilation γ-ray energy spectra (Kong and Lynn, 1991). The rationale of this technique has been dealt with in depth (Jaynes, 1982). Applications of this method included time series, geography, speech processing, particle dynamics, image reconstruction, etc. The advantage of this formulation is that without complete knowledge of the objective distribution, and if the raw data is noisy and contains possible errors (e.g., due to statistics, etc.), one can obtain a deconvoluted distribution which will be maximally non-committal with regard to the missing information. The solution will have the maximum entropy avoiding spurious features when there are no evidences in the data function. In the following, the formulation of the maximum entropy deconvolution technique will be presented, the results on synthetic data are then discussed.

Before we introduce the deconvolution technique, the Doppler broadening measurements will be briefly discussed. The Doppler broadening system resembles in part to that of the one-dimensional ACAR technique. The latter measures the coincidence rate of 2-γ annihilations, while the former can also measure the 3-γ annihilations of the Ps when a single energy detector is used. For 2-γ annihilation, the energy of the annihilation γ-ray is from eq.(1.2)

$$E = E_0 - \frac{\epsilon_B}{2} \pm \frac{cp_x}{2}, \tag{2.16}$$

The Doppler shift in energy is on the order of $10^{-2}mc^2$, thus the broadening due to the electronic momentum distribution is several keV. The measured 1D-

momentum distribution is associated with the momentum density $\varrho^{2\gamma}(\mathbf{p})$ by

$$N(p_l) = \int\int \varrho^{2\gamma}(\mathbf{p}) d\mathbf{p}_t \tag{2.17}$$

Deconvolution will be able to reveal structures in the electronic momentum density distribution, such as the Fermi surface. Depth profiling of this density distribution is possible by combining the deconvolution technique with the variable energy positron beam techniques. We note here that the 3-γ annihilations may on the one hand complicate the above mentioned simple picture; on the other hand, it can provide information on the Ps fraction.

The measured data function in a Doppler broadening system can be expressed as

$$n_i^{data} = N \int R(x_i, x') p(x') dx' + \epsilon(i), i = 1, 2...M \tag{2.18}$$

where $R(x_i, x')$ is the resolution function of the system. It can be determined at the same time during the Doppler broadening measurement, e.g., by using a reference γ-ray source with energy close to 511 keV. N is the total counts of the M channels of the collected data, $\epsilon(i)$ is the uncertainty in the data function n_i^{data}, $p(x)$ is the normalized original distribution that is of interest. In this work, we follow the usual procedure of concerning ourselves only with half of the data above the centroid ($\approx$511keV) of the distribution. It is then folded back , giving rise to a symmetric distribution around the centroid. We note that even if only 2-γ annihilations exist and the detector is perfectly recording the γ-ray energies, the measured spectrum will not be symmetric due to the ϵ_B term and other reasons discussed in section 1.2. In that respect, two energy detectors may be used to measure in coincidence of the γ-ray energies and deduce the ϵ_B term. The maximum entropy method discussed

here can also be applied to ACAR and the two energy detector Doppler broadening system since only a symmetric distribution is concerned.

Lieu et al(1987) has given a detailed discussion on the maximum entropy analysis of distributions with error-carrying constraints. For discretized original distribution p_i, the proper expression for entropy is termed as

$$S_d = \sum_i -p_i \ln(p_i) - \chi^2, \tag{2.19}$$

χ^2 is defined through

$$\chi^2 = \sum_i \frac{(n_i - n_i^{data})^2}{2\sigma_i^2}, \tag{2.20}$$

where n_i is the convolution of p_i with the system resolution function. Variation of eq.(2.20) with respect to $p(x)$ yields

$$\frac{\delta S_d}{\delta p(x)} = -\ln[p(x)] - \sum_i [n_i^{data} - N \int R(x_i, x')p(x')dx'] \frac{NR(x_i, x)}{\sigma_i^2} + C_1, \tag{2.21}$$

where C_1 is a constant. Define

$$a_i = \frac{-N[n_i^{data} - N \int R(x_i, x')p(x')dx']}{\sigma_i^2}. \tag{2.22}$$

Substituting eq.(2.22) into eq.(2.21), and letting eq.(2.21) equal to zero, we obtain $p(x)$ in terms of parameter a_i's

$$p(x|a) = C_2 \exp[(\sum_i a_i R(x_i, x))], \tag{2.23}$$

where C_2 is a constant. Combining eq.(2.23) with eq.(2.22) yields

$$n_i^{data} - N \int R(x_i, x)p(x|a)dx + \frac{\sigma_i^2 a_i}{N} = 0. \tag{2.24}$$

Finally, we can minimize the functional

$$\Phi = \sum_i [n_i^{data} - N \int R(x_i, x)p(x|a)dx + \frac{\sigma_i^2 a_i}{N}]^2, \tag{2.25}$$

through which we obtain parameters $\{a_i\}, i = 1, 2, ...M$ and the original distribution $p(x)$ in eq.(2.23). We note that minimizing functional eq.(2.25) is equivalent to minimizing eq.(2.19) directly (Zhigunov et al, 1988).

Synthetic data are generated by the superposition of a Gaussian and a parabola to simulate the effects of core electrons and free-electron-like valence electrons respectively. They are then convoluted with a resolution function of Gaussian shape plus added random statistical noises. The total number of counts in the spectrum is $\sim 10^7$. The width of the resolution is chosen to be able to enclose more than three data points to avoid possible "binning" effects.

The principal minimization technique we adopted here is the multi-dimentional variable metric method (Press et al, 1986). The functional eq.(2.25) can be dealt with effectively with this method in most cases, but noting the fact that the number of parameters is the same as our data points for a non-linear function, it can be imagined that the choice of the initial parameters $\{a_i\}$ is very critical. In our approach, we have on the one hand initialized the parameters through minimizing (Zhigunov et al, 1988)

$$\psi = \sum_j \{\ln[p'(x_j)] - \sum_i a_i R(x_i, x_j)\}^2 + \beta \sum_i a_i^2, \qquad (2.26)$$

where $p'(x)$ is the normalized data function, β is a stablizing parameter ~ 10. On the other hand, we have used Goldstein-Price method (James and Roos, 1983) in locating the global minimum when the variable metric method fails to reach the minimum. This ensures that the functional eq.(2.25) is always consistently minimized for different positron incident energies during one experimental run.

In deconvoluting the spectrum, we have evaluated function $p(x)$ from eq.(2.23) over a wider range than the original data. The width of the extended region should be comparable to that of the system resolution function to reduce possible "bound-

ary effects" due to the finite number of data points.

Fig.2.14 and fig.2.15 show two sets of normalized distributions of the deconvoluted results (dashed line) together with the original data (dotted line) and the convoluted data (solid line). Typical error bars are also given there. The original data in fig.2.14 has a parabola component of 30% contributed by valence electrons and the rest is a Gaussian component due to core annihilations. Fig.2.15 has 80% valence electron contribution and 20% core electron contribution. This is evidenced in the less substantial tail region of the distribution in fig.2.15. The transition from the parabola to the Gaussian dominance is most clearly seen from the sudden change in slope around channel 16 and 31. This discontinuity disappears in the convoluted data. In our example, the data function FWHM is $\sim$12 channels, and that of the resolution function is $\sim$4 channels.

It is seen that the agreement between the original data and the deconvoluted data is generally good. The width of the distribution as well as the tail are reproduced with accuracy, but around channel 16 and 31, when the original distributions have discontinuities in slopes, the deconvoluted data is changing more smoothly. There are several reasons for this smooth change. First of all, the underlying principle of the maximum entropy restricts any overdetermination of the spectrum, thus there will always exist residual resolution function. The effect of the residual resolution function is larger when the data is more noisy, in accordance with the spirit of the maximum entropy; the solution will be moved higher up in the "entropy hill" corresponding to a smoother distribution (Jaynes, 1982). Some of the detail in the original data, which we could have interpreted as real if there were no errors, will have to be reinterpreted as probably associated with the noise. The reconstruction of the data will be increasingly smooth when the errors become ever larger due either to exeprimental systematics or statistics. It is more smooth for sharper

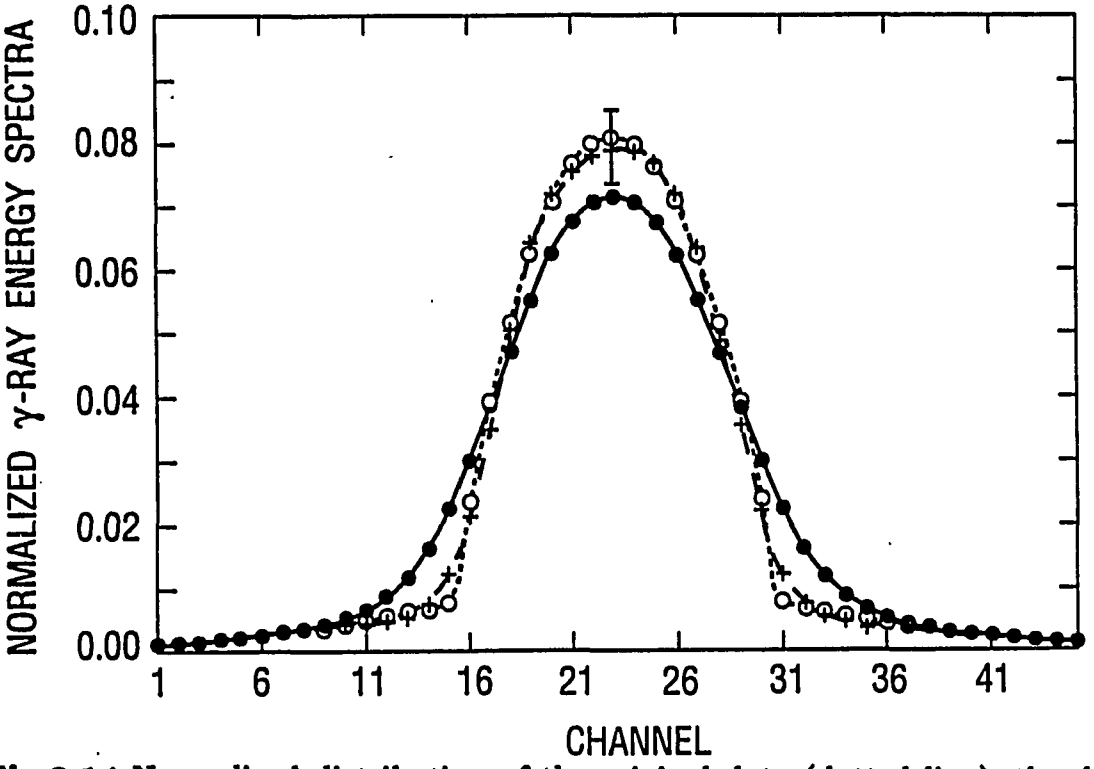

Fig.2.14 Normalized distribution of the original data (dotted line), the deconvoluted data (dashed line), and the convoluted data (solid line). The parabola fraction is ~ 30%.

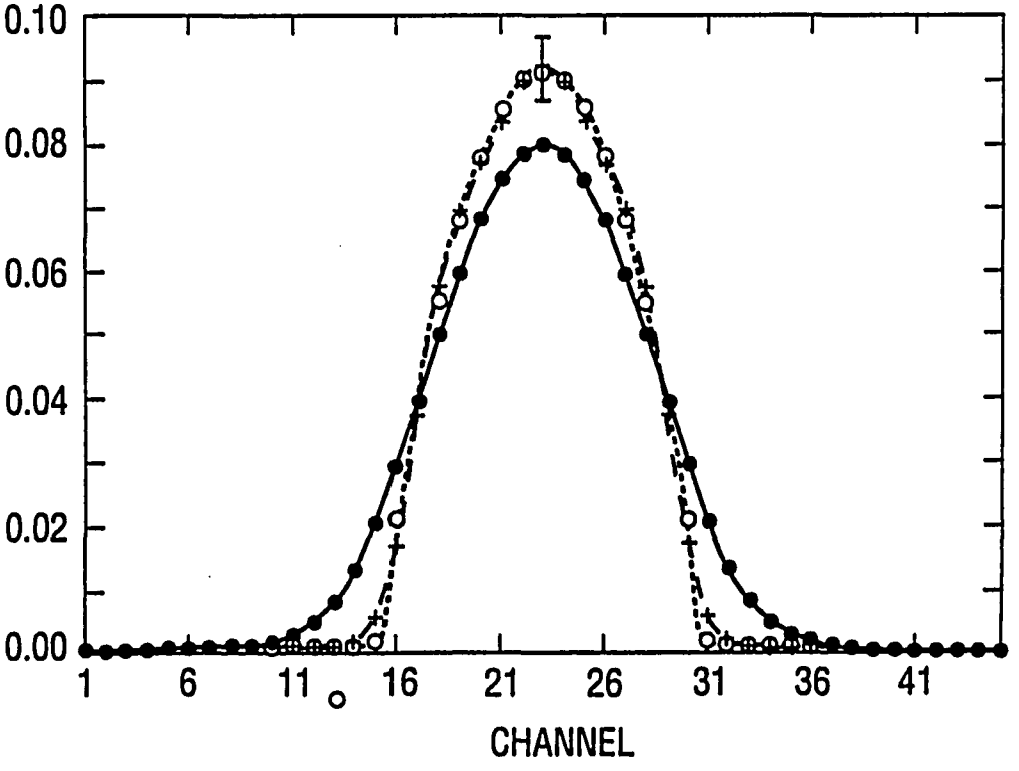

Fig.2.15 Normalized distribution of the original data (dotted line), the deconvoluted data (dashed line), and the convoluted data (solid line). The parabola fraction is ~ 80%.

features present in the original data. This is , as a matter of fact , the advantage of deconvolution with the maximum entropy principle, since we need not to worry about the uncertainty of any features present in the deconvoluted distribution if the errors and the deconvolution are properly treated. However, it is also the disadvantage of the maximum entropy principle in that the technique may be conservative, and will miss some possible interesting physical features. Therefore, there is a trade-off when applying the maximum entropy principle rather than other more deterministic methods. Another reason for the smoothness of the deconvoluted data has to do with the bias in the way we formulated $p(x)$. As seen in eq.(2.23), $p(x)$ is the exponential of a linear combination of a continuous resolution function.

The residual for the two sets of data are shown in fig.2.16, where a) corresponds to the data presented in fig.2.14 and b) that of fig.2.15. The oscillations seen in the residual are not associated with the maximum entropy technique itself as oscillations in FFT do due to the finite band filtering of the data. They merely show the accuracy with which we have deconvoluted the data. We note that the largest amplitudes of the oscillations are always related to discontinuities in slope in the original data. This agrees with the above discussions on the characteristics of the maximum entropy principle. As we reduce the errors of the data, we can approach the more deterministic solution to resolve more detailed structures in the data. The residual will consequently have much smaller amplitudes. Another point to be noted here is that the residual in the side channels are far smaller than those of the central part. This is both due to the slow change in the original data, and to the properties of maximum entropy deconvolution. Since the original distribution in the tail region is relatively featureless compared with the central channels, the maximum entropy method can easily converge on these points. After all, the maximum entropy distribution over an arbitrary interval is constant valued

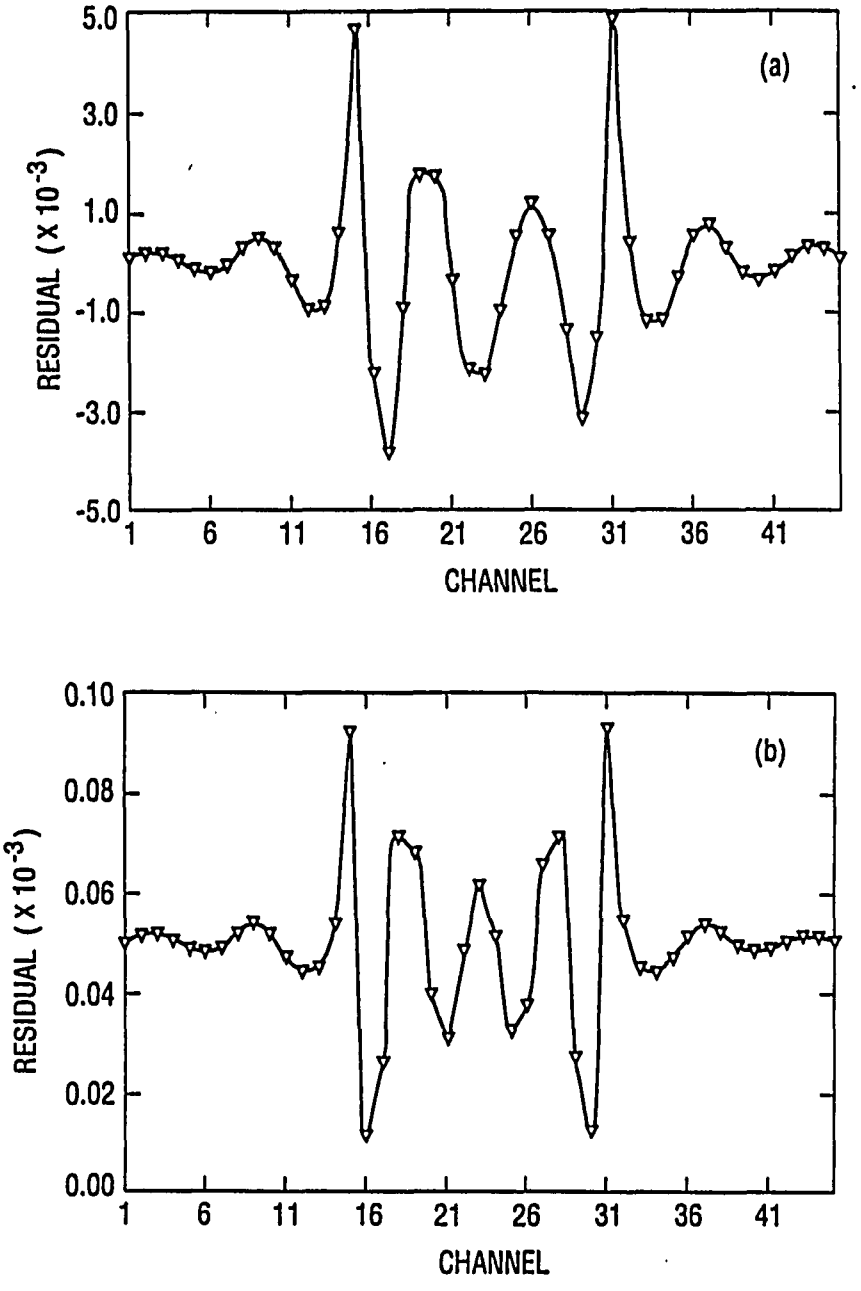

Fig.2.16 The residual for the original data and the deconvoluted a) when the parabola fraction is 30%; and b) when the parabola fraction is 80%.

(Zhigunov et al, 1989).

The difference data between two simulated pair momentum distribution spectra is often employed to examine positron localization effects or other physical processes. We have also taken the difference data of the two sets of spectra as they are convoluted (fig.2.17) and deconvoluted (fig.2.18). The difference of the original data is also shown in fig.2.18. It is seen that in the tail region the original difference data and the deconvoluted difference data agree with each other, but spurious structures are introduced in the central channels. This is not against any forementioned characteristics of maximum entropy principle. When the maximum entropy principle is applied to the positron annihilation γ-ray energy spectrum, it can only guarantee that information not evidenced in the original data will not be introduced into the deconvolution; it can not do the same thing for the difference of two separately deconvoluted data sets. For that purpose, direct deconvolution of the difference data is preferred. One point which should be noted is that the maximum entropy principle applied here implicitly assumes that $p(x) > 0$ in eq.(2.23), it can not be directly applied to the whole spectrum of the difference data where negative numbers are present. We suggest that the negative part in the central channels of fig.2.17 can be inverted and deconvoluted independently. This will also provide information on the side lobes, since they are complementary with respect to the central channels.

In conclusion, deconvolution of positron annihilation γ-ray energy spectra with the maximum entropy method is examined. This technique can also be applied to ACAR, or Doppler broadening measurements with more than one detectors. The introduction of the entropy term serves as a regulating function to accommodate the uncertainty due to errors present in the original truncated data. We may thus avoid introducing non-physical features into the deconvoluted spectrum, yet the resolution of the deconvoluted data is much improved compared to the raw data.

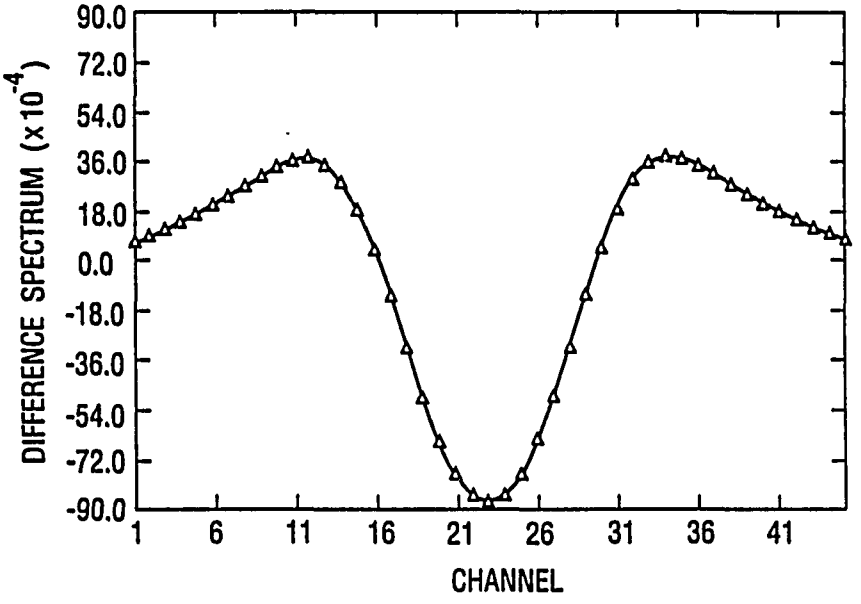

Fig.2.17 The difference data of the convoluted data for parabola fractions of 30 and 80 %.

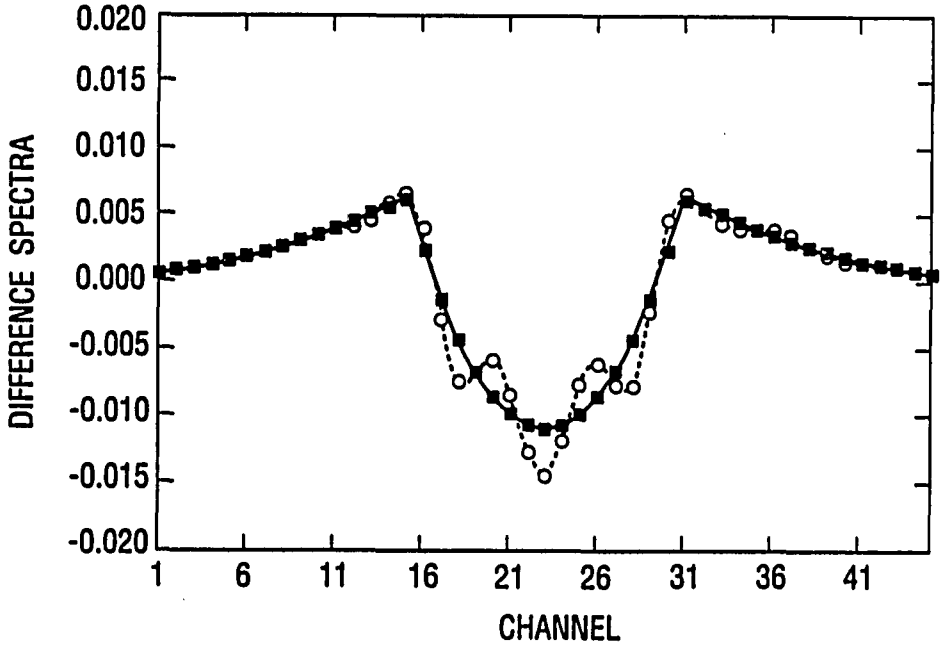

Fig.2.18 The difference data of the original data (solid line) and the deconvoluted data (dotted line) for parabola fractions of 30 and 80 %.

The disadvantage of this method is that the principle of maximum entropy is also a limiting factor for further improvement in the system resolution. The deconvolution process presently requires interactive iterative solution which makes it time-consuming for direct on-line deconvolution of experimental data. The programing part, especially the global minimization problem can also be troublesome in some cases. While other problems are yet to be overcome, we are currently developing an algorithm which combines the maximum entropy method with a more deterministic approach such as FFT for the deconvolution of the positron annihilation γ-ray energy spectra, the resolution of the deconvoluted data may be much improved in that way.

Chapter 3

POSITRON TRANSPORT IN SOLIDS

The understanding of positron transport in solids is crucial for the application of the slow positron techniques in profiling near-surface defects, multilayer structures, etc. This understanding is achieved through both a proper modelling of positron transport behaviors when interpreting experimental results, and through improving the positron techniques for measuring positron transport in a variety of solids. The present chapter describes our efforts in obtaining and improving this understanding on positron transport.

The organization of this chapter is as follows. The transport model of positrons in solids including epithermal positron effects is presented in section 3.1. Section 3.2 and 3.3 will describe two experiments for measuring positron transport characteristics in insulators and semiconductors.

§3.1 Transport Model of Thermal and Epithermal Positrons in Solids

Slow positrons of several thousands electron volts will penetrate the solids to a depth on the order of 10^3 Å. This depth is comparable to thermal positron diffusion lengths in most metals and semiconductors. It is also, however, not exceedingly larger than the length that epithermal positrons have to travel before they come to equilibrium with the solids (i.e., the thermalization length as will be discussed later). Two circumstances need special attention: 1) at low primary positron energies, positrons are implanted within a distance from the surface that can be comparable to the thermalization lengths; 2) in many insulators, epithermal positrons can survive much longer distances because of the inefficient energy loss mechanisms

in these solids. Thus epithermal positron effects have to be considered in slow positron experiments in order to properly interpret the experimental results. Once the epithermal positron transport behavior is understood, the potential can also be tapped of epithermal positrons as a diagnostic tool for studying the condensed matters. The observation of resonant trapping behavior of epithermal positrons at vacancies is one such example (Nielsen et al, 1987). To obtain a more quantitative knowledge of epithermal positrons, we will present our initial efforts in modelling epithermal and thermal positron transport in solids here (Kong and Lynn, 1990). Section 3.1.1 will discuss a two-level, two-stream model, which is extended in section 3.1.2. An application of the present model to a metal bilayer system is then presented in section 3.1.3.

3.1.1 Two-level and two-stream model of positron transport in solids

The current model will be based on the following assumptions.

i). Positrons as they are described by the implantation profile are epithermal. The Monte Carlo simulations of positron stopping in solids have usually been treated to be complete when positron energies are in the range of 30—50 eV (Lynn and McKeown, 1990; Valkealahti, 1988), thus the stopping profiles for epithermal positrons can well be assumed to be the same as obtained from these simulations. For the present modelling, an exponential profile for epithermal positrons will be used. A comparison of the exponential profile will be made with the derivative Gaussian profile in section 3.1.3. The exact profile will not alter any of the conclusions of the present model. It is also noted later that at relatively high positron incident energies, the thermal positrons "stopping" profile will not differ very much from that of the epithermal positrons.

ii). A two-level model is assumed where positrons are either epithermal, or thermal. A many-level model can also be constructed but will only be briefly discussed

in 3.1.2. The two level model will present not only a clear physical picture, it is also mathematically easy to treat. The epithermal positrons in the epithermal level are assumed to possess the same average elastic and inelastic scattering rates. The scattering rates mentioned here will not simply be related to the energy-dependent mean free paths, they are rather related to the positron thermalization length. For example, in a metal bilayer system, positrons reemitted from the substrate into the overlayer can have a well-characterized non-thermal energy due to the workfunction difference in the two metals. It is found that the elastic peak of these non-thermal positrons is attenuated over a length about 100Å (thermalization length), though it is known that the mean free path at the corresponding energy is only of 30-35 Å (Gidley and Frieze, 1988).

iii). Thermal positrons will still obey the one-dimensional diffusion equation (1.9). In consistency with that, a one-dimensional steady-state equation is developed for epithermal positrons. When positrons are "stopped", they will subsequently transport as epithermal positrons governed by the various scattering mechanisms. Those scattered elastically will remain as epithermal during their transport in the solid, while those suffering inelastic scatterings will be assumed to be thermalized and obey the diffusion equation for thermal positrons. The source of the epithermal positrons is the incident positrons as they are described by the implantation profile, and the source for thermal positrons is the inelastically scattered epithermal positrons. Thermalization is thus simply represented by the inelastic scattering rate which can be due to the electronic collision, phonon scatterings, etc.

The one-dimensional epithermal positron transport model developed here is based on the work of low energy electron transport in solids (e.g., Bernasconi et al, 1988). If the positron current at x is $I_e(\theta, x)$ (θ is the scattering angle), and γ_{el}, γ_{in} are the average elastic and inelastic scattering rates per unit length, $S(x)dx$

represents the rate at which the positrons are being implanted between x and $x+dx$, the sum of the bulk annihilation and trapping rate per unit length is γ_a, then the equation for the positron current (Chandrasekhar, 1950) is

$$\cos\theta \frac{dI_e(\theta,x)}{dx} = -(\gamma_{el}+\gamma_{in}+\gamma_a)I_e(\theta,x) + \gamma_{el}\int I_e(\theta',x)\frac{dw}{4\pi} + \frac{S(x)}{4\pi}, \qquad (3.1)$$

where dw is the differential angle element.

The total epithermal current $J_e(x)$ at depth x is

$$J_e(x) = \int I_e(\theta,x)\cos\theta dw, \qquad (3.2)$$

and the total density of epithermal positrons $n_e(x)$ at depth x is

$$n_e(x) = \frac{1}{v}\int I_e(\theta,x)dw, \qquad (3.3)$$

where v is the velocity of the epithermal positrons.

Analytical solution of the integro-differential equation (3.1) is in general unavailable. A two-stream approximation (Bernasconi et al, 1988) will be adopted here in which the particles are assumed moving either in the $+x$ direction or $-x$ direction. Elastic scattering will result in the particle moving in one direction joining the opposite direction stream. This approach can also be generalized to any finite number streams, but here we will treat the two-stream approximation only. Assume the average scattering angle is $\bar{\theta}$, and $\alpha = 1/\cos\bar{\theta}$, then the two-stream approximation gives

$$\frac{1}{\alpha}\frac{dI_+}{dx} = -\frac{\gamma_{el}}{2}(I_+ - I_-) - (\gamma_{in}+\gamma_a)I_+ + \frac{S(x)}{4\pi}, \qquad (3.4)$$

$$\frac{1}{\alpha}\frac{dI_-}{dx} = -\frac{\gamma_{el}}{2}(I_+ - I_-) + (\gamma_{in}+\gamma_a)I_+ + \frac{S(x)}{4\pi}, \qquad (3.5)$$

where I_+, I_- represent the two streams in $\pm x$ directions. The flux and the density in (3.2), (3.3) are then expressed as:

$$J_e(x) = \frac{2\pi}{\alpha}(I_+ - I_-), \tag{3.6}$$

$$n_e(x) = \frac{2\pi}{v}(I_+ + I_-). \tag{3.7}$$

From eqs.(3.4) and (3.5), forward moving positrons are depleted by scattering, annihilation and trapping, and augmented by the elastically scattered backward moving positrons; the opposite is true for the backward stream. Combining equations (3.4) and (3.5) yields

$$\frac{1}{\alpha}\frac{d(I_+ + I_-)}{dx} = -(\gamma_{el} + \gamma_{in} + \gamma_a)(I_+ - I_-). \tag{3.8}$$

$$\frac{1}{\alpha}\frac{d(I_+ - I_-)}{dx} = -(\gamma_{in} + \gamma_a)(I_+ + I_-) + \frac{S(x)}{2\pi}, \tag{3.9}$$

Substituting (3.9) into (3.8) and employing the relation between I_+, I_- and n_e, J_e, a diffusion equation is obtained for the epithermal positrons

$$\frac{v}{\alpha^2(\gamma_{in} + \gamma_{el} + \gamma_a)}\frac{d^2 n_e(x)}{dx^2} = (\gamma_{in} + \gamma_a)v n_e(x) - S(x). \tag{3.10}$$

The corresponding flux density is

$$J_e(x) = -\frac{v}{\alpha^2(\gamma_{in} + \gamma_{el} + \gamma_a)}\frac{dn_e(x)}{dx}, \tag{3.11}$$

with an effective diffusion coefficient

$$D_e = \frac{v}{\alpha^2(\gamma_{in} + \gamma_{el} + \gamma_a)}. \tag{3.12}$$

It is not surprising that eq.(3.10) is in the form of a diffusion equation since the two-stream approximation is essentially an random-walk model in one-dimension. Solution of eq.(3.10) will provide the initial conditions for solving the thermal positron diffusion equation. The stopping profile in eq.(1.9) will be given by $S'(x) = \gamma_{in} v n_e(x)$, i.e., the rate of thermal positrons being fed into x to $x + dx$ due to the inelastically scattered epithermal positrons.

Equation (3.10) indicates that the epithermal positrons will either diffuse back to the surface and escape or are inelastically scattered or are trapped and annihilate with electrons. If $\gamma_{in} >> \gamma_a$, the annihilation and trapping fraction may be neglected and the diffusion behavior of epithermal positrons is then seen to be limited by the inelastic scattering. For positrons at distances far greater than the thermalization length from the surfaces, there will be a negligibly small fraction of epithermal positrons re-emitted. Those positrons will become effectively thermalized while they are diffusing back to the surface.

In the following, eq.(3.10) is solved by assuming a totally absorbing boundary, i.e., $n(x)|_{x=0} = 0$. The $S(x)$ is the implantation profile in a steady-state transport equation which corresponds to a time-averaged rate of feeding the epithermal positrons into the solid. Assume an exponential profile given by

$$S(x) = (1/x_i)\exp(-x/x_i), \tag{3.13}$$

where x_i is the same as that defined in eq.(1.9). For a semi-infinite space with a total absorbing boundary, the Green's function for the diffusion equation similar to eq.(3.10) or (1.9) is

$$G(x, x') = (1/2\beta D)[\exp(-\beta|x - x'|) - \exp(-\beta(x + x'))], \tag{3.14}$$

where $1/\beta$ is the diffusion length, and D is the diffusion coefficient. For epithermal positrons, eq.(3.10) is solved to obtain

$$n_e(x) = \frac{1}{v\gamma_{in}x_0'}[e^{-x/x_0} - e^{\beta_e x}], \tag{3.15}$$

where

$$\beta_e = \alpha\sqrt{(\gamma_{in}+\gamma_a)(\gamma_{in}+\gamma_a+\gamma_{el})},$$

$$x_0' = \frac{x_0^2\beta_e^2 - 1}{\alpha x_0\beta_e\gamma_{in}}\sqrt{(\gamma_{in}+\gamma_a)(\gamma_{in}+\gamma_a+\gamma_{el})}$$

Thus

$$P_t(x) = S'(x) = \gamma_{in}vn_e(x) = \frac{1}{x_0'}(e^{-x/x_0} - e^{-\beta_e x}). \tag{3.16}$$

For thermal positrons with diffusion length $1/\beta_t$, equations (3.14) and (3.16) give the thermal positron density

$$n_t(x) = \frac{1}{D_t x_0'}[\frac{(e^{-x/x_0} - e^{-\beta_t x})}{\beta_t^2 - 1/x_0^2} - \frac{(e^{-\beta_e x} - e^{-\beta_t x})}{\beta_t^2 - \beta_e^2}], \tag{3.17}$$

and the total thermalized positron fraction

$$F_{th} = \int_0^\infty S'(x)dx = \frac{\alpha\gamma_{in}x_0}{1+x_0\beta_e}\sqrt{(\gamma_{in}+\gamma_a)(\gamma_{in}+\gamma_a+\gamma_{el})}. \tag{3.18}$$

The fraction of epithermal positrons that reach the surface is from eq.(3.15)

$$J_e = \frac{D_e}{v\gamma_{in}x_0'}[\beta_e - 1/x_0]. \tag{3.19}$$

and the fraction of thermalized positrons returning to the surface is from eq.(3.17)

$$J_t = \frac{1}{x_0'}[\frac{1}{\beta_t + 1/x_0} - \frac{1}{\beta_t + \beta_e}]. \tag{3.20}$$

With the conventional implantation-diffusion model, however, the fraction of thermal positrons returning to the surface is

$$J_s = \frac{1}{1 + x_0\beta_t}, \tag{3.21}$$

for an exponential implantation profile eq.(3.13) and a totally absorbing boundary in a semi-infinite space.

To make a comparison between eqs.(3.20) and (3.21), we will first discuss the results obtained from our model when inelastic scatterings due to phonons or electrons are dominant, and the epithermal trapping effect is negligible, i.e., $\gamma_{in} >> \gamma_{el} >> \gamma_a$. This approximation yields $\beta_e \approx \alpha\gamma_{in}, x_0' \approx (\alpha^2 x_0^2\gamma_{in}^2 - 1)/\alpha^2 x_0\gamma_{in}^2$.

The fraction of epithermal positrons which experience inelastic scattering and become thermalized is then from (3.18)

$$F_{th} = \frac{\alpha x_0\gamma_{in}}{1 + \alpha x_0\gamma_{in}}. \tag{3.22}$$

This fraction tends to unity when the stopping depth of the positrons is far greater than the thermalization length. In that limit, the use of the thermal positron diffusion equation is justified when using the as-implanted profile $S(x)$ for $P_t(x)$. The fraction of thermal positrons that returns to the surface is

$$J_t = \frac{1}{\beta_t x_0' + x_0'/x_0} - \frac{1}{\beta_t x_0' + \alpha\gamma_{in}x_0'}, \tag{3.23}$$

and that of epithermal positrons is

$$J_e = \frac{1}{1 + \alpha x_0\gamma_{in}}. \tag{3.24}$$

It is seen from eq.(3.24) that the fraction of epithermal positrons returning to the surface is proportional to $E^{-n}(n \sim 1.6)$ with E as the positron incident energy. Howell et al (1986) deduced from their experiment that the non-thermal Ps yield at the surface is proportional to E^{-1}. Apart from the simplicity of the

present model, as well as the insufficient experimental accuracy, other reasons for this quantitative disagreement may be a non-linear branching ratio for the returned epithermal positrons to pick up an electron at the surface and form Ps. It may also be true that the implantation profile at low positron energies is more uncertain (Baker et al, 1991). In fact, there are no results on the shape of the positron stopping profile when the positron incident energy is below 500 eV (Lynn and McKeown, 1990).

The source profile for thermal positrons when only inelastic scattering is considered can also be evaluated

$$S'(x) = \frac{\alpha^2 x_0 \gamma_{in}^2}{\alpha^2 x_0^2 \gamma_{in}^2 - 1}[e^{-x/x_0} - e^{-\alpha\gamma_{in}x}]. \tag{3.25}$$

This profile can be well-approximated by eq.(3.13) when the positrons are deeply implanted and inelastic scattering is predominant, i.e., $\alpha\gamma_{in}x_0 >> 1$.

It is clearly seen by comparing (3.21) with (3.23) that the fraction of returned thermal positrons is changed when the thermalization process is considered. This effect is especially large when the implantation depth x_0 is smaller than or comparable to the average thermalization length. In fig.3.1, we have plotted (3.21), (3.23) and (3.24) for a thermalization length $(1/\gamma_{in}) \sim 100$Å and a diffusion length for thermal positrons ~ 800Å with α taken to be 2 (other figures use the same parameters). Eq.(3.21) gives the reemitted thermal positron fraction (dashed line) from the old model which decreases monotonically with incident positron energy. The solid line is the reemitted thermal positron fraction from our model eq.(3.23). It coincides with (3.21) at high positron incident energies, but is depleted at low incident energies because of the epithermal positron emission. The dotted line represents the reemitted epithermal positron fraction from eq.(3.24). The inset of fig.3.1 is the

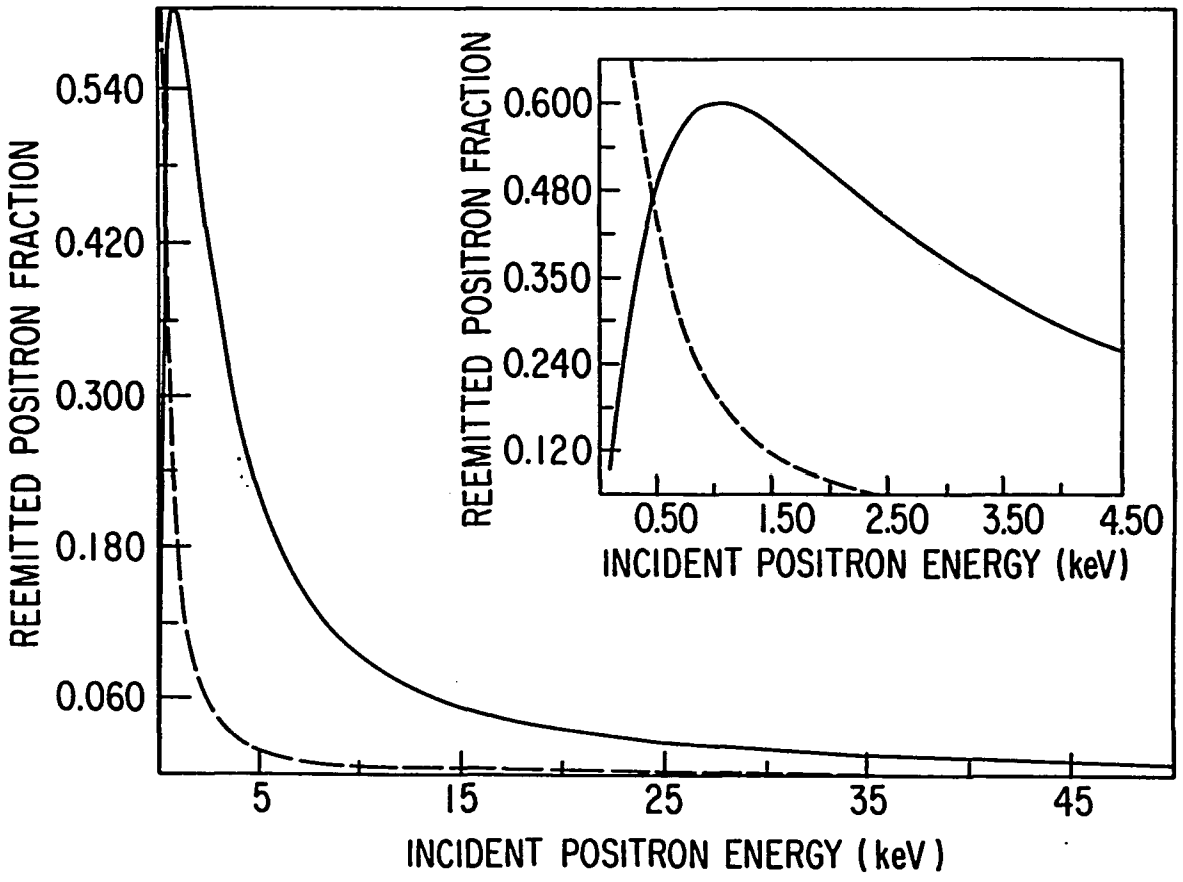

Fig.3.1 The surface returned thermal positron fractions are shown for the implantation-diffusion model (dashed line), and the present model (solid line). The dotted line is the epithermal positron fraction. The inset in the enlarged view of the low energy part.

low energy part; it shows that the deviation of our model from the standard diffusion model starts around 2-3 keV. This is in agreement with the data analysis carried out by Huomo et al (1987), where data obtained with positron incident energies below $\sim$ 4 keV are not treated.

Fig.3.2 shows the ratio of reemitted epithermal positrons to total reemitted positrons. It is seen that the epithermal positron contribution decreases with increasing positron incident energy. This is to be compared with the experimental data for Cu (dotted point). They are in general qualitative agreement. The experimental data was obtained by measuring the energy distribution of the reemitted positrons, and subtracting the thermal portion from it to evaluate the epithermal fraction (Fischer, 1986).

Fig.3.3 shows the total thermalized fraction as obtained from eq.(3.22). It is in general agreement with the above discussion, and more clearly indicates the non-negligibility of epithermal positrons below $\approx$ 3 keV.

Apart from the positron incident energy dependence of epithermal positrons discussed previously, the change of other experimental geometries or material properties may also induce substantial contributions from epithermal positrons. Since the effective thermalization depends on the properties such as the band gaps, the electron gas densities for a metal, etc. The parameters γ_{in}, γ_{el} will thus be material dependent. For example, in ionic and rare-gas solids, the incident positrons will initially lose energy by means of electron-hole creation, exciton excitation and Ps formation, but below the threshold for Ps formation, the only available inelastic channel is phonon scattering. The relatively high initial "stopping" energy caused by the lack of effective energy loss channels enables the epithermal positrons to have a large diffusion length (which can in some cases be larger than the thermal positron diffusion length limited by annihilation), and the reemission of epithermal

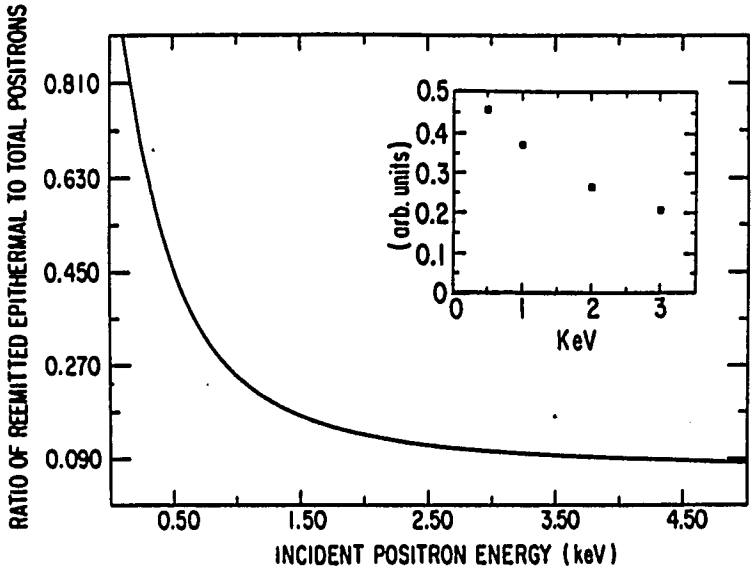

Fig.3.2 The ratio of the epithermal positron current to the total positron current at the surface is shown. Experimental result for Cu(111) surface is also presented.

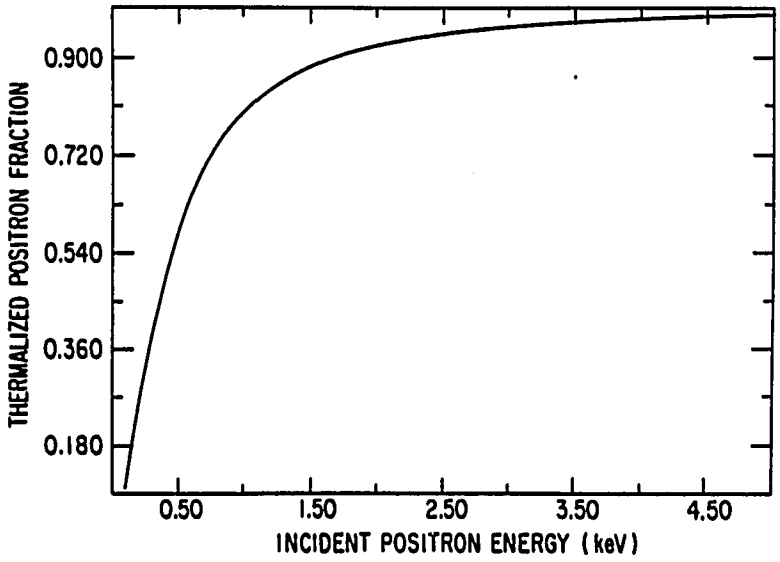

Fig.3.3 Total thermalizaed fraction of the implanted positrons as a function of positron incident energy.

positrons can dominate even at high positron incident energies.

Epithermal positron annihilation in solids are usually not important and are neglected in the above discussions. However, when defects abound in the solids, the epithermal positron trapping rate may become high enough that it will be comparable to or even larger than the inelastic scattering rate. Then the epithermal positron bulk annihilation is no longer negligible. The trapping of epithermal positrons by vacancies has been calculated by McMullen and Stott (1987). It is found that trapping before thermalization can be significant. The epithermal positron contribution to bulk annihilations should then be considered. Otherwise, the epithermal positrons are mostly important because of their possible reemissions from the surfaces in addition to the thermal positrons.

3.1.2 Multi-level and two-stream model of positron transport

Although the above two-level model constituted a useful initial attempt to include epithermal positron effects in a unified picture with the thermal ones, there are nevertheless some aspects which need to be improved. For example, the epithermal positrons are represented by only one average energy level. A more comprehensive treatment should ideally include the following factors:

i) The epithermal positrons actually have an energy distribution. The reemitted epithermal positron energy spread has been measured in different contexts (e.g., Gidley and Frieze, 1988) but it is not fully treatable by the two-level model. Epithermal positrons could provide important information on energy loss especially in the thermalization range if a more detailed theory treating the energy distribution of epithermal positrons were available. Reemitted positron energy spectra have been measured in rare gas solids as well as ionic crystals (Mills and Crane, 1984; Gullikson and Mills, 1986). It is clear now that the inefficiency of positron thermalization in such materials causes an appreciable quantity of epithermal positrons to

be reemitted.

ii). There is in real physical situations a need to treat more than one level of epithermal positrons. For example, in thin metal films studied using reemitted positron spectroscopy (Gidley and Frieze, 1988), when thermal positrons are going from one material to another, they are accelerated or decelerated by the interfacial dipole and are actually heated or cooled relative to the second material. When the overlayer film is thiner than the thermalization length and the positrons are heated when crossing the interface, a large fraction of them can escape into the vacuum as epithermal positrons. This situation is not treatable with a two level picture since additional epithermal positrons are introduced by the interface crossing. Previous efforts to consider electric field effects on positron transport are concerned only with the change in the effective diffusion coefficient due to the field (e.g., Beling et al, 1987), while the change in the thermal positron population is generally neglected. This may not be valid if the E-field is strong and the sample dimension is small.

iii). The actual thermalization process includes transitions between the many energy levels. The physics can be more transparent if the energy dependent quantity is used instead of the averaged mean free path or the thermalization length.

To reduce some of the above mentioned concerns, a formulation of a many level model for epithermal positrons will be presented and a specific three-level model will be discussed in detail.

The epithermal positrons having the highest energies will be assumed to possess a steady-state implantation profile. Intermediate levels between the topmost epithermal level and the thermal positron level will experience elastic and inelastic scatterings. Positron source for the intermediate level will either originate from the inelastic scattered positrons from higher energy levels , or they may come from the energy-gain scattering from lower energy levels. The inelastic and elastic scattering

rates for positrons of energy E will be $\gamma_{in}(E), \gamma_{el}(E)$.

Discrete energy levels are used in the present model. Thus for the k_{th} energy level, positron energy

$$E_k = E_0 - \sum_{i=1}^{k} \Delta E_i, \tag{3.26}$$

where ΔE_i is the allowed energy difference between two neighboring levels. The equations in a two-stream approximation will be given assuming that there is population exchange only between neighboring levels, i.e. only energy loss rate $\gamma_{in}^{k,k+1}(E_k)$ and energy gain rate $\gamma_{in}^{k,k-1}(E_k)$ are non-zero. The relation between the two branching ratios and the total inelastic scattering rate of level k is

$$\gamma_{in}^{k,k-1}(E_k) + \gamma_{in}^{k,k+1}(E_k) = \gamma_{in}(E_k). \tag{3.27}$$

Assume that there are N levels of epithermal positrons, then for the k_{th} level, the recursively coupled equations are

$$\frac{1}{\alpha_k}\frac{dI_k^+}{dx} = -\frac{\gamma_{el}(E_k)}{2}(I_k^+ - I_k^-) - (\gamma_{in}(E_k) + \gamma_a(E_k))I_k^+ + \frac{S_k(x)}{4\pi}, \tag{3.28}$$

$$\frac{1}{\alpha_k}\frac{dI_k^-}{dx} = -\frac{\gamma_{el}(E_k)}{2}(I_k^+ - I_k^-) + (\gamma_{in}(E_k) + \gamma_a(E_k))I_k^+ + \frac{S_k(x)}{4\pi}. \tag{3.29}$$

where α_k is the inverse of the cosine of the average scattering angle of the k_{th} level.

The source term for an intermediate k_{th} level is ($k \neq 1$ or N)

$$S_k(x) = 2\pi\gamma_{in}^{k+1,k}(E_{k+1})(I_{k+1}^+ + I_{k+1}^-) + 2\pi\gamma_{in}^{k-1,k}(E_{k-1})(I_{k-1}^+ + I_{k-1}^-), \tag{3.30}$$

i.e., positrons inelastically scattered from the $k-1$ and $k+1$ levels contribute to the source term of the k_{th} level.

For the next to the topmost epithermal level

$$S_1(x) = S(x) + 2\pi\gamma_{in}^{2,1}(E_2)(I_2^+ + I_2^-). \tag{3.31}$$

and for the N_{th} level

$$S_N(x) = 2\pi\gamma_{in}^{N-1,N}(E_{N-1})(I_{N-1}^+ + I_{N-1}^-), \tag{3.32}$$

here, the energy gain process from the thermal level is neglected.

For epithermal positrons in each level, the net current density of the scattered positrons is given by

$$J_{ek}(x) = \frac{2\pi}{\alpha_k}(I_k^+ - I_k^-), \tag{3.33}$$

and the corresponding density of the scattered positrons is

$$n_{ek}(x) = \frac{2\pi}{v_k}(I_k^+ + I_k^-), \tag{3.34}$$

where v_k is the average velocity of the k_{th} level.

In terms of $n_{ek}(x)$, equations (3.28), (3.29) can be written as

$$D_{ek}\frac{d^2n_{ek}(x)}{dx^2} = [\gamma_{in}(E_k) + \gamma_a(E_k)]v_k n_{ek}(x) - S_k(x). \tag{3.35}$$

with the effective diffusion coefficient

$$D_{ek} = \frac{v_k}{\alpha_k^2[\gamma_{in}(E_k) + \gamma_{el}(E_k) + \gamma_a(E_k)]}, \tag{3.36}$$

and the source profiles are

$$S_1(x) = S(x) + v_2\gamma_{in}^{2,1}(E_2)n_{e2}(x), \tag{3.37}$$

$$S_k(x) = v_{k+1}\gamma_{in}^{k+1,k} n_{ek+1} + v_{k-1}\gamma_{in}^{k-1,k} n_{ek-1}, (k \neq 1 \text{ or N}), \tag{3.38}$$

$$S_N(x) = v_{N-1}\gamma_{in}^{N-1,N} n_{eN-1}. \tag{3.39}$$

The thermalized positrons come from the inelastic energy loss process of the N_{th} level

$$S_t(x) = 2\pi\gamma_{in}^{N,t}(E_N)(I_N^+ + I_N^-). \tag{3.40}$$

and their diffusion equation is eq.(1.9)

The correlated equations (3.35)-(3.40) are very difficult to solve analytically in most cases. With some simplifications, researchers have been able to solve the problem for hot electrons. One possible way is by utilizing matrix methods which are suitable for the above equations. Some many-level examples are given by, e.g, Mahan(1985), here we will be concerned only with an analytical solution for a three-level example, i.e. two levels for the epithermal positrons, and one level for the thermalized positrons.

Let the space of interest be semi-infinite and have a totally absorbing boundary. Then the Green's function is given by eq.(3.14). No energy gain inelastic scattering events will be considered. It is found from eqs.(3.35)-(3.40) that for a three-level model, the topmost epithermal positron level has a density

$$n_{e0}(x) = \frac{1}{v_0\gamma_{in}(E_0)x_0'}[e^{-x/x_i} - e^{-\beta_{e0}x}], \tag{3.41}$$

where $x_0' = (x_i^2\beta_{e0}^2 - 1)/x_i\beta_{e0}^2$.

The reemitted fraction from the topmost level is thus

$$J_{e0} = \frac{D_{e0}\beta_{e0}^2}{v_0\gamma_{in}(E_0)}\frac{1}{1+\beta_{e0}/\beta_i}, \tag{3.42}$$

and the source of the second level epithermal positrons from the inelastically scattered fraction of the topmost level is

$$S_1(x) = \gamma_{in}(E_0)v_0 n_{e0}(x). \tag{3.43}$$

From which, the density of the second level epithermal positrons is

$$n_{e,1}(x) = \{D_{e,1}x_0'[\frac{e^{-\beta_i x} - e^{-\beta_{e,1}x}}{\beta_{e,1}^2 - \beta_i^2} - \frac{e^{-\beta_{e,0}x} - e^{-\beta_{e,1}x}}{\beta_{e,1}^2 - \beta_{e,0}^2}]\}^{-1}, \tag{3.44}$$

with the reemitted fraction of this level as

$$J_{e,1} = \frac{1}{(1+\beta_{e,1}/\beta_i)(1+\beta_i/\beta_{e,0})(1+\beta_{e,1}/\beta_{e,0})}. \tag{3.45}$$

and the inelastically scattered (i.e., thermalized) fraction

$$S_t(x) = \gamma_{in}(E)v' n_{e,l}(x). \tag{3.46}$$

Finally, we obtain the reemitted thermal positron fraction

$$J_t(x) = \frac{\beta_{el} + \beta_{e0} + \beta_t + \beta_l}{(1+\beta_{e0}/\beta_l)(1+\beta_l/\beta_{e1})(1+\beta_t/\beta_{e,0})(\beta_t+\beta_1)(1+\beta_t/\beta_{e,1})(1+\beta_{e,1}/\beta_{e,0})}. \tag{3.47}$$

Assuming the inelastic scattering is dominant for epithermal positrons, we have plotted the source profile for all the three levels in fig.3.4 and the reemitted fractions of each level in fig.3.5. Fig.3.6 shows the experimental data of Nielsen (1987) for two epithermal levels of positrons in Al, i.e., those having axial energies between

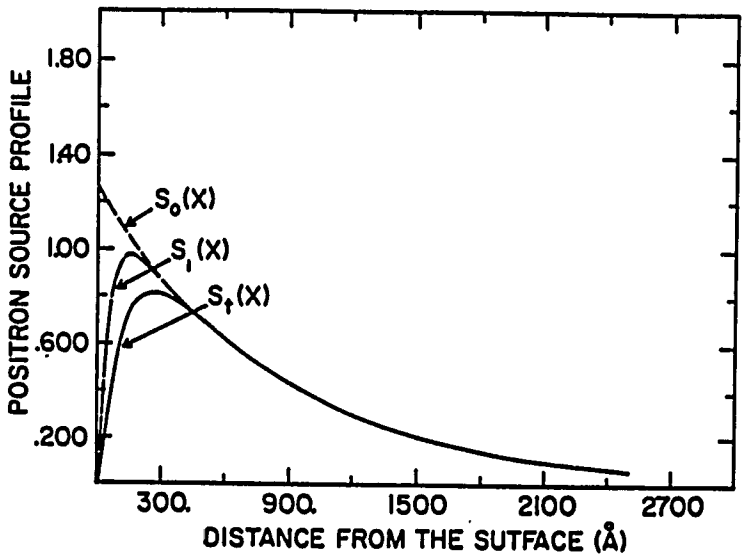

Fig.3.4 Source profiles for implantation depth ~ 800Å, $\beta_{e0} = 1/50$Å, $\beta_{e1} = 1/100$Å and $\beta_t = 1/1000$Å. $S_0(x), S_1(x)$, and $S_t(x)$ represent the topmost and second level epithermal positrons and the thermal positrons.

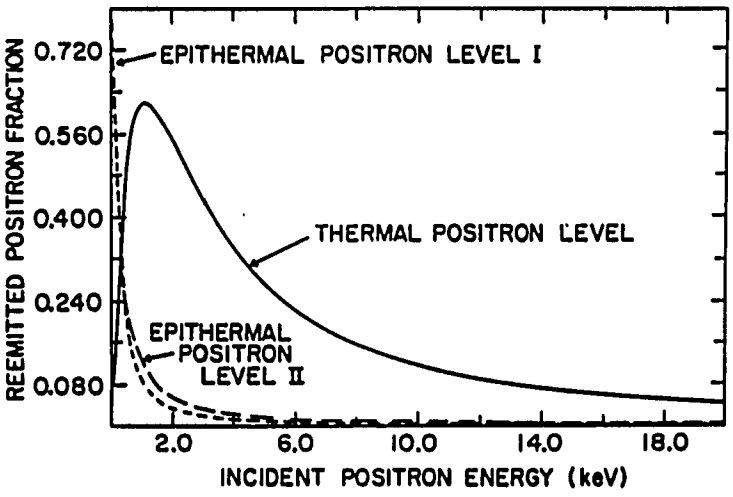

Fig.3.5 The surface returned fraction of the three levels. The parameters are the same as that for fig.3.4.

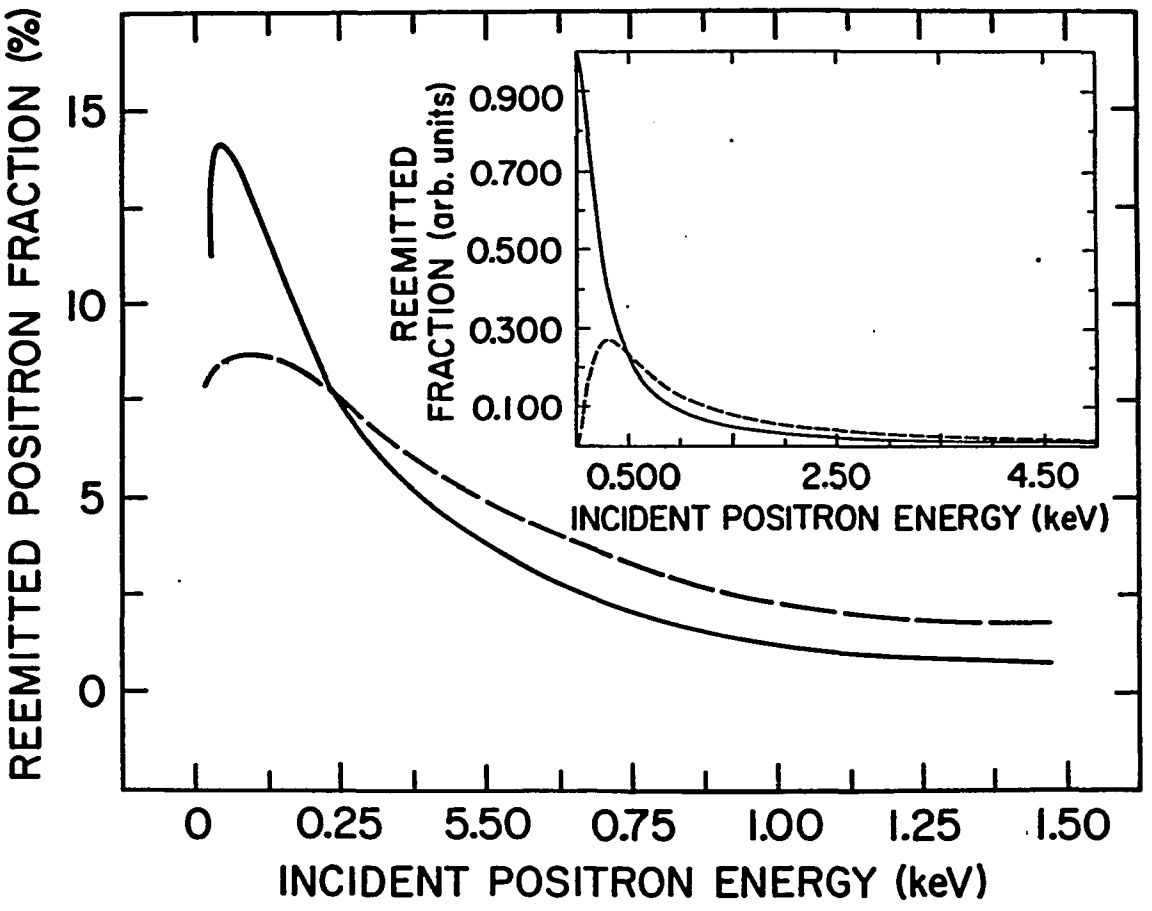

Fig.3.6 The measured reemitted epithermal positrons from an Al(111) surface with axial energies $1 < E < 2$ eV (the solid line), and $E < 1$ eV (the dashed line). The inset is from our model, $\beta_{e0} = 1/20\text{Å}, \beta_{e1} = 1/50\text{Å}$ and $\beta_t = 1/1000\text{Å}$. The solid line is the first epithermal level; the dashed line is the second epithermal level.

1−2 eV, and those with axial energy < 1 eV. The inset is from our model which qualitatively agrees with the experimental data. The depletion of reemission in the experimental data at 1 eV< E < 2 eV could be due to the reemission of higher energy epithermal positrons but it should be noted that our model itself is also very simplified in many aspects.

3.1.3 Application to metal bilayer systems

The treatment of epithermal positrons has important implications in some real physical situations. A bimetallic thin film is an especially interesting case. As shown in fig.3.7, its geometrical structure presents a positron with a potential step due to the charge transfer across the junction of the two adjoining layers. Positrons experience an acceleration field when crossing to the lower potential side. The dipole layer is thin enough to neglect any other scatterings during the acceleration, so relative to material 2, material 1 has an extra energy level related to the potential step.

The simple potential step in fig.3.7 is the starting point for treating a spatially extended electric field. An arbitrary potential produced by an electric field can be divided into many similar potential steps as shown. With this picture, positron transport in an electric field can be treated in more detail with both the drift motion and the possible positron heating effects taken into account.

It is worth noting that including epithermal positron effects is essential in the thin film examples (Gidley and Frieze, 1988), not only because of the possible strong field effects, but also because the dimensions concerned are almost comparable to or even smaller than the thermalization lengths of positrons, causing epithermal positrons to play an important role.

In the following treatment, only the dipole layer acceleration ($V_0 > 0$ in fig.3.7) will be concerned, because this is the physically more important case. Epithermal

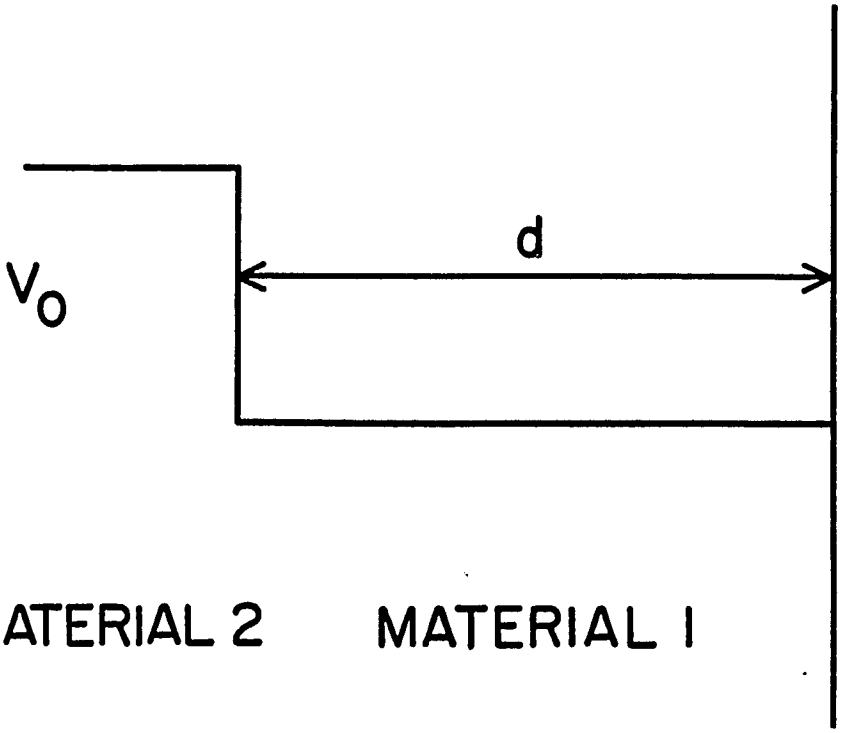

SCHEMATIC REPRESENTATION
OF AN ARBITRARY POTENTIAL

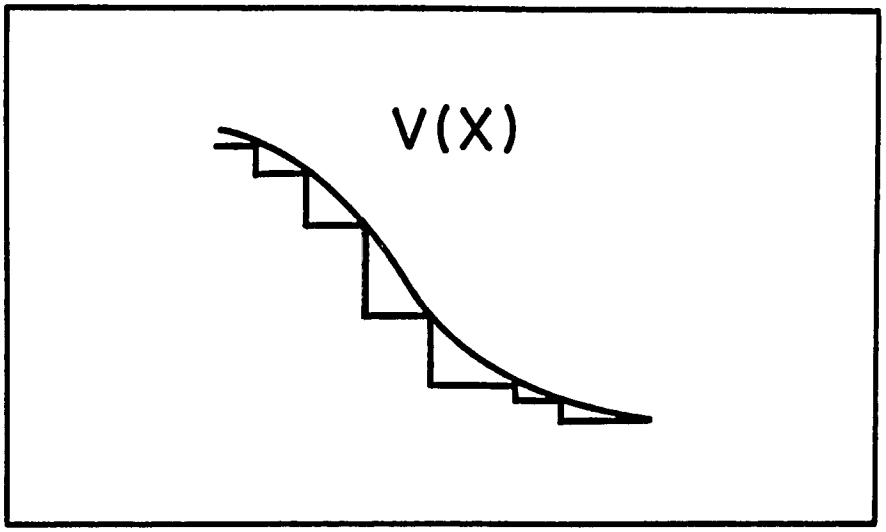

Fig.3.7 A potential step model for a bimetallic structure. The inset is for an arbitrary potential represented by a series of steps.

positron effects as the positrons stop in the substrate are also neglected to simplify the treatment. So there will be one thermal level in material 2, and one thermal and one epithermal level due to the potential step in material 1. Positrons are described by the implantation profile at the epithermal level in material 1 and at the thermal level in material 2.

For positrons in material 1, the solution can be obtained with the Green' s function for a totally absorbing boundary.

$$G(x,x') = A(e^{\beta x} - e^{-\beta x}), \text{for } x < x'$$

$$G(x,x') = A(e^{\beta x} - e^{-\beta x}) + (1/2\beta D)[\exp(-\beta(x-x')) - \exp(\beta(x-x'))], \text{for } x > x' \tag{3.48}$$

where A is a constant.

In this section, the derivative Gaussian implantation profile eq.(1.8) will be used with eq.(3.48). The density of the epithermal level in material 1 is obtained as

$$n_{e1}(x) = A[1-\exp(-\beta_i d)^2](e^{\beta_e x} - e^{-\beta_e x}) + \frac{e^{-\beta_e x}}{2\beta_e D_e}[1-\exp[\beta_e x - (x/x_i)^2] + \beta_e I_1(x)] +$$

$$\frac{e^{-\beta_e x}}{2\beta_e D_e}[1 - \exp[\beta_e x - (x/x_i)^2] - \beta_e I_2(x)], \tag{3.49}$$

where $I_1(x) = \int_0^x e^{\beta_e y - (y/x_i)^2} dy, I_2(x) = \int_0^x e^{\beta_e y - (y/x_i)^2} dy$. The parameters β_e and D_e depend on the potential well depth V_0 and the width d shown in fig.3.7. The density of the thermal level can also be solved with the same Green's function and the source profile $S_{t1}(x) = \gamma_{in} v_2 n_e(x)$

$$n_{t1}(x) = A_t(e^{\beta_{t1} x} - e^{-\beta_{t1} x}) \int_0^d S_{t1}(x')dx' +$$

$$\frac{1}{2D_{t1}\beta_{t1}} \int_0^x (e^{-\beta_{t1}(x-x')} - e^{\beta_{t1}(x-x')}) S_{t1}(x')dx'. \tag{3.50}$$

where A_t is also a constant.

For positrons in material 2, the solution is obtained from a Green's function for a semi-infinite space

$$G(x,x') = (1/2\beta D)[\exp(\beta(x-x')) - \exp(-\beta(x-x'))] + Be^{-\beta x}, \text{for } x < x'$$

$$G(x,x') = Be^{-\beta x}, \text{for } x > x'. \tag{3.51}$$

where B is a constant.

From which the density of thermal positrons at side 2 is solved as

$$n_{t2}(x) = B\exp(-\beta_{t2}x) + \frac{e^{-\beta_{t2}x}}{2\beta_{t2}D_{t2}}[\exp[\beta_{t2}x - (x/x_i)^2] - \beta_{t2}I_3(x)]$$

$$-\frac{e^{-\beta_{t2}x}}{2\beta_{t2}D_{t2}}[\exp[\beta_{t2}x - (x/x_i)^2] + \beta_{t2}I_4(x)], \tag{3.52}$$

where $I_3(x) = \int_x^\infty e^{-\beta_{t2}y-(y/x_i)^2}dy, I_4(x) = \int_x^\infty e^{\beta_{t2}y-(y/x_i)^2}dy.$

Material 1 and material 2 are connected by the flowing current matching condition (Mahan, 1985), here the thermal level in side 1 is actually a new level relative to side 2. Assume that the density of thermal positrons from side 1 at the interface position is zero; only as one moves towards the overlayer surface will the density of the 'new' level begin to change due to the inelastic scatterings in the epithermal level of side 1. Let $\beta_{t1} = \beta_{t2}$ and $D_{t1} = D_{t2}$ then equations (3.49)-(3.52) are solved which give the flux of epithermal and thermal positrons reemitted from the surface

$$J_e = 2\beta_e D_e A[1 - \exp(-d/x_i)^2]. \tag{3.53}$$

$$J_t = 2\beta_t D_t A_t \int_0^d S_{t1}(x')dx'. \tag{3.54}$$

We have plotted eqs.(3.53) and (3.54) in fig.3.8 and fig.3.9 with thermalization length 100Å and diffusion length 2000Å. Fig.3.8 shows the reemitted epithermal

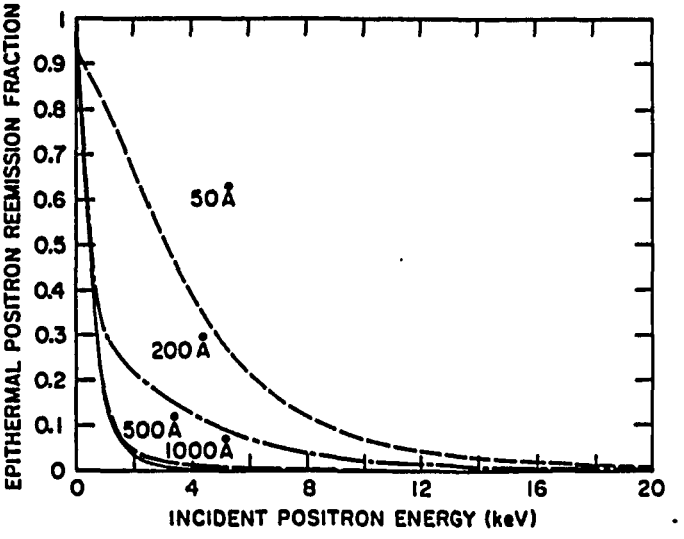

Fig.3.8 The surface returned epithermal positron fractions from a bilayered system with positron thermalization length 100Å and diffusion length 2000Å for different thicknesses of the overlayers.

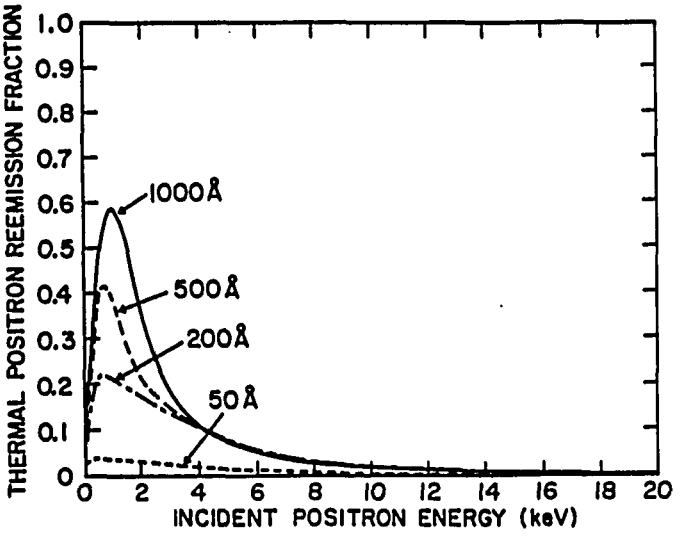

Fig.3.9 The surface returned thermal positron fractions from a bilayered system with positron thermalization length 100Å and diffusion length 2000Å for different thicknesses of the overlayers.

positron fractions for different thicknesses of the overlayer. Epithermal positrons due to the interface dipole are prominent in the 50Å and 200Å cases. For surface thicknesses far greater than the mean thermalization length 100Å, this effect becomes negligibly small except at low positron incident energies as is evident in the 500Å and 1000Å cases. The corresponding thermal positron reemission fractions , however, still exhibit observable differences (fig.3.9). This is simply due to the large thermal positrón diffusion length (2000Å) that is used. Only if the overlayer thickness is far greater than the thermal positron diffusion length will the result be close to a one-component system discussed previously.

The contribution of the interface dipole to the epithermal positrons can be further seen by subtracting the thick layer result (we have chosen 1000Å) from the thin layer results (fig.3.10). The resonant structure here suggests that epithermal positrons may be a potential tool in investigating the interface properties, especially with the development of positron microscope techniques.

At this point, we would also like to make a comparison between the exponential and derivative Gaussian profile results. In fig.3.11a and 3.11b, the reemitted epithermal and thermal positron fractions have been plotted with the two different implantation profiles. It is seen that they qualitatively agree with each other, except that the reemission fraction for the derivative Gaussian profile falls faster with increasing incident energies.

The last point which should be mentioned is, unlike what has been done with the so-called "topmost interval analysis" (Bernasconi et al, 1988), our model is not concerned with the elastic peak attenuation but with the overall thermalization and energy loss of a range of hot positrons. If optical phonon and electronic energy losses are neglected, the quasielastic acoustic phonon scattering in the "topmost interval analysis" will actually be the dominant inelastic energy-loss channel in our model.

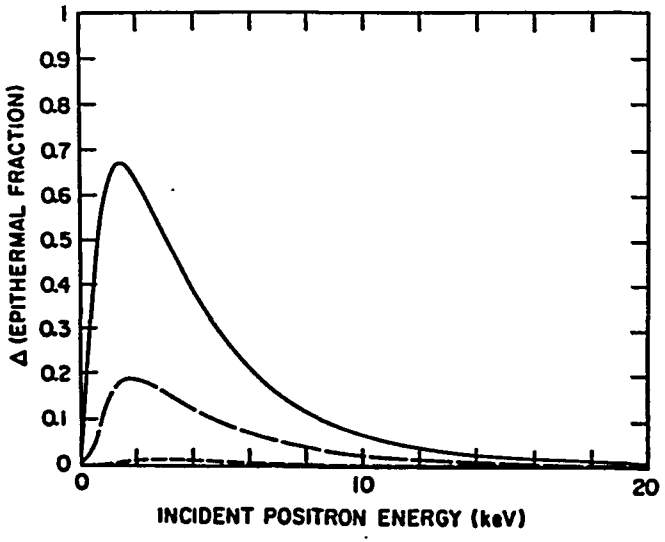

Fig.3.10 The difference of surface returned epithermal positron fractions of the 50 (solid line), 200 (long dashed line), and 500 Å (short dashed line) overlayer thicknesses from the 1000Å case.

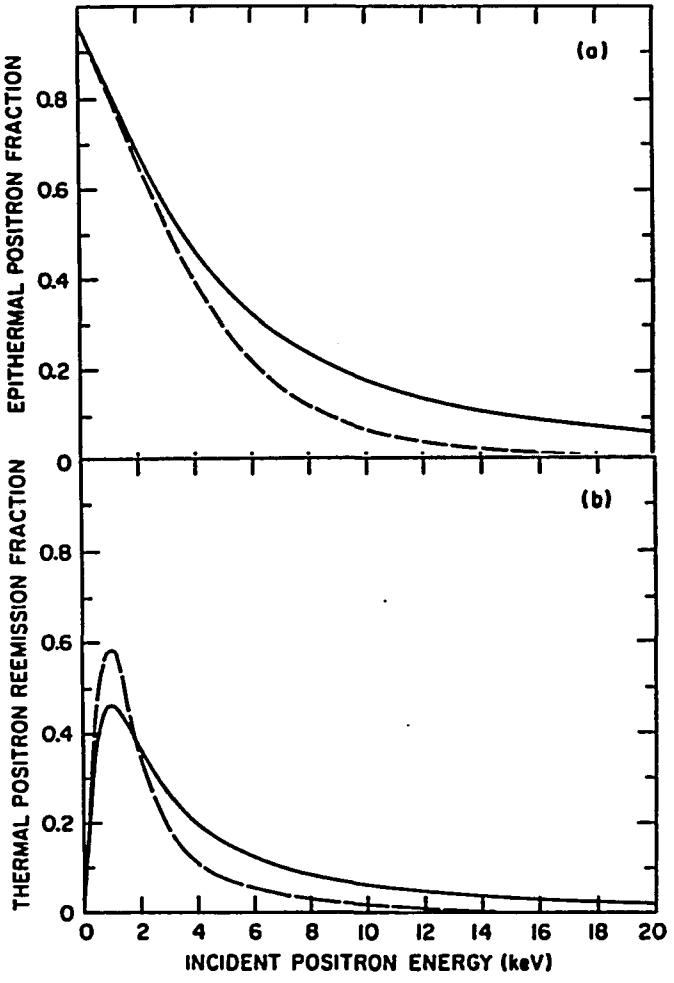

Fig.3.11 a) Comparison of the surface returned epithermal positron fractions for 50 Å surface layer from a derivative Gaussian (dashed line) and exponential (solid line) stopping profile. b)Comparison of reemitted thermal positron fractions for 1000 Å surface layer from a derivative Gaussian (dashed line) and exponential (solid line) stopping profile.

§3.2 Measurement of Positron Mobility in Thermally Grown SiO_2

Positron mobility in SiO_2 is an important quantity because of the recent interest (e.g., Lynn et al, 1989) in studying the MOS structure with slow positrons. Previous techniques applied for measuring this quantity are limited by their sensitivity to the small magnitude of positron mobility in the oxide layer. The present measurement makes use of the Doppler broadening technique in the sandwiched structure of MOS.

In this study, positrons with 2.5 keV incident energy are implanted into a n-type MOS sample with Al(50nm)/SiO_2(50nm)/Si(100). The dry oxide is thermally grown with a post-metallization Forming Gas (FG) anneal. The Doppler broadening parameters are measured under varying gate biases at room temperature. The centroid of the 511 keV photopeak of the annihilation γ rays is digitally stabilized, so that any systematic shift is minimized during the data acquisition.

At an incident energy of 2.5 keV, more than 80 % of the positrons will be stopped in the Al and SiO_2 overlayers for an exponential stopping profile (fig.3.12). A derivative Gaussian stopping profile eq.(1.8) will produce a slightly larger stopped fraction of positrons than the exponential profile. The electric field due to the gate bias will not affect the positrons in Al overlayer, and the small fraction of positrons implanted into the Si substrate have only a small contribution as discussed later. Changes in the Doppler broadening parameter versus gate bias is thus predominantly associated with the oxide and its boundaries.

The S-parameter as a function of varying external gate biases is shown in fig.3.13. There are several possibilities to explain the systematic dependence of the S parameter on the electric field strength. First of all, the positron motion in the oxide is affected by the electric field, which changes the fraction of positrons annihilating at different boundaries; and secondly, there is the possibility of Ps formation under the applied electric field, among which there exists the following

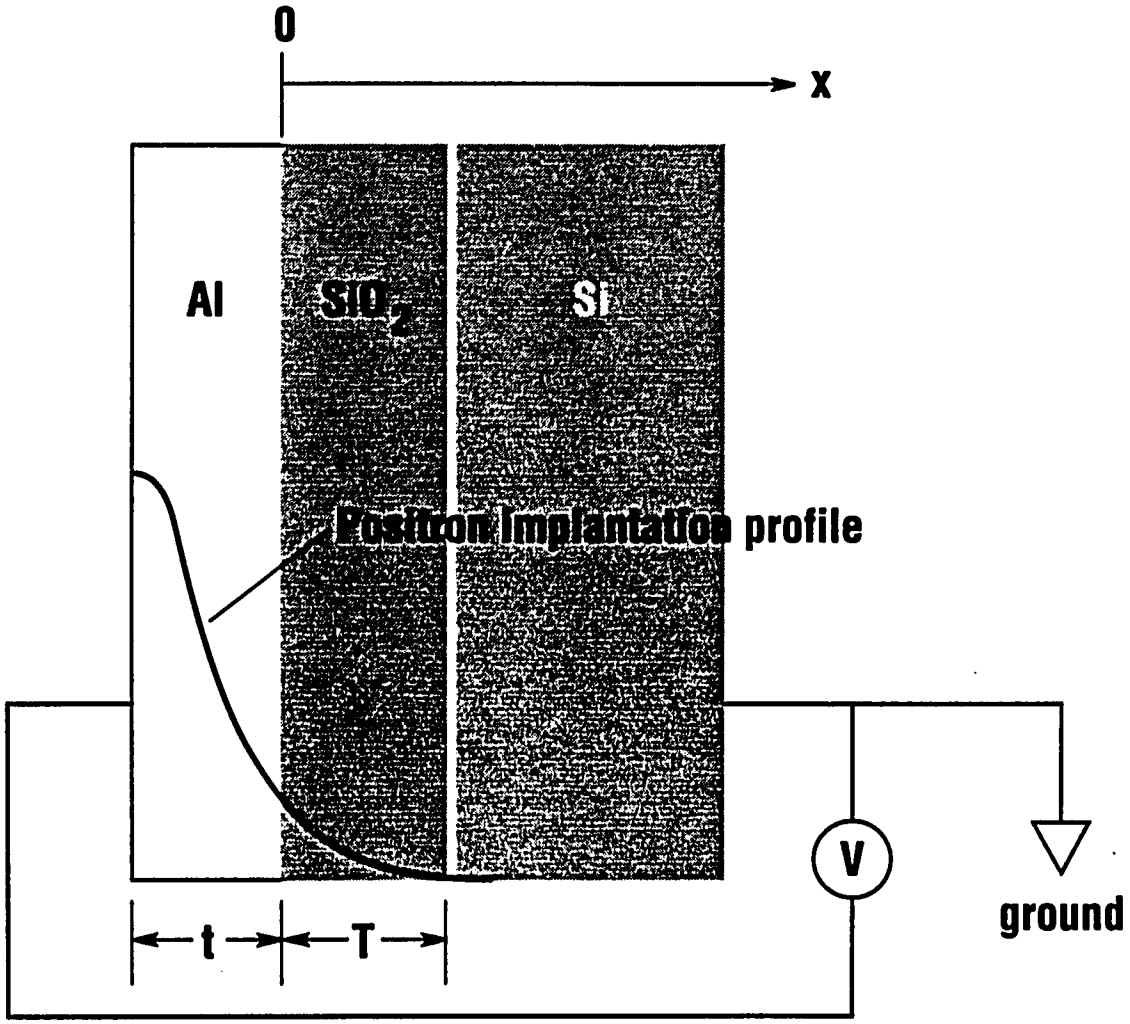

Fig.3.12 Schematics of a MOS structure, the positron stopping profile is also shown.

possibilities:

i). Ps formation through Ore mechanism or spur model could be affected by the presence of an electric field (Dupasquier, 1983). In the simplest picture, positrons in the Ore model will be driven by the electric field to overcome the Ore gap and form Ps, thus the Ps formation cross section increases with the electric field strength. In the spur model, the electron and the positron will be pulled apart from each other by the electric field thus impeding the formation of Ps. Hence, for spur model, the Ps formation cross section will decrease as the magnitude of the electric field increases. Ps formation in SiO_2 has been measured previously which suggests Ore mechanism will be important (e.g., Chen et al, 1988).

Ps formation is a small effect when compared to the electric field dependent diffusion in our measurement. The Ps formation can not explain the observation in fig.3.13. The measured S-parameter vs. gate bias depends only on the direction of the electric field instead of the magnitude of the electric field. Experimentally, we have also examined the ratio of the total-to-peak count (see section 2.2) of the positron annihilation γ-ray energy spectra. This ratio is found to be constant with gate bias variations, which shows that there is no observable changes in o-Ps formation associated with the electric field.

ii). There is another possibility of Ps being ionized by the static electric field present in the oxide. For an electric field ϵ (in atomic units), the ionization probability for a hydrogenic atom is proportional to $(1/\epsilon)e^{-\alpha/\epsilon}$, where α is a constant of unity order. In our setup, the electric field strength is less than 10^{-3} a.u., hence the ionization probability is too small to be observable.

iii). Ps moving in SiO_2 may experience the magnetic field arising from the relativistic effects. This magnetic field is estimated to be less than one Gauss for Ps with kinetic energy around 1 eV. The subsequent magnetic quenching probability

of Ps is hence negligible (Dupasquier, 1983).

A further possible contribution is from the electric field dependent generation of defects or defect trapping/detrapping. However, much stronger fields are necessary than the one used in this experiment. Therefore, only the electric field assisted diffusion of positrons in the oxide will be considered in the analysis. The data shown in fig.3.13 can be described using the following transport model for positrons in the oxide layer.

Both the Al/SiO_2 and the SiO_2/Si boundaries are assumed to be totally absorbing, i.e., the positrons reaching the boundaries will trap and annihilate in the region. An exponential positron implantation profile is used in terms of the coordinates shown in fig.3.12

$$P(x) = \frac{1}{x_i} e^{-(x+t_{Al})/x_i}, \tag{3.55}$$

where x_i is the mean implantation depth of 2.5 keV positrons $\sim$ 650Å, t_{Al} is the scaled thickness of the Al overlayer in terms of the SiO_2 density (1.22 : 1). The use of the exponential profile here is justified by the fact that we are dealing with a single incident positron energy. Only the relative fractions annihilating at the boundaries are important. These fractions are only slightly affected by the exact shape of the implantation profile. This is unlike the model fitting for positron incident energy vs. lineshape parameter (Uedono et al, 1988) where the implantation profile dependence on the energy plays a role in obtaining an reliable fit. This is especially true for the multilayered MOS structure.

The fractions of positrons annihilating at the Al/SiO_2 and the Si/SiO_2 interfaces are obtained through solving a drift-diffusion equation (Beling et al, 1987).

The fraction of positrons arriving at the Al/SiO_2 interface is

$$F_{Al} = \frac{\beta_i \exp(vT/2D - t_{Al}/x_i)}{T[(\lambda/D) - \beta_i{}^2 - \beta_i v/D]}[\frac{a}{\sinh(a)} - \frac{b}{\sinh(b)} + e^{-a}(b \cdot \coth(b) - a \cdot \coth(a))], \tag{3.56}$$

and at Si/SiO_2 interface is

$$F_{Si} = \frac{\beta_i \exp(-t_{Al}/x_i)}{T[(\lambda/D) - \beta_i{}^2 - \beta_i v/D]}[e^{-a}(\frac{a}{\sinh(a)} - \frac{b}{\sinh(b)}) + b \cdot \coth(b) - a \cdot \coth(a)], \tag{3.57}$$

where β_i is the inverse of x_i in eq.(3.55), λ is the annihilation rate of positrons in the SiO_2, $v = \mu E$ is the drift velocity, and D is the diffusion coefficient of the positrons in field-free SiO_2 . The parameters a and b are given by

$$a = \beta_i T + vT/2D, \tag{3.58}$$

$$b = T[(\lambda/D) + (v/2D)^2]^{\frac{1}{2}}. \tag{3.59}$$

The resulting S-parameter is

$$S = \eta F_{Al} S_{Al} + \eta F_{Si} S_{Si} + \eta(e^{-t_{Al}/x_i} - e^{-(T+t_{Al})/x_i} - F_{Al} - F_{Si}) S_o + const, \tag{3.60}$$

where η is a scaling factor accounting for possible para-Ps or trapped positrons not affected by the electric field. The constant term is the contribution from positron annihilation in regions outside the electric field. Eq.(3.60) is fitted to the data shown in fig.3.13. The electric field present in the oxide layer changes with the external gate bias. The detailed partition of the applied potential between the Si and SiO_2 can be found for example in Sze (1981). We have used a linear relation between the electric field strength in the oxide and the external bias, V_G. This

approximation will be further discussed below in association with the uncertainty in the S-parameters.

Positron lifetime in single crystal quartz is $\sim$ 270 ps (Uedono et al, 1988). The corresponding lifetime in amorphous SiO_2 is longer (Laermans et al, 1989). We fitted eq.(3.60) to the data in fig.3.13 with a lifetime of 400 (50) ps. The actual obtained fitting parameter is λ/D from eq.(3.60), thus the uncertainty in mobility due to the lifetime value is less than 13%. The fitted mobility for positrons in SiO_2 is found to be $\sim$ 11 (6) $\times$ 10^{-3}cm^2/sec·V with a reduced chi-squared $\sim$ 2.2, the scaling factor $\eta \sim 0.98(0.03)$ and the electric field in the oxide $V_G \sim 59(5)$ Volts/nm. The interface S parameters from the fitting are : S_{Al}= 0.56(0.05), S_{Si}=0.47(0.03) if the oxide S_o is assumed to be 0.50.

Fig.3.14 shows a sample calculation for S parameter vs gate bias for positron mobilities of 10^{-3},10^{-2}, and 0.1cm^2/sec·V. Other parameters used in the calculation are close to the above fitted values. As is evident from the figure, for the 10^{-3}cm^2/sec·V case, the change in S is too small to resolve the positron mobility value within the given gate bias range. This presents a lower limit of the mobility that can be obtained with the current experiment, which is about 4 or 5 orders of magnitude smaller than the usual positron mobility in, e.g., semiconductors. For the 0.1 cm^2/sec·V case in fig.3.14, the S-parameter becomes saturated when the gate bias changed only by about 2 Volts indicating the high sensitivity of Doppler broadening technique towards the positron drift motion.

The above discussion concerns only the positrons inside the oxide layer. For a FG annealed MOS sample, the contributions from the Si surface will be small, though it is more uncertain for samples without FG annealing. The S-parameter dependence on gate bias for positrons with higher implantation energies (i.e., when more positrons are implanted into the Si) is also studied (Leung et al, 1991). It is

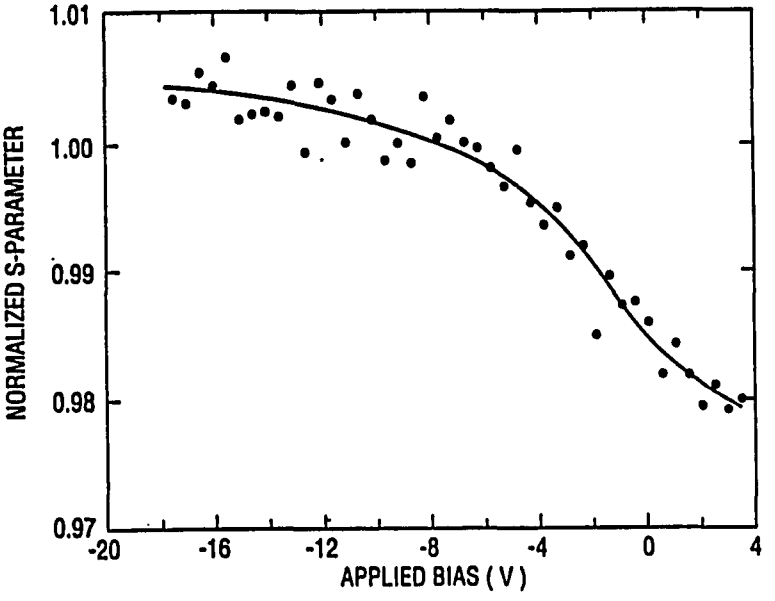

Fig.3.13 Variation of S-parameter under external gate bias for 2.5 keV incident energy positrons. Solid dots are the data points with typical statistical errors of $\sim 10^{-3}$. The solid line is the fitted result.

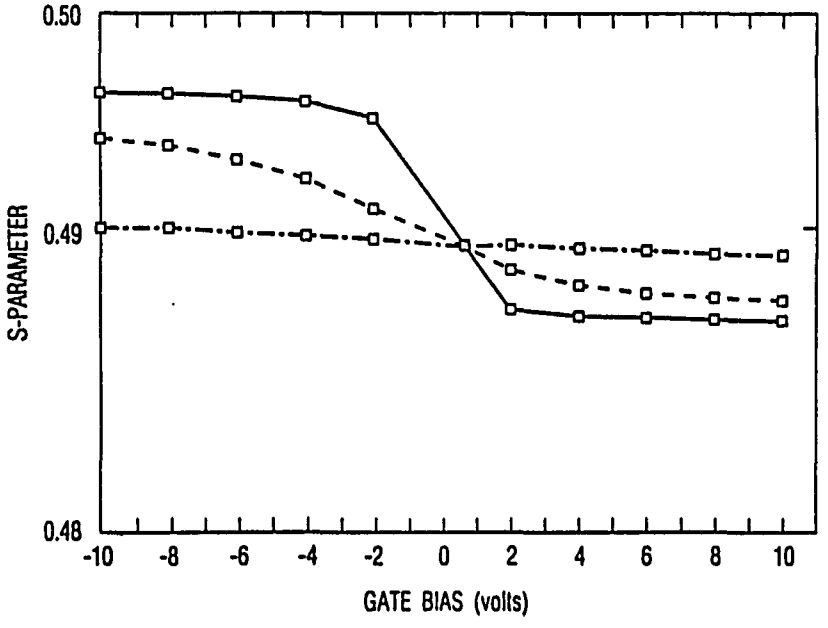

Fig.3.14 The model calculation of S vs gate biases for $\mu = 10^{-3}$/ (dot-dashed line), 10^{-2} (dashed line) and 10^{-1} (solid line) $cm^2/sec \cdot V$.

found that the S-parameter will decrease from Si bulk value to a lower value related to the SiO_2/Si interface as the gate bias varies from positive to near zero, which can be explained by the electric-field dependent positron diffusion in Si. However, as the gate bias further decreases towards a more negative voltage, the FG-annealed sample will stay with the low S-parameter characteristic of the SiO_2/Si interface. For a sample without FG annealing, this S-parameter can increase to a much higher value possibly related to the increased hole presence at the interface. For a positron beam energy of 2.5 keV, the Si side positron induced S-parameter change is estimated to be of the order 10^{-3} for FG-annealed sample and is comparable to the statistical error. The mobility excluding Si effects may increase by 20% and can become 13 (6) $\times 10^{-3} cm^2/sec \cdot V$. This would correspond to a diffusion coefficient of $\sim 2.7 \times 10^{-4}$ cm^2/sec or a diffusion length of $\sim$ 35Å. The effective positron diffusion length in the oxide under the electric field can also be deduced from the above parameters (Mills and Murray, 1980). Relative to the Al/SiO_2 interface, the effective diffusion lengths are 1400Å and 0.9Å respectively for -20 and 20 Volts gate biases.

The derived mobility value will depend on the oxide conditions (e.g. growth method, defect concentration, etc.), positron thermalization effect, as well as the approximations used in the model. For example, the possible uncertainties with the implantation profile or the electric field in the oxide are convoluted with the uncertainty in the S-parameter in the fitting model. These systematic effects will increase the error bar in the mobility reported here which is estimated to be 13(10) $\times 10^{-3} cm^2/sec \cdot V$.

The measured electron mobility (Hughes, 1973) in SiO_2 is $\sim$20 $cm^2/sec \cdot V$ and the hole mobility(at 200 K) (Hughes, 1977) is of $10^{-6} cm^2/sec \cdot V$ The transport model for the former is governed by the electron-phonon interaction, where the mobility will decrease as temperature rises. For the hole, the mobility is dominated

by hopping and increases with increasing temperatures. Our measurement has also been performed at$\sim$ 35 K where the positron mobility decreases with respect to the room temperature value indicating positron transport is also possibly trap-modulated. This would justify the use of the diffusion equation in evaluating the small positron mobility here.

Thus the positron mobility in SiO_2 is deduced from the Doppler broadening of positron annihilation γ-ray energy measurement. The mobility obtained $13(10) \times 10^{-3}cm^2/sec{\cdot}V$ represents a more accurate value than that obtained from previous studies. The multilayered structure of the sample provides a good example of Doppler broadening studies even when the positron mobility is very small. This is because of the relatively large difference of S-parameters at the boundaries of the oxide layer(S_{Al}=0.56, S_{Si}=0.47). The thickness of the oxide layer is also important to provide the sensitivity of the technique. A thicker oxide layer may be preferred, though a larger gate bias will be needed to induce the same observable S-parameter changes. A good understanding of the positron mobility in SiO_2 should provide another means of studying the oxides. For example, positron mobility can be measured when the oxide is under ionizing radiation or when the oxide has been grown epitaxilly, where one would expect a larger mobility owing to the decrease in the defect concentrations. The overall quantitative study of MOS system using variable energy positron beams will also benefit upon an improved knowledge of the positron mobility in the oxide layer.

§ 3.3 Centroid Shift Measurement of Positron Transport at a Si Surface

Electric field induced positron drift motion is measured in the previous example by the subsequent annihilation site changes of the positrons. There are complications involved there that one has to be careful such as the possible Ps formation induced by the electric field. In this section, positron drift motion is measured

by the subsequent annihilation γ-ray energy shift. This technique will be mostly sensitive to positrons in drift motion at annihilation.

As a positron enters the sample, it is rapidly thermalized and travels with a velocity which depends on its thermal energy and the effects of the electric field in the depletion region. The width of the 511 keV peak is almost entirely due to the much larger electron velocities. However, if, e.g., the n-type sample is reversely biased, a depletion region can occur at Si surface with a dimension larger than the positron diffusion length. Positron velocities will then have a directionality imposed by the electric field, and the centroid shifts in the subsequent annihilation γ-ray energies will be characteristic of the positron velocities. If the n-type sample is forward biased, an accumulation region, which affects little of the positron near-surface transport, is induced, and there will essentially be no change in the centroid position. If the positron drift velocity is v, it will shift the centroid of the γ-ray of mean energy E by an amount of $\Delta E/E = v/2c$. Considering positron mobility in Si $\mu \sim 70\text{cm}^2/\text{sec}\cdot\text{V}$ (Mills and Pfeiffer, 1977) and an electric field of 10^4 V/cm, positron drift velocities are on the order of 10^6 cm/sec. It is larger than positron drift velocity in the oxide, which is estimated as $\sim 10^4$ cm/sec. Thus for positron annihilations in Si, the relative centroid shift is of the order of 2×10^{-5}, or about 10 eV energy shift for the 511 keV annihilation line. The centroid shift due to the positron drift motion in the oxide, on the other hand, will only be about 0.1 eV which is negligible when most of the positrons are implanted in the Si (with positron energies beyond 3 keV in the present case). There is also an interesting possibility that Ps formation in the oxide may contribute to the centroid shift of annihilation γ rays. For example, positrons may be driven to overcome the Ore gap forming Ps under the electric field. The Ps formed may still possess a momentum in the same direction as the initial positron drift motion. The subsequent Ps annihilation

can thus occur from a moving frame inducing centroid shift of annihilation γ rays. However, it has been shown that Ps will slow down rapidly in solids (Kubica and Stewart, 1975) and possesses almost zero momentum upon annihilation. So no account needs to be taken of Ps during the centroid shift measurement even if its production is E-field dependent.

The centroid shift measurements of the γ-ray energy spectra produced by positron annihilation in MOS structure will be carried on two samples. One had a n-type Czochralski grown Si(100) substrate, upon which 500 Å of wet oxide was grown and 500 Å of Al overlayer evaporated without post-metal anneal. The substrate doping density was $\sim$ 2-6 $\times 10^{14}/cm^3$. The second sample had a p-type Si substrate upon which 500 Å oxide was grown and 500 Å of Al was evaporated. The substrate doping density was $\sim$ 3-7 $\times 10^{15}/cm^3$.

During the measurement, the substrate is always grounded and the Al overlayer is forward or reversely biased at 10 volts for the n-type sample and 6 volts for the p-type sample. Variable energy positrons are implanted into the samples. The corresponding annihilation γ-ray spectra are then analyzed to obtain the relative centroid shifts caused by positive or negative bias conditions as described in section 2.2. The positron beam facility used in the experiment is the same as that measuring the positron mobility in the oxide. It should be noted that the Ge detector here is facing the direction of the applied electric field on the MOS sample and hence provides an optimal measure of the centroid shift.

In the present set up, a Be^7 radioactive source (which emits 477 keV γ-rays) is used as a reference. The centroid position from the positron annihilation γ-rays (511 keV) with respect to the Be^7 477 keV peak is decided by calculating the first moment of the γ-ray energy distribution from a pulse height analyzer. To avoid systematic centroid drifts during the measurements, we alternately measured the

relative centroid shifts at the positive and negative bias conditions (10^6 counts for each bias) at a given incident positron energy. The positron incident energy is varied to obtain the depth-dependent centroid shifts for both samples. Since the accumulation of the majority carriers at the Si surface does not affect the positron diffusion behavior in the bulk Si, the measured centroid shifts will only be treated as related to the depletion layer at the Si surface.

Fig.3.15 shows the measured centroid shifts for an n-type sample as a function of positron incident energy in the range of 5-40 keV. Fig.3.16 shows the results for a p-type sample in the range of 5-30 keV. The positrons that contribute to the measured centroid shift are those that annihilate when under the effect of the applied electric field. Positrons which annihilate in the field-free region will have negligible contributions to the measured centroid shift. In addition, if the positron is in a certain immobile state such as a trapped state, the centroid shift measurement will see no differences under different bias conditions. The insensitivity of the centroid shift measurement towards the "immobile" state indicates that if this technique is used in combination with other positron techniques such as the S-parameter measurement, then positron trapping behavior may be distinguished from the diffusion behavior. Since the measurement carried out here will not include the contributions from the trapped state while the S-parameter measurements are a convolution of the positron diffusion behavior and the electronic environment in which the positron annihilates (e.g. bulk delocalized state, vacancy and interface trapped state).

Another case of potential interest is when positrons are accelerated by the electric field so that they may become heated when the electric field is strong enough. If this occurs near the SiO_2/Si interface region, one may observe the heating effects from the centroid shift measurements. However, this would require a better knowledge of, e.g., positron implantation profile and the electric field configuration

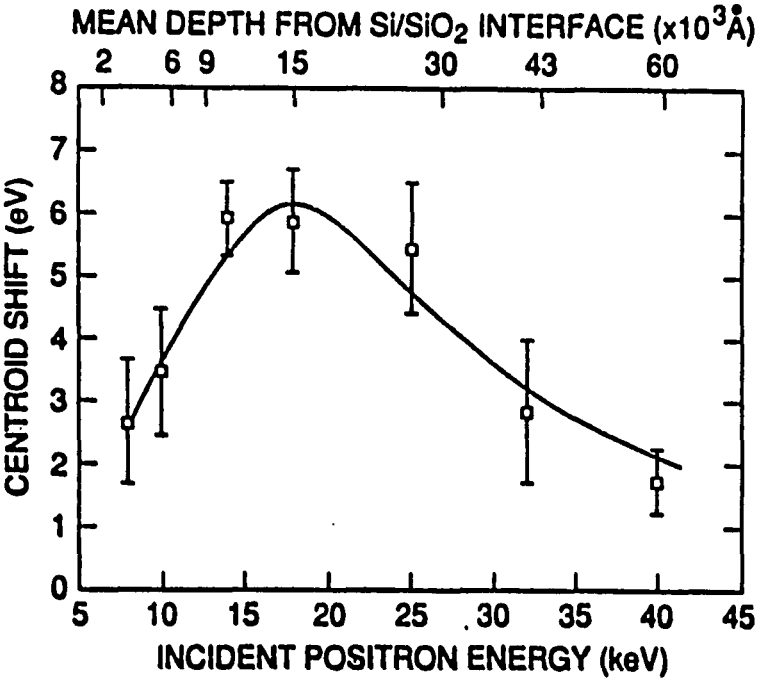

Fig.3.15 The centroid shift vs positron incident energy for the n-type MOS sample. The solid line is the fitted result.

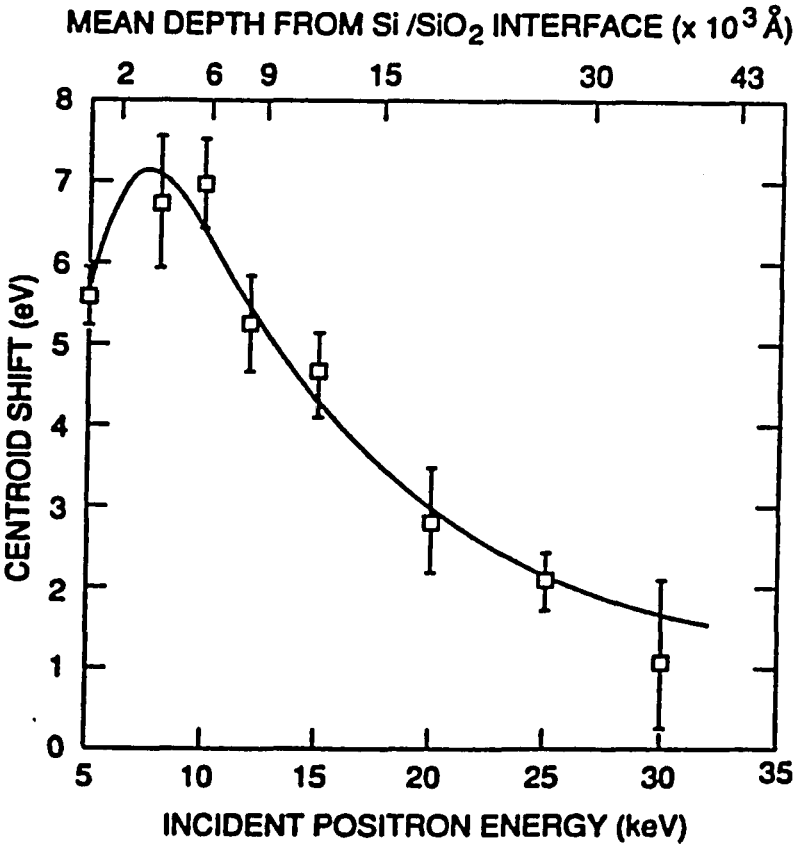

Fig.3.16 The centroid shift vs positron incident energy for the p-type MOS sample. The solid line is the fitted result.

at the Si surface.

In this work we have not considered positron heating effects and have assumed that the positrons annihilating beyond the electric field region will have zero contribution to the measured shift. The initial increase of the centroid shift in figs.3.15 and 3.16 with incident energy can be understood as due to the increase in the fraction of positrons that will annihilate in the electric field region. With further increases in the positron incident energy, more positrons will be implanted beyond the electric field region. Thus the fraction of the positrons that annihilate in the depletion region decreases, resulting in a smaller centroid shift.

For the n-type substrate a depletion region is formed for a bias of -10V with the electric field inside the bulk Si directing towards the SiO_2/Si interface, and the effective diffusion length of the positrons towards the interface will be larger than for the field-free situation. The $+10$V bias corresponds to the accumulation case and the bulk positron diffusion behavior is not affected. For the p-type substrate (fig.3.16) the opposite is true. The depletion region is formed when the sample is positively biased, and the electric field is directing away from the SiO_2/Si interface. The effective positron diffusion coefficient towards the interface is smaller than the field free case. The negative bias situation for this sample will have little effect on the positron bulk diffusion behavior because of the accumulation of the holes. The accumulation and depletion conditions reached under the applied bias are confirmed by comparing with the C-V curves of both samples. The effects of electric field enhanced diffusion and larger depletion layer length are clearly seen from Figs.3.15 and 3.16, where the n-type sample has a maximum centroid shift occurring at a much larger positron incident energy (18 keV) than the p-type sample (8 keV). We have used an effective diffusion length, L_{eff} to describe the positron mobility towards the interface and have approximated the electric field in the depletion region

as a constant. The derivative Gaussian distribution $P(x)$ eq.(1.8) is represented for the positron implantation profile. However, x_i is defined through $A(E-E_{ref})^{1.6}/\rho$, here A, ρ are the same as in eq.(1.7), except that E_{ref} is defined to account the fact that the Si surface is buried under the Al and the oxide layers. E_{ref} should correspond to an energy for positrons to be implanted to the SiO_2/Si interface.

We emphasize here that the exact shape of the stopping profile does not affect the estimations below. In fact, we have employed an exponential stopping profile and found the fitted results to be of the same order of magnitude. The depletion region has a width x_d, therefore the fraction of positrons that annihilate in the electric field region and contribute to the measured signal is

$$F = \int_0^{x_d} [1 - \exp(-x/L_{eff})] P(x) dx, \tag{3.61}$$

which can be evaluated to get

$$F = \frac{1}{L_{eff}} \exp(x_i/2L_{eff})^2 [\mathrm{erf}(x_d/x_i + x_i/2L_{eff}) - \mathrm{erf}(x_i/2L_{eff})] -$$
$$[1 - \exp(-x_d/L_{eff})] \exp[-(x_d/x_i)^2]. \tag{3.62}$$

Taking $E_{ref} = 0$, fig.3.17a shows eq.(3.62) for a fixed diffusion length and varying depletion layer lengths. Fig.3.17b shows a fixed depletion layer length and varying effective positron diffusion lengths. It is seen that the slope of the initial increase of the centroid shift is associated with the effective diffusion length of the positrons. A short diffusion length will correspond to a sharp rise to the maximum centroid shifts. When the diffusion length becomes comparable to the depletion layer length, the slope of the centroid shift as a function of incident positron energy begins to saturate. For a fixed positron diffusion length, a longer depletion layer

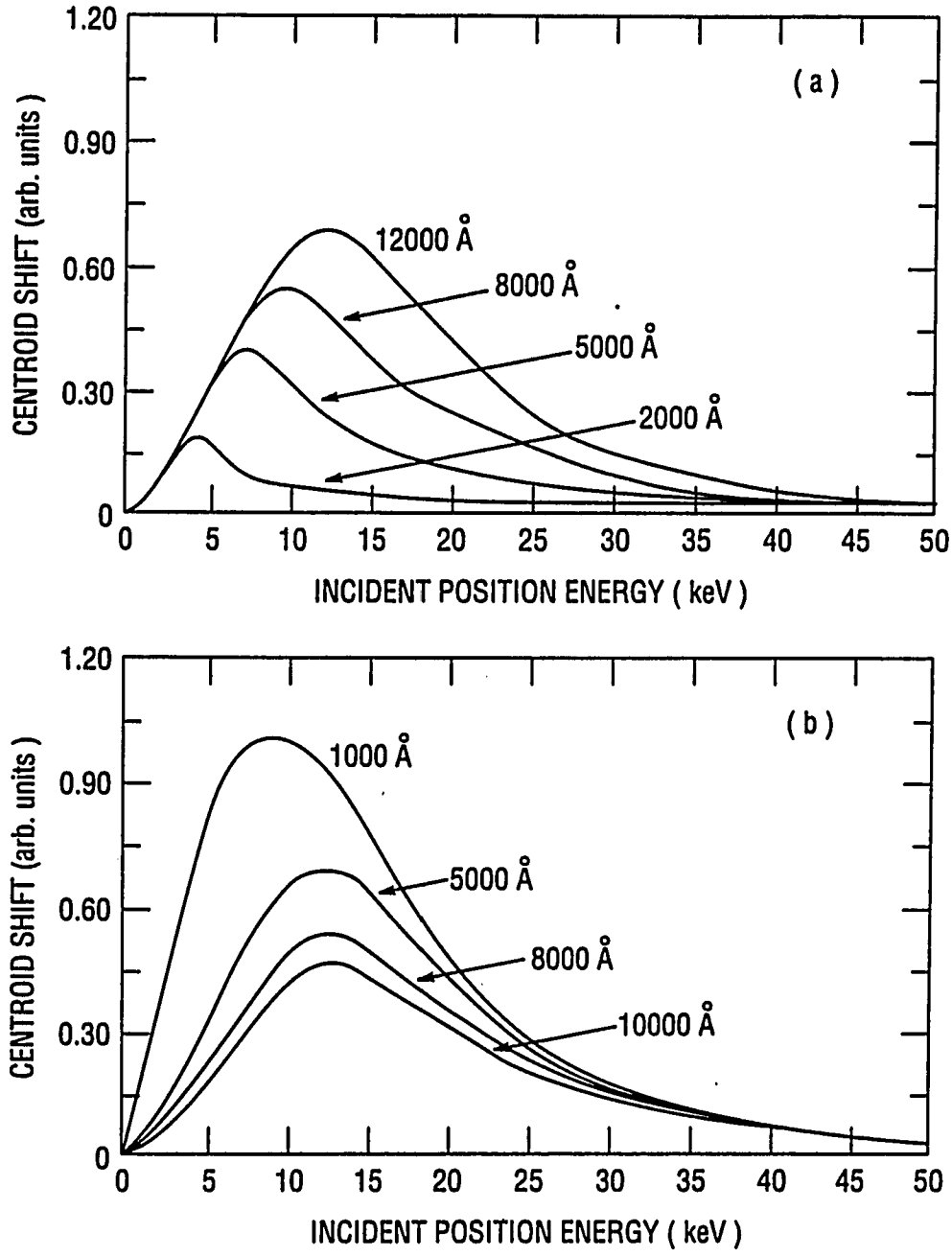

Fig.3.17 a) Model calculation for centroid shift at given positron diffusion length (5000 Å) but varying depletion layer lengths. b)Model calculation for centroid shift at given depletion layer length (12000 Å) but varying positron diffusion lengths.

means the peak position will be shifted towards the higher energy side, and more positrons will annihilate in the depletion zone and contribute to the signal. The height of the peak increases with increasing depletion layer length, though the slope of the initial increase is only slightly affected. Fig.3.17 shows that the centroid shift measurements are sensitive to the positron diffusion behavior in the electric field as well as the MOS geometry including the depletion layer conditions.

When fitting the experimental data, the fraction in eq.(3.62) has to be multiplied by the corresponding centroid shift, which will be determined by the position drift velocity. The parameters x_d, L_{eff}, and positron drift velocity are free to change during the fitting. The fitted effective diffusion length is 5600(50)Å, while the depletion layer length is $16(2) \times 10^3$Å. For our sample, since the doping density is known, we can calculate the depletion layer width from (Sze, 1981)

$$W = \sqrt{4\epsilon_s k_B T \ln(N_A/n_i)/q^2 N_A}, \tag{3.63}$$

where ϵ_s is the dielectric constant, n_i is the intrinsic carrier density and N_A is the doping concentration. We obtain W $\sim 12000 - 18000$Å in agreement with our fitted value for the n-type sample. For the p-type sample, the fitted effective positron diffusion length is $3(1) \times 10^2$Å. The depletion layer width is $6(1) \times 10^3$Å, which also agrees with the calculated depletion layer width ~4-7 $\times 10^3$Å from eq.(3.63). The average electric field in the depletion zone can be estimated from the fitted effective diffusion length assuming that the field free diffusion length is $L_o \sim 2400$Å (Nielsen et al, 1985). Using a positron mobility in Si of $\mu \sim 70 \text{cm}^2/\text{sec}\cdot\text{V}$ (Mills and Pfeiffer, 1977), the effective diffusion length under an electric field E is given by

$$\frac{1}{L_{eff}} = \sqrt{\frac{\mu^2 E^2}{4D_+^2} + \frac{1}{L_o^2}} \pm \frac{\mu E}{2D_+}, \tag{3.64}$$

where the $\pm$ sign depends on whether the E-field is directing towards or away from the interface. From eq.(3.64) one obtains the electric field strength for the n-type sample as $\sim 3 \times 10^3$ V/cm and for the p-type sample as $\sim 1 \times 10^4$ V/cm. The average electric field strength is larger in the p-type sample than in the n-type sample because of the larger doping concentration(N_A) in the former sample, which gives a shorter depletion layer width as well as a larger surface band bending (Sze, 1981)

$$\Psi_s = qN_A W^2/2\epsilon_s, \tag{3.65}$$

It is worth noting that the electric field in the depletion region is not constant and is given by $E = E_0(1 - x/x_d)$ (Sze, 1981). This would result in a higher electric field close to the interface. This electric field gradient, along with the fact that the average electric field in the p-type sample is greater than that in the n-type sample is possibly the reason that the maximum centroid shift of the p-type sample is a little larger than the maximum centroid shift of the n-type sample.

In summary, we have measured the centroid shift of positron annihilation induced γ-rays in the presence of an electric field in both the n- and p-type substrate MOS samples. The results can be well represented by a positron diffusion model, and the effective positron diffusion length can be deduced. The results not only provide a better understanding of the physics of positron interactions with a multilayered structure, but will also be important in characterizing device quality. It will shed light on properties such as the hole mobility at the interface region. The optimum bias condition for the maximum positron charge collection at the interface is easily deduced from the results. This enables one to make positrons more sensitive to the interface region. It is possible to obtain information on the SiO_2/Si interface

trapping properties, positron heating effects, and the electric field configuration when a more quantitative study can be done.

Chapter 4

POSITRON INTERACTION WITH SURFACES

Variable energy positron beam technique has enabled the study of solid surfaces with positrons. Of the possible positron processes at the surfaces, we will be concerned with the positron surface reflection and trapping into the surface potentials. The quantitativeness of internal surface reflection is discussed in section 4.1, and a multiple-encounter picture for positrons to participate in the normal surface processes are suggested. Positron trapping into the image potential is discussed in 4.2 considering the role of the excited Rydberg states and the phonon mediation. An experimental study with PAES on an ionic solid KCl(100) surface is discussed in section 4.3. Finally, PAES application for the non-destructive evaluation of the ion sputtering damage on KCl(100) surface is discussed in section 4.4.

§ 4.1 The Multiple-encounter of Thermal Positrons with Surfaces

Thermal positrons returning to the surface can be reflected by the surface potential back into the bulk solids (Nieminen and Oliva, 1980) inhibiting the positrons participating in the surface escape processes.

This internal surface reflection has been demonstrated by Britton et al (1989) from positron and Ps emission measurements. The modelling of positron reflection by the surface potential is adopted from Nieminen and Oliva (1980), where a surface potential step accounting the positron surface workfunction (ϕ_+) is employed. The reflection and transmission of thermal positrons by this potential step is deduced to be of the same order of magnitude. In fact, the transmission coefficient used there is

$$\Pi = \frac{4[k_BT(k_BT - 2\phi_+)]}{\{k_BT - \phi_+ + [k_BT(k_BT - 2\phi_+)]^{1/2}\}^2}, \tag{4.1}$$

where k_BT is the thermal positron energy. Most recently, Brandes (1991) measured positron reemission yield from a thin Ni film and deduced the internal surface reflection coefficient as $R = 0.63 \pm 0.04$ consistent in order of magnitude with that predicated by eq.(4.1).

There is, however, questions related to the modelling of the surface potential by a simple potential step as in eq.(4.1). It is recognized that a potential well exists in between the vacuum and the solid which is responsible for the positron surface states on many metal and semiconductor surfaces. Though the dimension of the potential well is of the order $\sim$ 1Å (note that the thermal positron de Brogile wavelength is $\sim 62\text{Å}\sqrt{300/\text{T(K)}}$), it will significantly affect the positron reflection from the surface potential. The larger mismatch of the wavenumbers for a positron inside the solid and inside the potential well region will increase the quantum mechanical reflection by an order of magnitude. In fact, for a square potential well of depth V_0 at a zero workfunction surface, the transmission coefficient is

$$\Pi = [1 + \frac{1}{4}(\sqrt{\frac{k_BT}{k_BT + V_0}} - \sqrt{\frac{k_BT + V_0}{k_BT}})^2 \sin^2(\sqrt{\frac{2m(k_BT + V_0)a^2}{\hbar^2}})]^{-1}, \tag{4.2}$$

where m is the positron effective mass in solids, $\hbar$ is the Planck constant, a is the width of the potential well of the order of 1 Å, V_0 is about the Ps vacuum binding energy (6.8 eV). It can be seen that eq.(4.2) is approximately decided by $4k_BT/V_0$ which is about 10^{-2} in the temperature range of interest. The corresponding transmission coefficient will then be an order of magnitude smaller than that suggested by eq.(4.1) and the forementioned experimental results. For negative workfunction surfaces at high temperatures, the transmission coefficient can be around 0.1, but it

is much smaller than it would be from eq.(4.1). For positive workfunction surfaces, the reflection coefficient will be unity in terms of thermal positron reemissions even when there is a potential well present.

The experimental deduced reflection coefficients (Britton et al, 1989; Brandes, 1991) can be interpreted more realistically when the stronger reflection effects are accounted. The key here is the fate of the reflected positrons. It is the implicit assumption in the modelling of Britton et al (1989) and Brandes (1991) that the reflected positrons will no longer contribute to the positron surface processes. In reality, however, positrons reflected by the surface potential will be experiencing scatterings since they are still present in the solids. The average scattering angle of a thermal positron should be around 120° (Nieminen and Oliva, 1980), thus quite a fraction of the positrons will approach the surface again before they wandered further from the surfaces and annihilate in the bulk solid. Once at the surface region, positrons can participate in one of the surface escape processes, i.e., emission as positrons and Ps and trapping into the surface state.

In the experiments of Britton et al (1989) and Brandes (1991), it is not the outcome of a single encounter of the positrons at the surface that is measured. The measured reemitted positron fraction, e.g., is the sum of the many meetings between the positron and the surface potential. This reemitted fraction will not be sensitive toward the strong reflection positrons feel during one attempt. One can simply model the multiple encounter of a positron with the surface potential as follows. Assume that at a single encounter, positron reflection coefficient is r and the transmission coefficient is $t = 1 - r$, for these reflected positrons, a fraction $\alpha(\leq 1)$ on average will come back to the surface and join the surface processes again. After many such repeats, the total surface transmitted fraction is

$$\tau = t + \alpha r t + \alpha^2 r^2 t + \alpha^3 r^3 t + \cdots = \frac{t}{1 - \alpha r}. \tag{4.3}$$

From eq.(4.3), if all the reflected positrons are lost in the solid ($\alpha = 0$), then the measured transmission coefficient will be the same as that for a single encounter. When α is nonzero, there will then be a finite number of positrons coming back to the surface participating in the surface processes. In this case, the transmission coefficient obtained from eq.(4.3) τ will be larger than that for a single encounter t. The extreme case would be for $\alpha = 1$, when positrons will all be transmitted, i.e., a total absorbing boundary.

If τ is assumed to equal to $0.1 - 0.9$ which is of the same magnitude as deduced from eq.(4.1), and if t equals 1%, we can deduce from eq.(4.3) that $\alpha \approx 91\% - 99.9\%$. In other words, there are about $0.1 - 9\%$ of positrons "lost" in the bulk solids after one reflection by the surface potentials. Since experiments by Britton et al (1989) and Brandes (1991) are carried for relatively clean and defect-free sample, it is natural to assume that the "lost" positrons are due to annihilation events. The total bulk annihilation fractions of the reflected positrons corresponding to $\tau = 0.1 - 0.9$ are between 0.9 and 0.1 (this is actually the measured reflection coefficient in the previous experiments). Several percent of which (Jensen and Weiss, 1989) will be associated with the core electron annihilations. Noting that the trapping branching ratio is of the same order of magnitude as τ, the contribution of the reflected positron towards PAES will be due to those annihilating while within the Auger electron escape depths ($\sim$ 10Å). It can be estimated considering that thermal positron random walk diffusion length before they annihilate is about 10^3Å, thus 10^{-2} bulk positrons core annihilations may produce Auger electrons when compared with the surface trapped positrons.

There has actually been some experimental evidence for a large reflection of positrons at the surface. Köymen et al (1988) suggested from a simple classical model that their experimental results indicate an reflection coefficient of 95% for positrons reaching the surfaces; thus, positrons may encounter the surface potential many times through which they join the surface processes. Another example which may directly indicate the multiple encounter process is the positron microscope measurements of positron diffusion and emission in solids. By combining a classical diffusion equation with a non-total absorbing boundary, the positron reemission yield (Brandes, 1991) and the spatial profile widths (Brandes et al, 1991) of reemitted positrons have been analyzed. The positron emission yield measurement gives an reflection coefficient consistent with eq.(4.1) as discussed above, the experimental measured spatial profile widths, however, are larger than the calculated results from the diffusion equations. Among other possibilities, a larger reflection coefficient (Brandes et al (1991) suggested $R \geq 0.92$) can explain the discrepancy. We point out that it will be the reflection at a single encounter that is important for introducing widened spatial profile of positron emission; while the net result of multiple reflection is important for the positron emission yield measurements. Thus, it is realistic to explain the above findings with the multiple-encounter model proposed here. We note also that analyzing the experimental results with the diffusion equation approach may not be appropriate for evaluating quantum mechanical properties such as reflection, but the qualitative features should at least hold for the experiments.

A further example where surface reflection should be accounted for is the positron annihilation induced Auger electrons from solid surfaces. Positron annihilation induced Auger electron spectroscopy (PAES) has recently been developed as an unique probe for solid surfaces (Weiss, 1991). It is believed that positrons

originating the core holes for the subsequent Auger deexcitations are those which are trapped in the surface image-potential. The experimental support for this claim may be divided into two parts. On the one hand, temperature-dependent PAES signals are found to be complementary to that of thermal Ps desorption from surfaces, which are both attributed to surface trapped positrons (Mayer et al, 1990; Soininen et al, 1991). On the other hand, surface adsorption effects on PAES has been measured simultaneously with the electron collision induced Auger electron spectroscopy (EAES). The observed differences in PAES and EAES responses were explained by assuming that positrons producing the PAES signal are trapped at the surface potential (Jensen and Weiss, 1990). These experiments, however, do not exclude the possibility that a small percent of the PAES signal is due to bulk delocalized positrons.

Recently, Soininen et al (1991) measured the temperature dependence of PAES signal from a Ge(100) surface with relatively high accuracy. While they observed an essential desorption of the surface positrons through the Ps signal, the PAES signal was, nevertheless, nonzero and was about 5% of the room temperature intensity at elevated temperatures. The authors introduced other positron surface trapping centers to explain the nonzero PAES signal. We suggest that positron surface reflection can also explain the non-vanishing PAES signal. Positron workfunction at a Ge(111) surface was calculated to be +1.98 eV (Boev et al, 1987)); it is possible that the Ge(100) surface also has a positive workfunction (Jorch, 1981). While the thermal positron reemission channel is blocked in this case, Ps emission and positron surface trapping are still possible; thus, the effective reflection probability is not unity, though it is much enhanced compared with a negative workfunction surface. We note that the trapping branching ratio is of the same order of magnitude as the net reflection, τ, and the contribution of the reflected positrons to PAES will

be due to those which annihilate while within the Auger electron escape depths ($\sim$ 10Å). Considering that thermal positron random walk diffusion length before they annihilate is about 10^3Å, we can roughly estimate that 10^{-2} sub-surface positron core annihilations may produce Auger electrons when compared with the surface trapped positrons. Here, it is not necessary to introduce the multiple-encounter picture to account for the sub-surface PAES contribution, but multiple-encounter will certainly enhance the probability of such a contribution. The above estimate agrees in order of magnitude with the results of Soininen et al (1991).

In conclusion, we have suggested that positron reflection from the surface potential is more substantial than that suggested by Nieminen and Oliva (1981). Positrons will thus encounter the surfaces with many attempts to participate in the surface processes. For a clean, defect-free sample, a few percent of the reflected positrons will annihilate in solids after each encounter. The suggested picture is possible to explain the difficulties in previous positron measurements. The experimental data can also be interpreted more physically taking into account the fate of the reflected positrons.

§ 4.2 Positron Trapping into the Surface Image-potentials

Recently, a strong temperature dependence for positron trapping into the Ag(111) surface (Kong et al, 1991) is deduced (fig.4.1). At low temperatures, the trapping cross section of positrons is much enhanced (note that the measured surface trapping property is the branching ratio, the actual trapped positron fraction can be approaching zero as $T \rightarrow 0$ K because of the surface reflection. Approximately, the branching ratio of the surface trapping can be obtained by dividing the surface trapped fraction with the fraction of positrons transmitting through the surface potential). The anomalous temperature dependent positron trapping behaviors in fig.4.1 indicate that phonon emission may be important in mediating

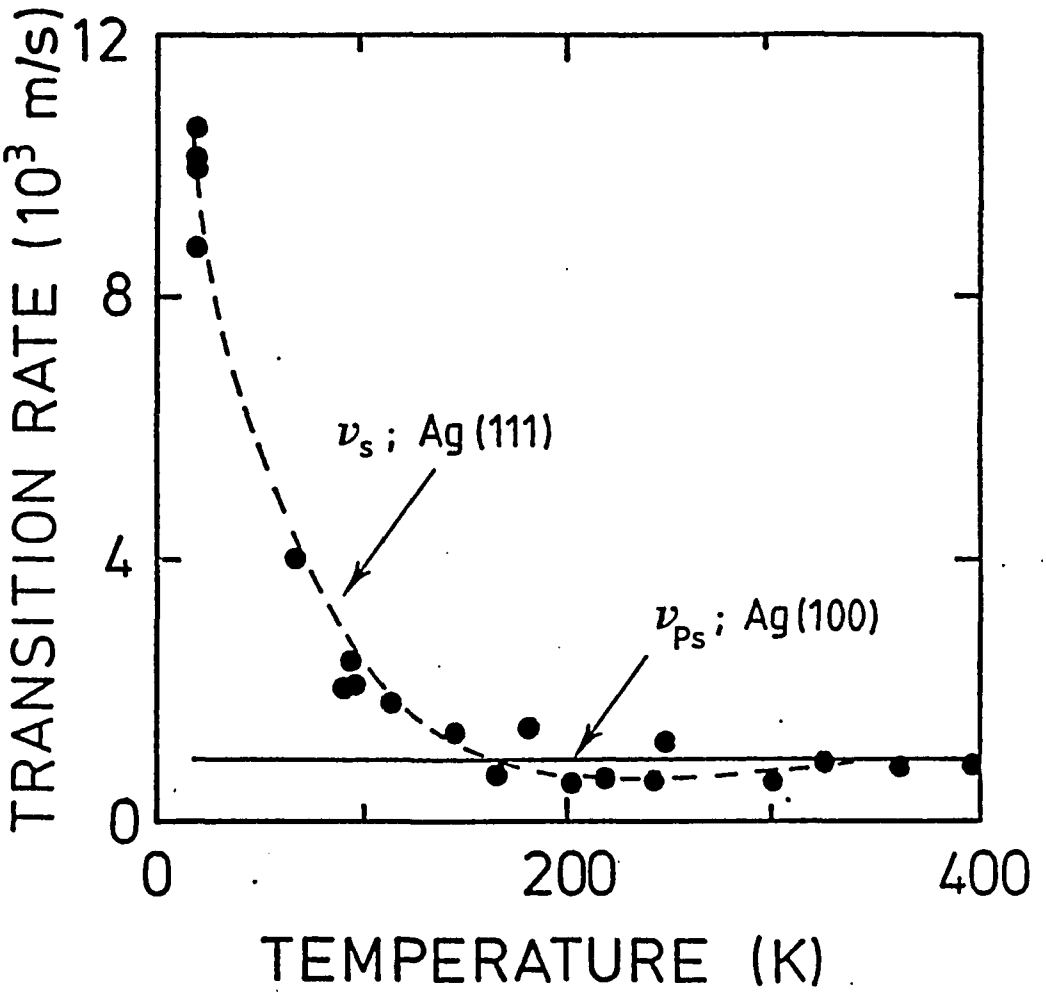

Fig.4.1 The deduced temperature-dependence of the positron surface trapping branching ratio at Ag(111) surface.

the positron trapping. Lax (1960) proposed a phonon cascade mechanism to explain the large electron capture cross sections in semiconductors. Dannefaer et al (1980) and recently Sarrinen et al (1989) applied the same phonon cascade model when interpreting the positron lifetime measurements in defected semiconductors. Negatively charged defects may exist in these semiconductors forming attractive Coulomb centers, thus excited Rydberg-like positron states are introduced. Positrons can trap into these Rydberg states by emitting phonons at low temperatures (Puska et al, 1990). In case of surfaces, the image potential is long-ranged Coulomb potential where excited Rydberg states can also exist. For negative workfunction surfaces, however, the energy differences between the positron energy level inside the solids and those Rydberg states can still be so large that one-phonon emission is impossible. For positive workfunction surfaces such as Ag(111), the energy difference can be within the Debye energy for the one-phonon process to be efficient. If the one-phonon trapping cross section for positron transition into the shallow levels can exceed that of the electron-hole mediated trapping at low temperatures, the net result may then be that the overall trapping rate is strongly enhanced at low temperatures.

In case of electrons at surfaces, the existence and properties of the image states have been studied extensively (e.g., Echennique and Pendry, 1978; Weinert et al, 1985). We shall be solving the wavefunctions and binding energies of the Rydberg-like states as Weinert et al (1985). Fermi golden rule is then employed to evaluate the positron trapping rate. In our approach, only qualitative features of surface trapping will be discussed without taking into account the dynamic or non-local effects of positron-surface interactions. The modelling of the surface potential is also simplified in many aspects, e.g., surface properties such as the effective Debye temperature, the Thomas-Fermi screening constant may all vary from bulk val-

ues which are simply parameterized. These approximations should not affect our conclusions here. Also, the experimental results in fig.4.1 should be viewed as qualitative only since it is subject to the indirect data analysis methods. The aim of the present work is to examine whether phonon cross section can be more important than electron-hole processes at low temperatures.

4.2.1 Positron Rydberg-like states at surfaces

Fig.4.2 shows schematically the positron surface potential used for the present calculation. This potential is modelled at the crystal side by a step-like potential, and at the vacuum side by an image potential $-1/4(z-z_0)$ with z_0 as the image-plane position. The intermediate connecting region is a plateau.

Schördinger equation can then be solved for the Rydberg-like state wavefunction with binding energy E_b

$$\Psi = \begin{cases} \exp[\sqrt{2m(E_b+\phi_+)/\hbar}], & z<0; \\ \cos kz + \sqrt{(\phi_+ + E_b)/(V_0 - E_b)}\sin kz, & 0<z<z_1; \\ \mathrm{W}_{\kappa,1/2}((z-z_0)/2\kappa), & z>z_1, \end{cases} \quad (4.4)$$

where $k=\sqrt{2m(V_0-E_b)/\hbar^2}$, $\kappa=\hbar/\sqrt{32mE_b}$, $V_0=1/4(z_1-z_0)$, and $W_{\kappa,1/2}(x)$ is the Whittaker function.

Matching the logarithmic derivatives $L=d\ln u/dz$ of eq.(4.4) at $z=z_1$ (L_1) and $z=0$ (L_0), we obtain

$$\tan(kz_1) = k\frac{L_0-L_1}{k^2+L_0L_1}. \quad (4.5)$$

A multi-branched relation between the image-plane position z_0 and E_b can be evaluated from eq.(4.5). The Whittaker functions for the lowest three states are

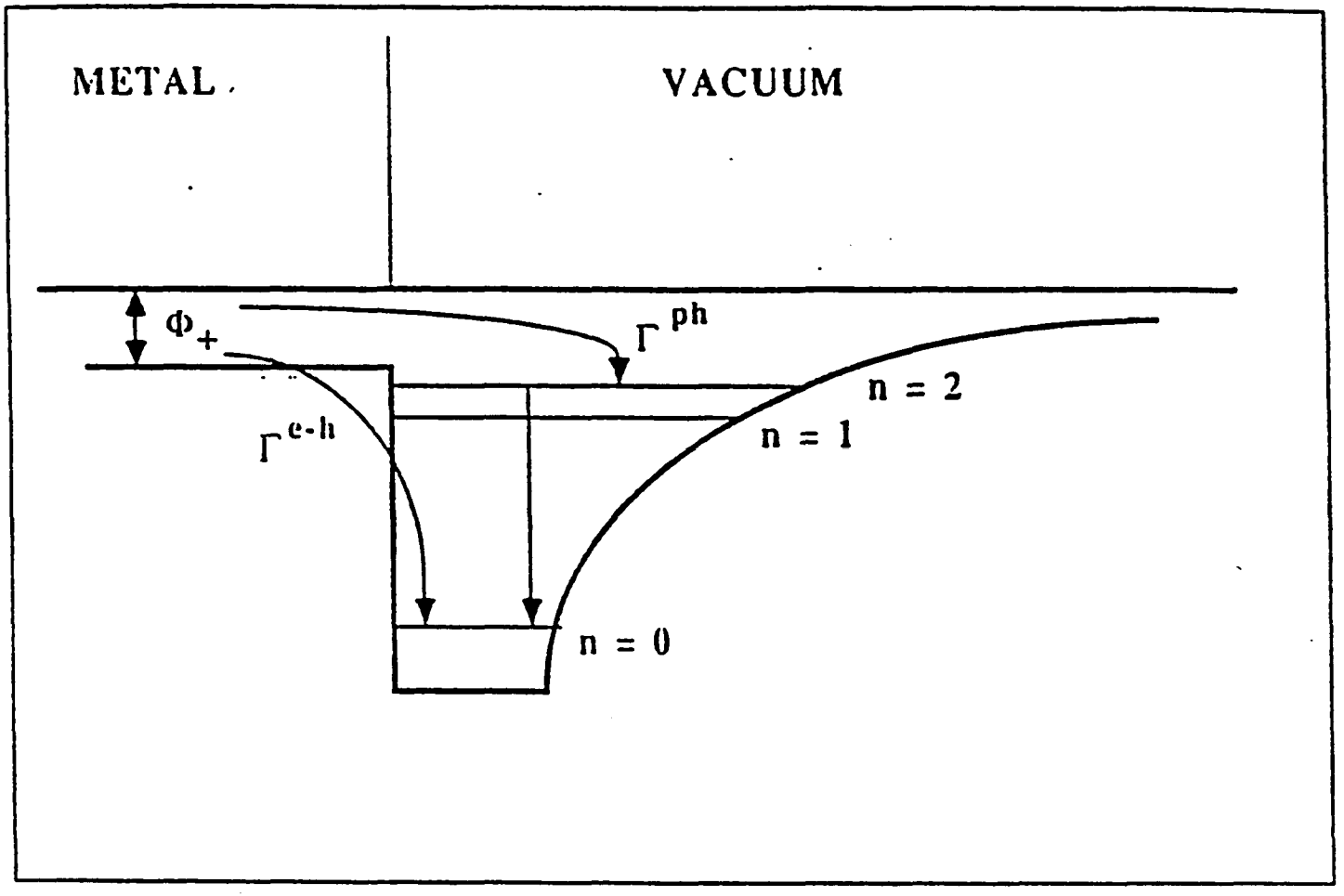

Fig.4.2 The schematics of the surface potential for calculating the positron surface trapping.

approximated by

$$W_{\alpha,1/2} = \exp(-x/2)\{1-\alpha[(\exp(-x)-1)\ln(x)-...]+...\}, n=0,$$
$$W_{\alpha+1,1/2} = x\exp(-x/2)\{1-\alpha[\ln(x)/x...]+...\}, n=1, \quad (4.6)$$
$$W_{\alpha+2,1/2} = x\exp(-x/2)\{(x-2)-\alpha[3+(2-x)\ln(x)-1/x]+...\}, n=2,$$

where $x=(z-z_0)/2\kappa$. The delocalized positron wavefunction is obtained from solving the Schrödinger equation numerically for the potential shown in fig.4.1. With the obtained wavefunctions, the transition matrix element for positron trapping can then be evaluated in the following sections.

4.2.2 Trapping through the electron-hole and phonon processes

The starting point for a calculation of the trapping rate Γ is the Golden rule expression first used by Hodges (1970). Bergersen and Pajanne (1974) pointed out that the Golden rule approach is more appropriate than other adopted approaches in terms of taking into account the quantum mechanics of positron trapping.

Generally, the trapping rate is

$$\Gamma = \frac{2\pi}{\hbar}\sum_{if}|M_{if}|^2 f_{\mathbf{k}}(1-f_{\mathbf{k}+\mathbf{q}})\delta(E_i-E_f), \quad (4.7)$$

where i,f indicate the initial and final states, $\mathbf{p}$, $\mathbf{k}$, $\mathbf{q}$ denotes the initial positron and electron momenta and the momentum liberated due to the positron localization, M_{if} is the transition matrix, E_i, E_f are the initial and final state energies, and $f_{\mathbf{k}}$ is the Fermi-Dirac distribution which is approximately taken as the zero temperature step function (Puska and Manninen, 1986).

The electron-hole assisted trapping transition matrix is

$$M_{if}^{eh} = V(q)\langle\psi_t|\mathbf{p}-\mathbf{q}\rangle, \quad (4.8)$$

where $V(q) = 4\pi/(q^2 + q_{TF}^2)$ is the Thomas-Fermi screened Coulomb interaction with a screening constant q_{TF}, ψ_t describes the final state wavefunction.

If the normalization length is L, then the wavefunctions of the positron-electron system before and after the trapping are

$$\Psi_i(\mathbf{r},\mathbf{r}') = u_i(z)\frac{1}{L}\exp(i\mathbf{p}_t\cdot\mathbf{r}_t)\frac{1}{L^{3/2}}\exp(ik_z z')\exp(i\mathbf{k}_t\cdot\mathbf{r}'_t), \tag{4.9}$$

$$\Psi_f(\mathbf{r},\mathbf{r}') = u_f(z)\frac{1}{L}\exp(i(\mathbf{p}_t-\mathbf{q}_t)\cdot\mathbf{r}_t)\frac{1}{L^{3/2}}\exp(i(k_z+q_z)z')\exp(i(\mathbf{k}_t+\mathbf{q}_t)\cdot\mathbf{r}'_t), \tag{4.10}$$

where z denotes the longitudinal component, $u_i(z)$ is the initial delocalized z-component positron wavefunction, and $u_f(z)$ is the final localized z-component positron wavefunction given by eq.(4.6). The primed coordinates are for electrons and the unprimed coordinates for positrons, the subscript t denotes the transverse component which are represented by plane waves for both electrons and positrons in the initial and final states.

The transition matrix term in eq.(4.7) can be evaluated as

$$\int d\Omega_q |M_{if}^{eh}|^2 = |\frac{V(q)}{L^3}|^2\frac{4\pi}{q}\int dz\int dz' u_i(z)u_f(z)u_i(z')u_f(z')\frac{\sin(z-z')q}{(z-z')}. \tag{4.11}$$

The sum over $\mathbf{k}$ in eq.(4.7) is evaluated by Puska and Manninen (1986) as

$$\sum_{\mathbf{k}} f_{\mathbf{k}}(1-f_{\mathbf{k}+\mathbf{q}})\delta(E_i-E_f) = \frac{L^3}{(2\pi)^3}mk_F\chi(\frac{q}{k_F},\frac{p^2/2+m(E_B-\phi_+)}{\hbar^2k_F^2}), \tag{4.12}$$

where

$$\chi(x,y)=\begin{cases} \pi[1-(y/x-x/2)^2]/x, & x+x^2/2 \geq y \geq |x-x^2/2|; \\ 2\pi y/x, & 0 \leq y \leq x-x^2/2; \text{ and } x<2, \\ 0, & \text{otherwise.} \end{cases}$$

Eq.(4.7) can thus be evaluated for the electron-hole assisted positron trapping into the surface state.

The positron-phonon interaction matrix element has been evaluated by Perkins and Carbotte (1970).

$$M_{if}^{ph} = \{\frac{E_d^2 q[n_q(T)+1]}{2\rho c_s L^3}\}^{1/2} q_{TF}^2 M_{if}^{eh}, \tag{4.13}$$

where E_d is the deformation potential constant, ρ is the density of the material and c_s is the sound velocity, $n_q(T)$ is the Bose-Einstein distribution for phonons. It should be remarked here that q_{TF} at metal surfaces will be smaller than the bulk screening constant (Neilson et al, 1986). Combination of eq.(4.13) and (4.7) gives the phonon-assisted trapping rate.

4.2.3 Results and discussions

The parameters for the present calculation is shown in table 4.1. Positron workfunctions are 0, and ±0.075 eV respectively for zero and positive and negative workfunction surfaces. The binding energies are calculated, e.g., for positive workfunction surface as 1.9 eV, 0.8 eV and 0.08 eV for $n = 0, 1, 2$ states. Fig.4.3a shows the electron-hole assisted positron trapping rate when the positron workfunction is +0.075 eV. It is seen that for electron-hole mediated trapping, there exists only a weak temperature dependence. This is due to 1) the phase space available for electron-hole excitation; and 2) the delocalized positron overlapping with the localized state all have very small temperature dependences. The electron-hole assisted trapping into the n=2 state in fig.4.3a is not as efficient as trapping into the deeper states (n = 0, or 1) due to the phase space limitations. The temperature depen-

dence increases, however, for trapping into the $n = 2$ state. This can be explained by the fact that the spatial extent of the corresponding surface state is larger thus the overlapping of the localized state with the delocalized state is more temperature dependent.

Table 4.1

Parameters for surface trapping calculation

Surface potential well depth: 4.10 eV
Image plane position z_0: 1.5 Å
Fermi momentum: 0.76 $Å^{-1}$
Sound velocity: 3650 m/s
Deformation potential: 9.5 eV
Debye temperature: 225 K

The electron-hole assisted trapping rates into the n=2 state of the three work-function surfaces are shown in fig.4.3b. The trapping is more efficient as the work-function changes from positive to negative due again to the phase-space limitations of exciting electron-hole pairs. The temperature dependences are similar for these three cases indicating that there is little temperature difference in the spatial extent of the wavefunctions.

For one-phonon assisted trapping, only positron energy librations smaller than $k_B\Theta_D$ (Nieminen, 1983) but larger than k_BT (Lax, 1960) will have appreciable contributions. In the present case, trapping into the n=2 state of the positive workfunction surface satisfies the condition. Fig.4.4 shows the evaluated trapping rate at varying temperatures for phonon assisted trapping into $n = 2$ state. It is seen that the phonon assisted trapping processes can have a larger trapping rate than even the electron-hole trapping rate into the $n = 0$ ground state. Thus there

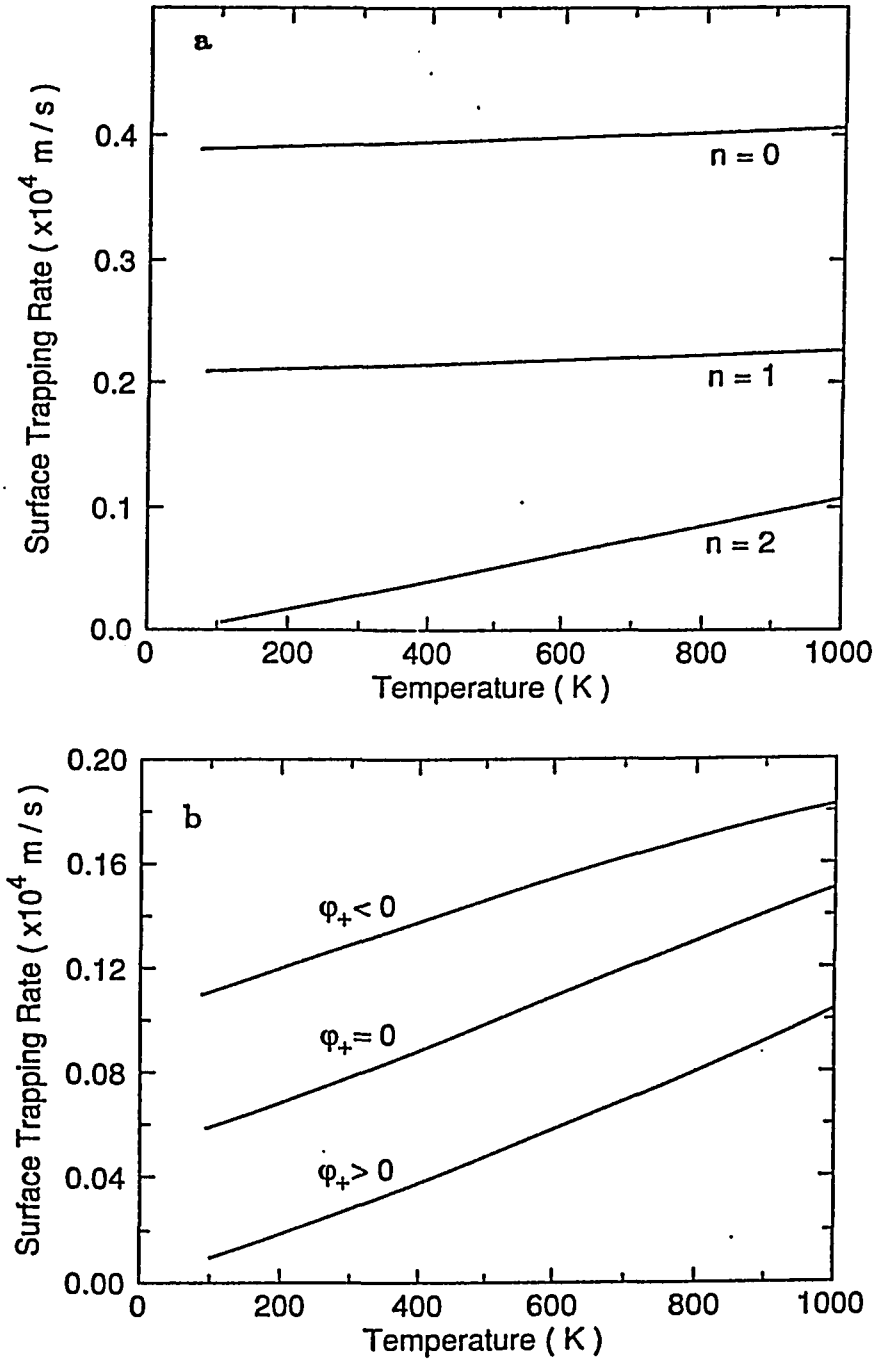

Fig.4.3 a) Temperature-dependence of the electron-hole trapping rate into the n=0,1,2 states of the positive positron workfunction surface. b) Temperature-dependence of the electron-hole trapping rate into the n=2 state for different positron workfunctions.

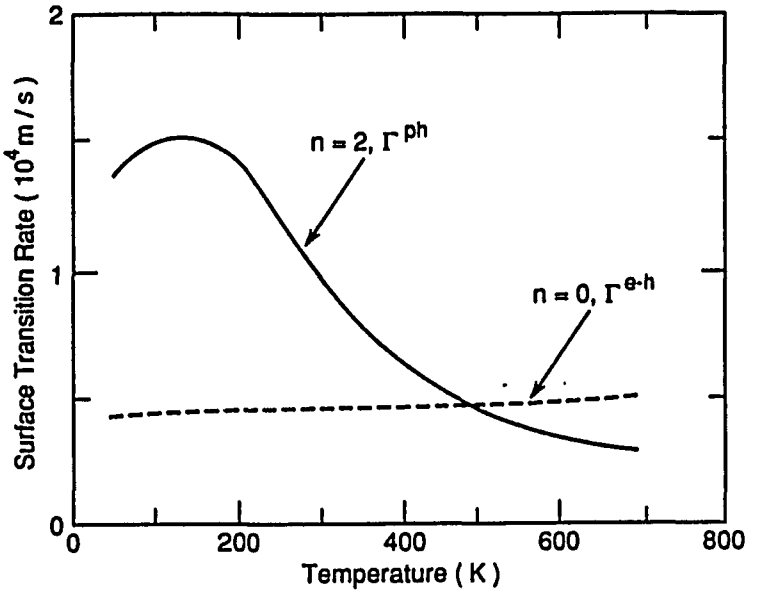

Fig.4.4 Temperature-dependence of the phonon mediated trapping rate into the n=2 state, the e-h trapping rate into n=0 is also shown.

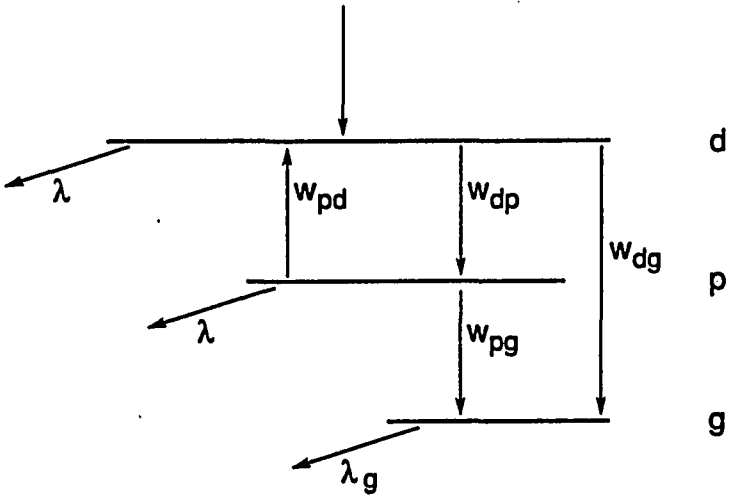

Fig.4.5 Schematics of a two-stage trapping model (see text for explanations).

can indeed be an enhancement of positron trappings at low temperatures. Strong temperature dependence is also seen in fig.4.4. By examining the matrix element in eq.(4.13), it is found that the Coulomb interaction term decreases as the momentum transferred increases at elevated temperatures. However, not too much faith should be given to this fall-off region of the phonon cross section since it corresponds to larger momentum transfers where the validty of eq.(4.13) needs to be investigated.

The positron trapping behavior into the Rydberg states will also have to take into account the possible positron detrapping at elevated temperatures. Based on equilibrium kinetic equations, the effective positron trapping rate can be evaluated with a two-stage trapping model schematically shown in fig.4.5. The possible positron states are represented by horizontal lines, and vertical arrows indicate the transitions in between the states. The population for the delocalized state (d-state), the precursor state (p-state) and the ground state (g-state) are n_d, n_p, n_g, and the annihilation rate for positrons in the d and p state are assumed to be the same as denoted by λ and the annihilation rate in the g state is λ_g. Denote the positron transition rates between the d and p, d and g , p and g state as w_{dp}, w_{dg}, w_{pg}, and further the detrapping rate from the p state is w_{pd}. A steady state solution yields the branch of positrons annihilated while in the ground surface state (Puska et al, 1990) as

$$\frac{w_{dg}(\lambda + w_{pd} + w_{pg}) + w_{dp}(w_{pg} + \lambda)}{(\lambda + w_{dp} + w_{dg})(\lambda + w_{pg}) + w_{pd}(\lambda + w_{dg}).} \tag{4.14}$$

From which an effective trapping rate into the ground state is

$$\kappa_{eff} = w_{dg} + \frac{w_{dp}(w_{pg} + \lambda)}{w_{pg} + w_{pd} + \lambda} \approx w_{dg} + \frac{w_{dp} w_{pg}}{w_{pg} + w_{pd}}. \tag{4.15}$$

The last approximation is because of the much smaller λ value as compared

with the much larger trapping rates.

In thermodynamic equilibrium, positrons in the surface potential well can be assumed as a two dimensional gas whose chemical potential equals that of a three dimensional positron gas in the bulk solid. The free energy distribution of the positrons gives the relation of the trapping and detrapping rates as

$$\frac{w_{pd}}{w_{dp}} = \frac{1}{\rho_L}\sqrt{\frac{mk_BT}{2\pi\hbar^2}}\frac{\exp(-E_b/k_BT)}{1-\exp(-E_b/k_BT)}, \tag{4.16}$$

where ρ_L is the surface-to-volume ratio for planar traps. Combination of eq.(4.15) and eq.(4.16) gives rise to a temperature desorption behavior which will effectively suppress the phonon trapping at high temperatures. From this point of view, phonon contribution can be neglected at high temperatures. The trapping at elevated temperatures is due to w_{dg}, i.e., the direct trapping from the delocalized state into the ground surface state without the precursor state playing a role.

§ 4.3 PAES Study of KCl(100) Surface

In this section, we shall present our study of positron interaction with KCl(100) surface using positron annihilation-induced Auger electron spectroscopy. In case of metals and semiconductors, PAES has been shown to be mostly originated from positrons trapped at the image-potential (Weiss, 1991), where they may annihilate with core electrons of the surface atoms. The subsequent core hole deexcitation emits Auger electrons mostly from the topmost surface layer atoms. There is, however, no study of insulating materials with PAES so far. Therefore, the present study is concerned with an ionic solid. It would be interesting to observe on an insulating surface whether positrons trap at a surface image potential; if the PAES is totally due to the surface trapped positrons; and also the possible energy release

mechanisms for positron trapping into an insulator surface.

We have carried the positron incident-energy dependent study, as well as the temperature dependent study with PAES. The relevant experimental aspects are discussed in subsection 4.3.1. The experimental results are given in subsection 4.3.2 and 4.3.3. Discussions and conclusions are presented in 4.3.4.

4.3.1 The experimental aspects

The KCl sample is cleaved in air with a thickness of 3mm and (100) orientation. It is cleaned *in situ* by low energy ion sputtering and heating over more than 20 hours at 450°C. After this process, the PAES spectrum is seen to be stable with time during the data acquisition. This shows that positron beam will not induce any observable damages to the insulating sample (see section 4.4).

In the PAES positron beam (fig.2.1), the incident positron energy is determined by the extraction voltage and the sample biasing. It is the sample bias that is varied during the experiment to change the positron energy with respect to the sample. Sample charging is determined by monitoring the secondary electron spectrum produced by $\sim$ 200 eV positrons. The secondary electron spectrum will be shifting with time when the sample charges up. For the present sample geometry, the charging is found to be negligible during PAES measurement if the sample temperature is above 150°C. Another aspect of this experiment is that it will take typically 200 seconds of data acquisition time for one PAES spectrum in order to obtain sufficient statistics. A positron energy or temperature scan may then need several hours to complete in a vacuum of high 10^{-9} torr. Surface contamination effects will thus be possible, though the relatively high temperatures at which the measurements are carried reduces the problem to some extent. To assess the effects of surface contamination, positron energy is swept up and down during the positron energy dependent runs. The possible surface contamination during temperature-dependent

runs will also be mentioned in section 4.3.3.

In section 2.1, the limitations on the energy resolution of the present positron beam system are discussed. Since only Cl Auger signal is observed for a clean KCl sample, the beam can thus be tuned into the optimum settings for monitoring the Cl (LMM) 181 eV Auger electrons. Another thing to note is that with the permanent magnet, the peak position of the Cl 181 eV Auger electrons will be shifted down to $\sim$ 172 eV before they are detected (Lei, 1988). This shifted peak is still within the pass energy window of [150 eV , 210 eV], though some of the signal may be cutoff by the low pass energy due to the poor energy resolution.

4.3.2 Positron incident energy dependent measurements

Fig.4.6 shows the positron energy dependent measurements up to 30 eV for (a) total annihilation γ ray counts; (b) the R-parameter indicative of o-Ps fraction; and (c) the Cl(LMM) 181 eV PAES counts. Correlated energy-dependent oscillation features are seen in these measured quantities. It should be first of all remarked that the exciton production (with threshold energy E_g) is competing with Ps formation in the energy region $E_x + E_+ < E < E_g + E_+$ (here E_g is the energy gap, E_+ is the positron zero-point energy in the solid), but the width of which ($E_g - E_x \sim 0.6$ eV, Tuomissari et al, 1989) is much too small to be resolved with the present setup, thus it is not mentioned in the following discussions of the energy-dependent features.

For the R-value in fig.4.6b, the first oscillation around zero energy is an artifact. Since at very low incident energies, positrons are partly retarded from reaching the sample and will annihilate elsewhere. The γ-rays from these annhilations are reaching the NaI detector in a different solid angle from it would otherwise be if the positrons are annihilating in or near the sample. The scattering of the γ-rays in the chamber and the shielding materials before they are detected by the NaI will effectively suppress the 511 keV photopeak, thus the relative T/P value will be

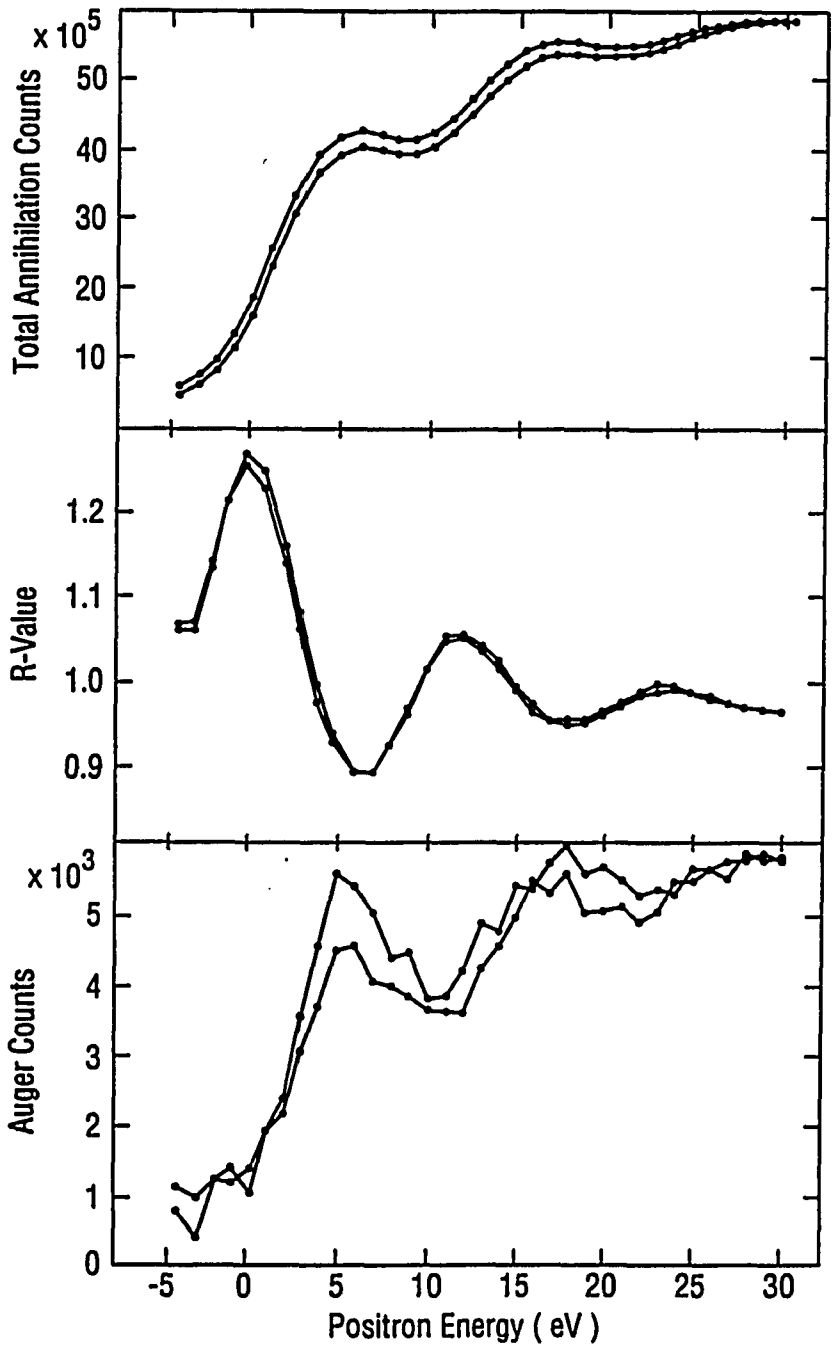

Fig.4.6 The positron incident energy dependent measurements of a) the total annihilation counts; b) R-value for o-Ps production; and c) the PAES counts from KCl(100) surface.

increased giving rise to the first oscillation feature.

Beyond that point, however, the oscillations can be attributed to energy-dependent Ps formation in KCl. Similar oscillations in Ps fraction as a function of positron incident energies have been observed for several other insulators (Eldrup et al, 1985; Chen et al, 1988). Ore mechanism of Ps formation is employed for interpreting the results. Positrons will excite valence electrons forming Ps, thus the Ore gap corresponding to the valence band is

$$E_g + E_+ - E_B < E < E_g + E_+, \tag{4.17}$$

where E_B is the Ps binding energy in KCl. Positrons with energies falling within the Ore gap will form Ps efficiently. Once out of the Ore gap, other energy loss processes will suppress the effective formation of Ps, thus introducing the energy-dependent features shown in fig.4.6b. The dominance of the Ore mechanism for Ps formation in KCl is also evidenced in the measurement of reemitted Ps velocity distribution where the Ps energy is found to be significantly below the prediction of the spur model(Tuomissari et al, 1989).

Assume E_B = 3.2 eV, E_+ = −1.5 eV and E_g = 8.4 eV for KCl (Tuomissari et al ,1989), the first Ore gap for KCl is from eq.(4.17) [3.7 eV , 6.9 eV]. Gullikson and Mills (1986) measured KCl (the surface orientation is not clear) Ps production threshold and found it to be 4.7 eV which gives E_+ = − 0.5 eV for E_g = 8.4 eV, E_B = 3.2 eV. The Ps formation threshold in our case is not apparent from the R-value measurement in fig.4.6b, but it can be deduced from either the total annihilation counts or PAES measurement as $\sim$ 6 eV which is larger than the above values. Eldrup et al (1985) argued that Ps formation will have a higher threshold value than that given by eq.(4.17), they actually assumed a $\sim$ 4 eV higher threshold to interpret their observations. In our case, however, part of the reason for a

higher threshold value in fig.4.6 is because of the magnetic field gradient effects. The longitudinal energy of the positrons are reduced according to eq.(2.4) when they approach the surface. The effective positron longitudinal energy distribution at the target position will be spread from zero up to the nominal energy due to this magnetic field gradient. Positrons with large initial angular distributions can even be reflected. This "magnetic mirror" effect is most clearly seen in the total annihilation counts as a function of the positron nominal energy. Since the low energy positrons are angularly more disperse than the higher energy case, a large fraction of positrons are repelled from the sample at low incident energies (1-5 eV)

If we assume that the permanent magnet will produce a uniform longitudinal energy distribution for positrons reaching the target, a true energy dependent function $f(E)$ can be obtained from the measured distribution $f'(E)$ as follows.

$$f'(E) = \frac{1}{E}\int_0^E f(E')dE', \tag{4.18}$$

Differentiation of eq.(4.18) obtains

$$f(E) = f'(E) + E\frac{df'(E)}{dE} \tag{4.19}$$

There are two major effects after this transformation as shown in fig.4.7. One is that the threshold position will be shifted downward. It becomes $\sim$ 4 eV after the transformation in better agreement with that predicted by eq.(4.17) (3.7-4.7 eV). The first oscillation feature peaks at $\sim$ 7 eV or about 3 eV lower after the transformation. This is also more close to the predicted upper limit of the Ore gap of 6.9-7.9 eV. The second effect is that the oscillation features will be sharper after the transformation, the widths of the oscillation features will be reduced. This is because that eq.(4.18) indicates a degraded resolution function especially at higher

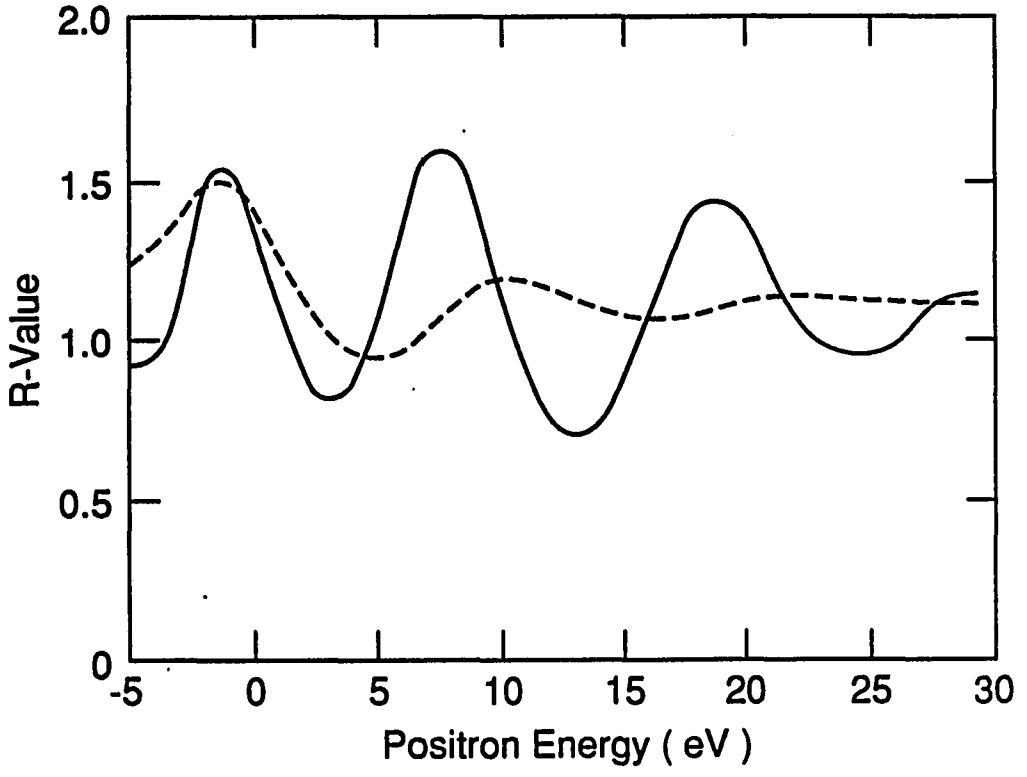

Fig.4.7 Transformation of the energy-dependent R-values with eq.(4.19).

energies.

The above discussion is a simplified one. The three dimensionality of the solid will actually introduce Ps production threshold values dependent on the positron incident directions. This point may explain the inconsistencies between the experimentally evaluated and theoretically predicated threshold values in many cases. The magnetic beam that is often used for such a measurement is disadvantageous since the angular distribution of positrons is not well defined.

As to the oscillation in the total annihilation counts in fig.4.6a, Eldrup et al have also observed similar features but only when the reemitted positrons are returned to annihilate in the target. They have attributed the oscillations in their total annihilation counts to the diffraction effects in a single crystal ice sample. The oscillations shown in fig.4.6a, however, are seen to be closely related to the Ps. It is thus difficult to suggest that such oscillations are also related to diffraction effects. If indeed the diffraction effect is dominating, the corresponding PAES and Ps fraction should both follow the total annihilation count behavior in the same trend. The fact that Ps fraction change is complementary to that of PAES and total annihilation counts discounts the diffraction possibility greatly. The wide angular and energy spread of the positrons in the present setup should minimize the possibility that diffraction features will be present in our measurement.

The reduction in the total annihilation counts when Ps forms in larger fractions can be both due to the positron reemissions and the escape of the o-Ps from the solids. In the present setup, the NaI detector is 90° with respect to the incoming beam and is well shielded on the sides, thus it will not be able to detect the annihilation of o-Ps escaped away from the solids. This is different from Eldrup et al's measurement(1985) where a Ge detector is behind the sample facing the incoming beam. The solid angle effect there is convoluted with the increased γ-ray counts

due to the dominant 3γ annihilations of o-Ps. Thus the total annihilation counts measured can be insensitive to o-Ps escape compared with the PAES setup. Another note is that the grid before the 1D-PSD in fig.2.1 is biased at +200 Volts, so reemitted positrons should be reflected back to the target chamber, making the measurements in fig.4.6a even more sensitive to o-Ps counts. Presently, we consider the reduction of total annihilation counts when Ps abounds to be mostly associated with the o-Ps escape.

It is interesting to note again that the initial slow increase of the total annihilation counts over an energy span of $\sim$ 5 eV is much wider than that measured by Eldrup et al (1985). This is both due to the energy resolution of the PAES beam, and the magnetic field gradient as mentioned in section 2.1.

PAES measurement of the Cl (LMM) 181 eV Auger electrons is shown in fig.4.6c. It follows the same trend as that of the total annihilation counts and complements the behavior of Ps fraction. This complementary behavior is explained as due to the competing nature of Ps formation and core hole production, since the population of bare positrons will be reduced when Ps forms efficiently. One point which needs special attention in fig.4.6c is that the threshold for producing PAES is at zero positron energy, the initial rise of PAES from 0-5 eV follows closely the changes in the total annihilation counts. The implication of this zero threshold energy will be discussed in section 4.3.4.

Lastly, we note that two runs are taken in fig.4.6. Positron energy is increased from -5 to 30 eV in the first run and decreased from 30 to -5 eV in the second run. The small difference in the two runs is attributed to possible surface contaminations, as well as the reduction in positron beam strength after 10 or more hours of run (Soininen et al, 1991). The difference in fig.4.6b is smaller than 4.6c. This is because Ps formation is a subsurface phenomenon here and is less sensitive to the surface

conditions.

4.3.3 Temperature-dependent measurements

Fig.4.8 shows the temperature dependent PAES measurement at positron incident energy 40 eV. The temperature is varied between 150°C - 450°C. Ps fraction has been found to be almost constant throughout the measured temperature region. This is not surprising since the energy gap $E_g \sim 8.4$ eV is 1.6 eV larger than the Ps vacuum binding energy, thus surface positron desorption through Ps channel is energetically unfavorable even if there does exist positron surface states. This desorption channel is further discounted when considering the possible larger binding energies of the positron state producing the PAES (see 4.3.4). In that case, even if electron surface state exists, the obtained desorption energy can still be too large to enable effective Ps desorption.

There is also the possibility of thermal effects for bulk produced Ps. Tuomissari et al (1989) have measured the TOF distribution of the reemitted Ps from a series of alkali halides including KCl. Only one source of Ps production is found in KCl which is attributed to Ore mechanism. Though the diffusion length of the Ps in KCl is comparable to the stopping depth of 40 eV positrons, the temperature dependence of Ps diffusion is, however, negligible (Schultz and Lynn, 1988).

The PAES measurements in fig.4.8, on the other hand, shows a desorption-like behavior as temperature is increased. The change in PAES intensity with temperature is found to be consistent for several samples over positron incident energy range of 40-100 eV. This temperature dependence can be attributed to positron transport and/or the trapping/detrapping processes at the surface. One special note about fig.4.8 is that the level-off at the high temperature region (> 450°C) still possesses substantial PAES signal ~ 40 % of that at ~ 150°C.

The data in fig.4.8 is taken with the sample heated in between the

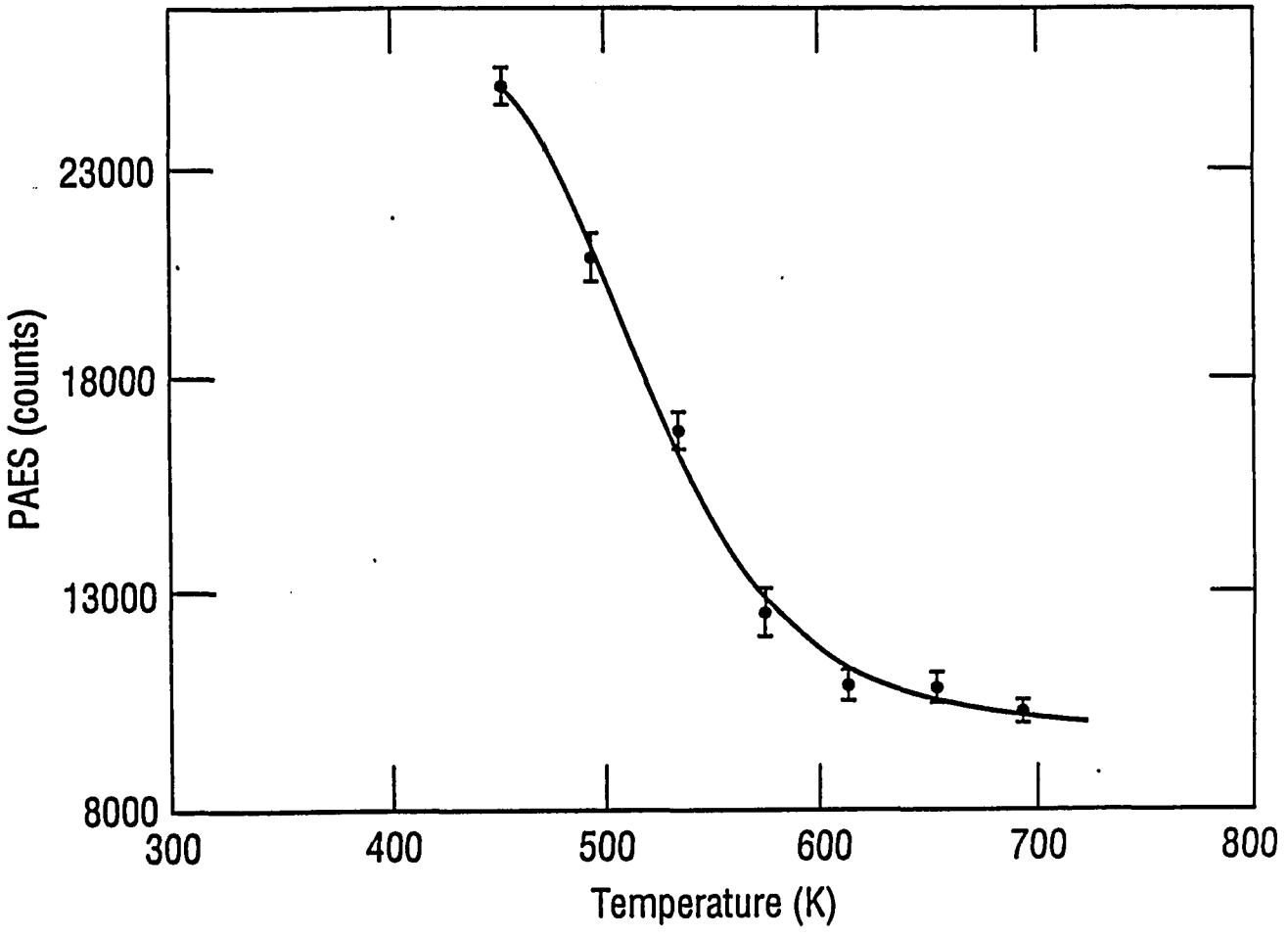

Fig.4.8 The temperature-dependent PAES intensity (solid dots) at positron incident energy 40 eV for KCl(100) surface. The solid line is fitting with a desorption model.

measurements, the observed temperature behavior is repeatable indicating contamination effects can be neglected. We have also noticed that the temperature dependence can be sensitive to the surface conditions. Fig.4.9 shows two temperature runs, with one of them going from one measurement temperature to another directly; while the other is heated to above 400°C after each measurement at the temperature of interest. The reduction of PAES signal at lower temperature region (< 400°C) for the measurements without intermediate heating is attributed to surface contaminations during the data acquisition.

4.3.4 Discussions and conclusions

In this subsection, we shall first of all discuss the possible positron states in KCl which may contribute to PAES measurement. The indications of the above mentioned measurements are then considered, especially in relation to the existence of surface states.

Apart from the possible surface image-potential trapped positrons. PAES can also be due to positrons in the bulk states. These bulk states include delocalized positrons, positrons bound to the Cl ions, pick-off annihilations of Ps with core electrons, and positrons trapped by defects, etc.

Theory calculation indicated that for bulk delocalized positrons, positron annihilation with anions is $\sim$ 8 times as more possible as with cation element in KCl (Puska, 1991). We have failed to see any detectable potassium Auger signals for a clean sample. It is only after sputtering the sample that we can detect some K (LMM) 240 eV Auger electrons, but its intensity is only about one-nineth of the Cl signal. The fact that we did not observe the potassium PAES signal is the first indication that we may be seeing the Auger electrons produced by positrons in a state other than the bulk delocalized one.

The KCl (100) surface is neutral consisting of both anion and cation ions. Its

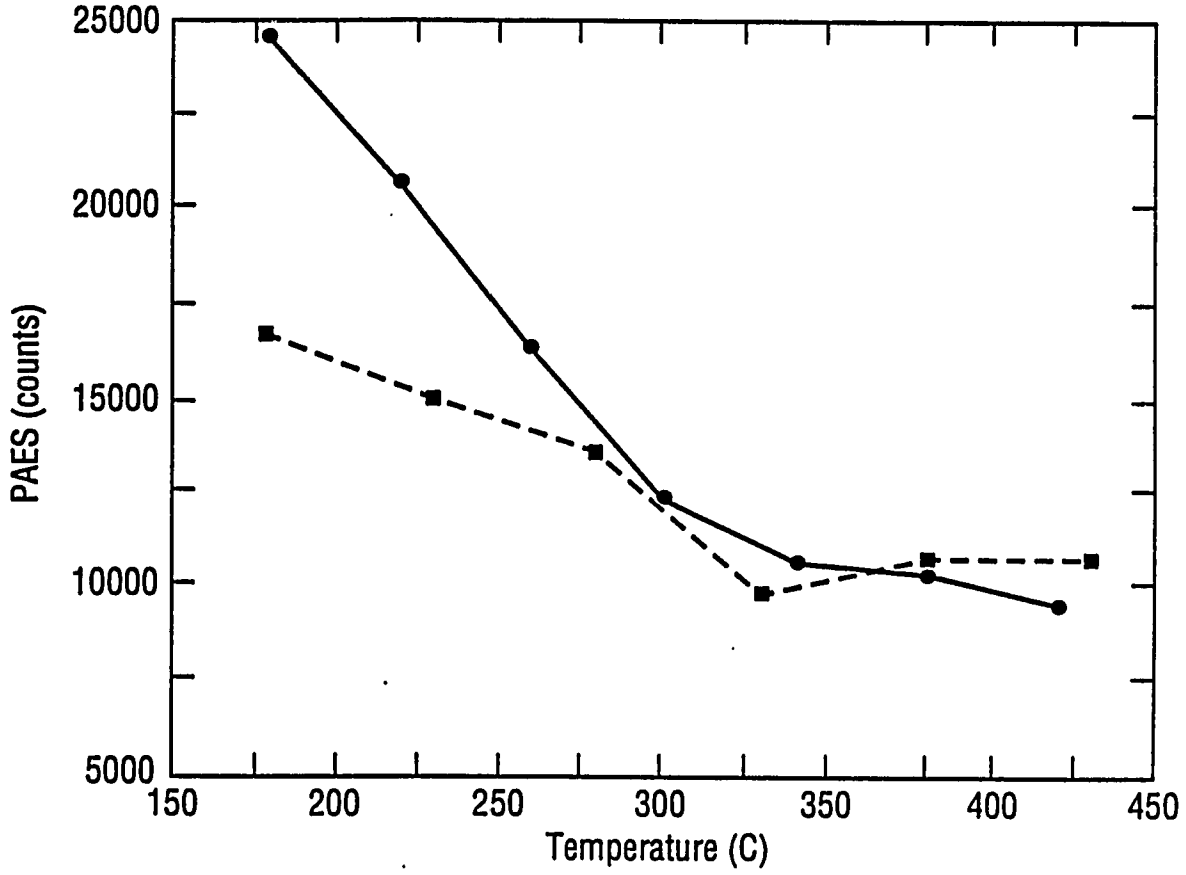

Fig.4.9 The temperature dependence of PAES with heating the sample to above 400 °C before each data point is taken (solid line); and without intermediate heating.

compound nature presents an interesting difference from the often studied elemental metal or semiconductor surfaces. While the positron surface interaction in the surface normal direction is governed by the image-potential, the two-dimensional potential parallel to the surface is corrugated due to the presence of cation and anion ions. The positron surface state, if it exist, can be strongly modulated by this corrugated potential.

When a one-dimensionally localized surface state is concerned, the image-potential is the most important possibility for positrons. This is unlike electrons where surface state may occur due to the termination of the three dimensional periodicity. In the solid side, positron energy level is

$$-\phi_+ = D + E_0 + E_{corr}, \tag{4.20}$$

where D is the surface dipole, E_0 is the positron bulk band energy, and E_{corr} is the positron-electron correlation energy. In the vacuum side, the classical image potential for a static particle on a dielectric surface is

$$V(z) = \frac{\epsilon - 1}{\epsilon + 1}\frac{e^2}{4z}, \tag{4.21}$$

where ϵ is the dielectric constant of KCl. Imposing a cutoff of eq.(4.21) at the vacuum side will give rise to a plateau region between the inner potential and the image potential. The above formulation of the surface potential is basically the Hodges-Stott model (1973) used in 4.2 for positron surface trapping calculations. Though dynamic and nonlocal calculations of the surface potential are developed later, this model remains to provide qualitative information for understanding the many experimental results. With the surface potential defined above, surface state and its associated binding energy E_b can be evaluated.

A stable surface state must fulfill the conditions that $E_b < \phi_+$ and $E_b < 0$. We have calculated the binding energy for a square potential well as a function of positron surface workfunctions. The depth of the potential well is 6.8 eV, the width is 1.5 Å. Fig.4.10 shows the difference of the positron zero point energy in solids and the binding energy of the surface state vs the surface state binding energy. It is seen that the more positive the positron workfunction is, the less bound the surface state will be, until the bound state becomes unstable at a certain point. The dotted line intersect the ϕ_+ axis at where the bound state begin to be non-existent $\sim$1.25 eV. The energy difference (vertical axis) shown in fig.4.10 is the minimum energy that can be liberated when a positron transits from a delocalized bulk state to the surface state. This is around 1-2 eV for positive workfunction surfaces. It is recognized that the KCl(100) surface possesses a positive workfunction for positrons (see, e.g., Tuomisarri, 1989), we may thus expect that positron trapping into the possible KCl(100) surface image-potential will liberate an energy 1-2 eV.

Surface trapped positrons will be sampling the anion and cation elements differently from delocalized positrons. Positron wavefunction can be modulated strongly by the two-dimensional surface potential. Thus the fact that no K Auger electrons are detected can be associated with the surface trapped positrons because of this two-dimensional character, as well as the possible (100) surface relaxation and rumpling. The later is calculated by Welton-Cook and Prutton (1977). For KCl, the relaxation is about -1.73 % of bulk lattices constant, and rumpling is about 4%.

Another important positron bulk state in KCl which may contribute to PAES is due to the ionic nature of the solid. The long range Coulomb interaction between the positron and the anion element (X^-) can produce a bound system composed of [X^-, e^+]. Nuramagambetov (1985) showed that the positron and halogen negative ion bound state has an energy band of width $\sim$ 3.07 eV (referred to as anion

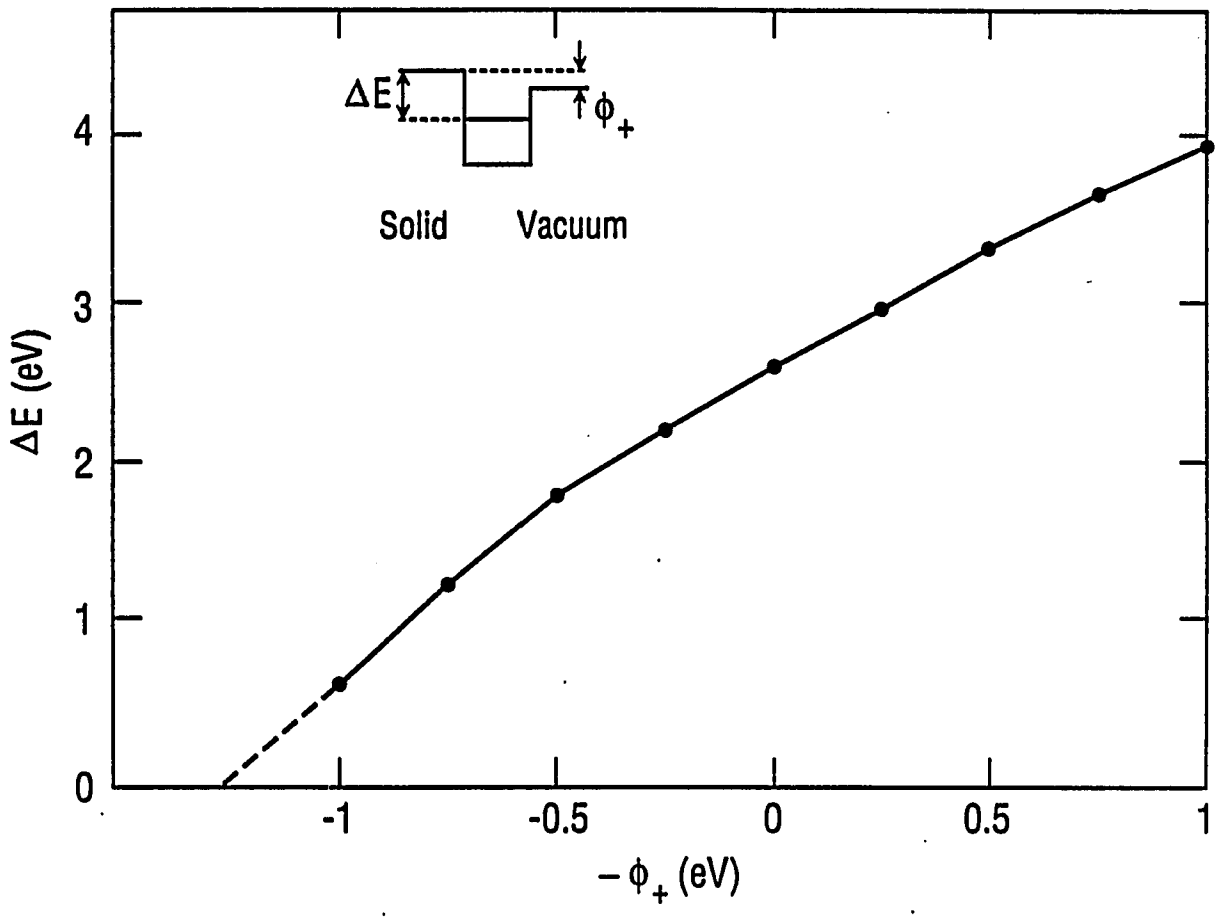

Fig.4.10 The model calculation of the energy difference between positrons in the solid and at the surface potential vs positron workfunction ϕ_+.

band hereafter). Positron motion in the anion band is deduced to be hopping dominated and the room temperature diffusion coefficient is 1.1×10^{-4} cm^2/sec (Nuramagambetov, 1985). Further, the binding energy of the anion-positron bound state is of $\sim$ 8 eV. This large binding energy will be important when explaining the energy-dependent features below.

The positron-anion band may actually be playing a role by the fact that we have failed to observe PAES on LiF, NaF. Though there is evidence of LEPD threshold effects on these surfaces (Horsky et al, 1989), there may not exist ground state bound positrons or there may not be efficient mechanisms for populating a ground positron surface state even if it exists. It happens that Nuramagambetov (1985) indicated that fluorides will have most of the positrons annihilate in Ps state instead of the anion band. This difference from that of KCl may be the possible reason that PAES is not observed on LiF and NaF samples. Our failure to observe K Auger electrons can also be easily explained if positrons producing PAES are bound to the Cl ions. In section 4.1, the bulk delocalized positron contribution to PAES is compared with the surface trapped positrons. The analysis there is valid for most metal and semiconductor surfaces since the equilibrium positron state in these solids is delocalized Bloch positrons. When positron equilibrium state becomes a bound state such as described here, bulk positron contribution to PAES can be much more enhanced.

As to the defect related positron state, since no time-dependence of the PAES is found, we may assume that any defects that will affect PAES should be in thermal equilibrium with the solids. The importance of thermal defects as the positron trapping centers producing PAES for a clean KCl sample can be neglected, however, considering the decreased PAES signal at elevated temperatures. Since more thermal defects should occur as temperature increases which is opposing to the data in

fig.4.7. Apart from the role as a direct trapping center producing PAES, the thermal vacancy generation in bulk solids may also affect the delocalized positron diffusion back to the surface. The diffusion length of the delocalized positrons should be large when compared with the small stopping depth of the 40 eV positrons because of less efficient scatterings in insulators. Thus the PAES temperature dependence is difficult to explain by the defect trapping of delocalized positrons.

From the above discussions, we may then discount the contributions from the delocalized positrons as well as the defect trapped positrons, only the surface trapped state and positrons bound with the anion ions need to be considered. The binding energy of the surface state positrons is of the order of 1 eV which is several times smaller than the positron binding energy in the anion band $\sim$ 8 eV. Thus by studying the energy dependent characteristics of PAES, we may distinguish the contributions from these possible positron states considering the positron trapping mechanisms. The following energy absorption mechanisms are discussed for mediating positron localization either into the surface state or the anion band, special attention will be given to the zero energy threshold for producing PAES on KCl(100) surface.

i). Phonon, exciton or electron-hole excitations should be principally responsible for the energy released during positron trapping. One-phonon trapping is only important for shallow states at low temperatures as discussed in section 4.2. At the present measurement temperature range, detrapping from any shallow states will dominate so it can be neglected here. Multiphonon process is not important also since it has a far smaller cross section than , e.g., the electron-hole process. Our observed PAES signal intensity is of the same order even when positron incident energy is large enough for the electron-hole process to play a role , thus multiphonon process will not be important here (fig.4.6).

Considering the zero threshold energy for PAES in fig.4.6, electron-hole mediated trapping is energetically unfavorable if positron binding energy is on the order of 1-2 eV such as for the image-potential surface state. Electron-hole mediated trapping through the possible electron surface states or for positrons trapping into a deeper state is discussed below. As to the exciton energy release mechanism, its threshold (6-7 eV) can not explain the PAES zero energy threshold in fig.4.6c neither if there are possible positron surface states, though it may play a role at higher positron energies.

ii). Another trapping mechanism can be related to an Auger-like Ps breaking up process. Mills (1985) has proposed that positron emission from ionic solids may come from bulk formed Ps breaking up at the surface through an Auger-like process where the electron returns to the valence band and the positron gains the energy and reemits. We may also think of the opposite process with positron getting trapped while the electron gets emitted by gaining the energy. This picture is, however, discounted considering the complementary nature of PAES signal with that of Ps fraction (fig.4.6c). The same reason also excludes other possible contributions to PAES by Ps such as pick-up annihilations mentioned earlier.

iii). Positron trapping may be mediated by electron-hole excitations through possible surface electron states. The existence of surface electron state has been deduced in case of SiO_2 (Chen et al, 1987), and NaF (Mills, 1985) by the observation of the almost zero energy threshold for Ps formation, and in the later case, also by angle resolved photoemission experiment.

Not all the alkali halide surfaces possess electron surface states. Mills (1985) saw no sign of electron surface state on NaCl from the Ps measurement. From the current R-value measurement (fig.4.6b) alone, it is yet difficult to conclude about whether electron surface state exists due to the artificial Ps fraction around zero

energies in fig.4.6b. Contact charging as well as photoelectric emission study of KCl, however, have shown that extrinsic electron surface state exists about 4 eV below the vacuum level (Ernst, 1970). This still gives rise to a nonzero PAES threshold for electron-hole excitation of $\sim$ 1.5-2.5 eV, if the positron surface state binding energy is assumed $\sim$ 1 eV and positron workfunction is between 1.5 eV and 0.5 eV. Thus it is difficult to relate the zero energy threshold in fig.4.6c. to positron surface states.

The difficulties in i)-iii) for electron-hole mediated trapping are avoided if the positron binding energy is much larger than 1-2 eV. The possible positron state in the anion band is a good candidate for such a bound state. The large binding energy of which plus the energy gain for incident positrons due to the positive KCl surface workfunction may well excite electrons from either the valence band or the surface electron states for positrons to become localized.

The above discussion has been centered around the zero energy threshold of producing the PAES. At increased positron incident energies, electron-hole excitation can play a role in mediating epithermal positron trapping into the possible surface states. However, the energy scan of PAES in fig.4.6c up to 30 eV follows closely the change in the total annihilation counts. In other words, opening up the possibility of mediating positron trapping into the surface state does not observe any appreciable increase in PAES, we thus consider the positrons bound to the anion elements are the most possible candidates producing the Cl Auger electrons.

As to the temperature-dependent PAES shown in fig.4.8, there should be no appreciable surface structure changes on KCl(100) surface to the author's knowledge. If PAES is totally due to the positrons bound to the anion element, since their transport is hopping dominated as mentioned before, the transport efficiency will be described by a desorption-like behavior with enhanced diffusion ability at

elevated temperatures. Thus positrons which would have been localized near the surface producing PAES may now have the ability of wandering away from the surface region within which the Auger electrons may escape. PAES at high temperatures may then decrease as observed in fig.4.8. We have discussed in section 4.1 the possible bulk positron contributions to PAES in case bulk positron equilibrium state is delocalized. For KCl, if the equilibrium state is indeed the anion-positron bound state, the bulk positron contribution can be much more enhanced. Since first of all, it will be energetically unfavorable for the positrons bound to Cl ions to transit to any image-potential surface states, they will thus annihilate with Cl electrons and contribute to the PAES measurements directly. Secondly, positrons in anion band is more spatially localized (as compared with, e.g., the thermal positron de Brogile wavelength), thus if the positrons are bound in a subsurface region, they would mostly annihilate with core electrons in their immediate vicinities. The subsequent Auger electrons can then be detected if the core holes are located within the electron escape depths. Fitting of the temperature data with an activation model $\sim [A + B\exp(-\Delta E/k_B T)]^{-1}$ obtained an activation energy $\Delta E = 0.6$ eV. This is a reasonable value considering that Hughes (1975) obtained an activation energy of 0.6 eV for hole hopping transport in SiO_2.

We note also that we have carried a PAES measurement of Cu evaporation onto the KCl surface. Since no EAES measurements can be done to compare with the PAES results, and also due to the small mean-free-path of the Auger electrons at 181 eV, it is difficult to deduce whether positron surface states are evidenced in these data. And the result is not against the idea that positrons producing PAES are bound with the Cl ions.

In summary, surface state is not evidenced in the present PAES measurement on KCl(100) surface. Instead, positrons bound with the Cl ions are suggested as

responsible to the observed PAES signals.

§ 4.4 PAES Study of Ion Sputtering Damage of KCl(100) Surface

In this section, we'll examine the application of PAES to the study of ion sputtered KCl surface. The Cl LMM 181 eV Auger electrons produced by positron annihilation in the surface region is followed after sputtering . It is shown that the intensity of Cl PAES signal is very sensitive to the outmost layer(s) of the damaged surface, and indeed that PAES as an insulator surface probe induces negligible damage to the specimen. The experimental aspect of the measurement will be discussed in subsection 4.4.1; while the results and discussions will be presented in subsection 4.4.2.

4.4.1 The experimental aspects

In the present measurement, the moderator is biased at +30 Volts. The slow positrons are extracted and transported to the target biased at −10 Volts for PAES measurement, the nominal positron incident energy is thus $\sim$ 40 eV.

It should be emphasized that the 1D-PSD electron energy detection system shown in fig.2.1 is crucial here, since it enables rapid data acquisition for monitoring the surface defects annealing behavior. Other techniques such as the retarding grid energy analysis would be impractical because of the much longer data recording time compared with the typical defect annealing time.

The KCl sample is the same as described in section 4.3.1. The Ar^+ sputtering of the sample is done with a Varian ion gun titled $\sim 70^o$ with respect to sample surface normal. The sputtering energy is varied from 400 eV up to 3 keV under partial pressure $\sim 2 \times 10^{-4}$ torr. Ion gun emission is controlled at 30 mA, the sputtering current density at the sample is approximately 5 μ A/cm^2, though the uniformity of which is unknown. After the sputtering is stopped, it will take $\sim$ 10 minutes or longer to pump the inert gas away and reach the operating pressure in the high 10^{-9}

torr in our system. Apart from the waiting time after sputtering to pump the inert gas, additional minutes are spent to reach the specified temperature if temperature-dependent defects behavior is to be studied. The lower the temperature is, the longer it may take for the specified temperature to be reached during which time the sample may have already experienced some annealing. Thus more attention will be given to the qualitative features in the temperature dependence measurement. For the same reason, the time-dependent annealing is monitored with the sample at the same temperature as when the sputtering is done.

As will be discussed later, only a few K LMM 240 eV Auger electrons are seen immediately after sputtering, Cl LMM 181 eV Auger electrons are more dominant which can be easily monitored during the change of surface conditions. The grid before the 1D-PSD is set at −150 Volts and −210 Volts below the sample bias to obtain the Cl Auger electron energy spectrum and its background. Thus two spectra are recorded for each data point. The difference of which is considered to be measured Cl LMM 181 eV Auger electrons. The time needed for recording the Auger electron energy spectrum has to be well chosen. The data may have poor statistics if the acquisition time is too short. Longer acquisition time, on the other hand, may introduce poor time resolution as well as systematic errors for the measured time-dependent annealing behavior. For example, though we have attached a micro-ammeter between the sample and the ground during sputtering , the sample will still charge up after sputtering. The Auger electron energy peak position shifts upward as a consequence. Longer data acquisition time will see a much broadened spectrum after sputtering when compared with the spectrum of a well-annealed sample.

It should be noted that the observed PAES spectrum may contain contributions from different sources in the present set up. Most of them are related to the energy

resolving ability of PAES beam. The 1D-PSD geometry though provides efficient electron energy analysis, the overall energy resolution is degraded when compared with, e.g., the retarding grid method. Mayer et al (1990) reported the ability of the present PAES beam to resolve secondary electrons produced with the sample biases at negative 60 eV and 40 eV. This only represents an upper limit of the system resolution. For Auger electrons of the same energy as those secondary electrons, the sample is biased at a much lower voltage, thus Auger electrons will not be gaining much longitudinal energy as secondary electrons would when leaving the surface.

The Auger electrons are emitted basically isotropically from the target, a permanent magnet is applied behind the sample to enable the maximum solid angle of the CEMA over the sample as described in section 2.1. This solid angle, however, will be less at higher Auger electron energies since the initial almost isotropic angular distribution coupled with the higher energies will make the transverse-to-longitudinal energy conversion process less complete. The energy spread at the detector position will be wider as a consequence. This poses a problem with setting the low pass energy. If it is set too close to the Auger peak energy, much signal can be lost. In the current measurement, the dominant signal are the Cl LMM 181 eV Auger electrons. This peak will be shifted to 172 eV due to the magnetic field if the ratio of magnetic field at the sample vs. that at the 1D-PSD is 20:1 (assuming that the adibatic approximation is valid). Consider the resolution of 1D-PSD to be a Gaussian with a FWHM of 40 eV, and noting that the contribution outside 2σ (σ is the standard deviation of Gaussian distribution) would be $\sim$ 32%, or 16% on one side. The 22 eV difference between 150 eV pass energy and the 172 eV centroid would thus repel less than 16% Cl PAES 181 eV signal from 1D-PSD energy window.

The 16% would have not been so important if there is no sample charging after sputtering. Since the Auger peak can shift upwards in energy after sputtering, this in effect would vary the window setting for taking the Cl PAES spectrum. It will introduce an artificial increase in the present PAES intensity. If the charging voltage is assumed to be positive 10 Volts , the part of the 181 eV Auger peak cutoff by the low pass energy will be varying as the sample is annealed. The percentage of this cutoff will increase from $\sim$ 2% up to 16% .

The background for the Auger electron energy measurement is taken at 210 eV pass energy for the Cl(LMM) Auger electron. If higher energy Auger electrons, e.g., the K (LMM) 240 eV Auger electrons are present, its peak position will also be shifted down to $\sim$ 228 eV due to the magnetic field. The tail region of these Auger electrons extending below the 210 eV pass energy is also $\sim$ 16% of the total intensity. Fortunately, positrons have far smaller probability of approaching K^+ ions and producing K (LMM) Auger electrons. Assume that K Auger signal strength is one-tenth of the Cl Auger signal, we estimate the contribution of the K (LMM) tail towards the measured Cl (LMM) Auger spectrum is less than 0.1 $\times$16% or 1.6%. This contribution is in fact reducing the effect due to the cutoff of Cl signal. When sample charging occurs, the K signal will be mostly shifted out of the energy window defined for Cl Auger signal.

The above discussed systematics for measuring the Cl(LMM) Auger intensity may need not to be concerned if, e.g., one is only looking for signs of complete annealing of the surface, since both the charging and the K (LMM) Auger signal will disappear as annealing is done. On the other hand, understanding of the system resolution will help to distinguish the different sources if so desired. An improved beam design and electron detection system will help greatly in dealing with these problems.

4.4.2 Results and discussions

Typical KCl PAES spectra after sputtering and annealing are as shown in fig.4.11. The sputtering is done at 250°C with ion energy 400 eV for 10 minutes. Fig.4.11a and 4.11c is the foreground with pass energy set at 150 eV, fig.4.11b and 4.11d is the background with the pass energy set at 210 eV . Figs.4.11a and 4.11c are the measurements 10 minutes after the sputtering, while figs.4.11b and 4.11d are for well-annealed sample taken about 20 hours after the sputtering. Each spectrum is recorded over a time of 150 seconds.

It is seen that the Auger electron intensity is much enhanced after ion sputtering. As discussed in subsection 4.4.1, there are some systematic effects which may contribute to this enhancement such as sample charging. The charging is related to Ar^+ sputtering by the observation that prolonged sputtering increases the Auger peak upper-shift. This charging can not be explained by the direct Ar^+ beam bombardment, though its current density is about 10^6 times of the positron beam . Since if Ar^+ ions are implanted into the insulator or being neutralized by electrons from the insulator, the sample surface should be positively charged, which will cause the Auger energy peak shift to the lower energy side. It is plausible to assume here that secondary effects related to the Ar^+ bombardment is important in deciding the charging behavior. Examples of which may include charged defects generation on the surface or positive ion sputtering. The annealing of the sample with either time or temperature will see the Auger peak shifting downward and its intensity decreasing until stabilized (fig.4.11). There is also the contribution from the low energy tail region of the K LMM 240 eV Auger electron included in Fig.4.11a. Fig.4.11b shows the small K LMM Auger signal which would otherwise be a flat background as 4.11d. In a well-annealed sample, no K Auger signals can be seen above the detectable limit by sweeping the pass energy above and below

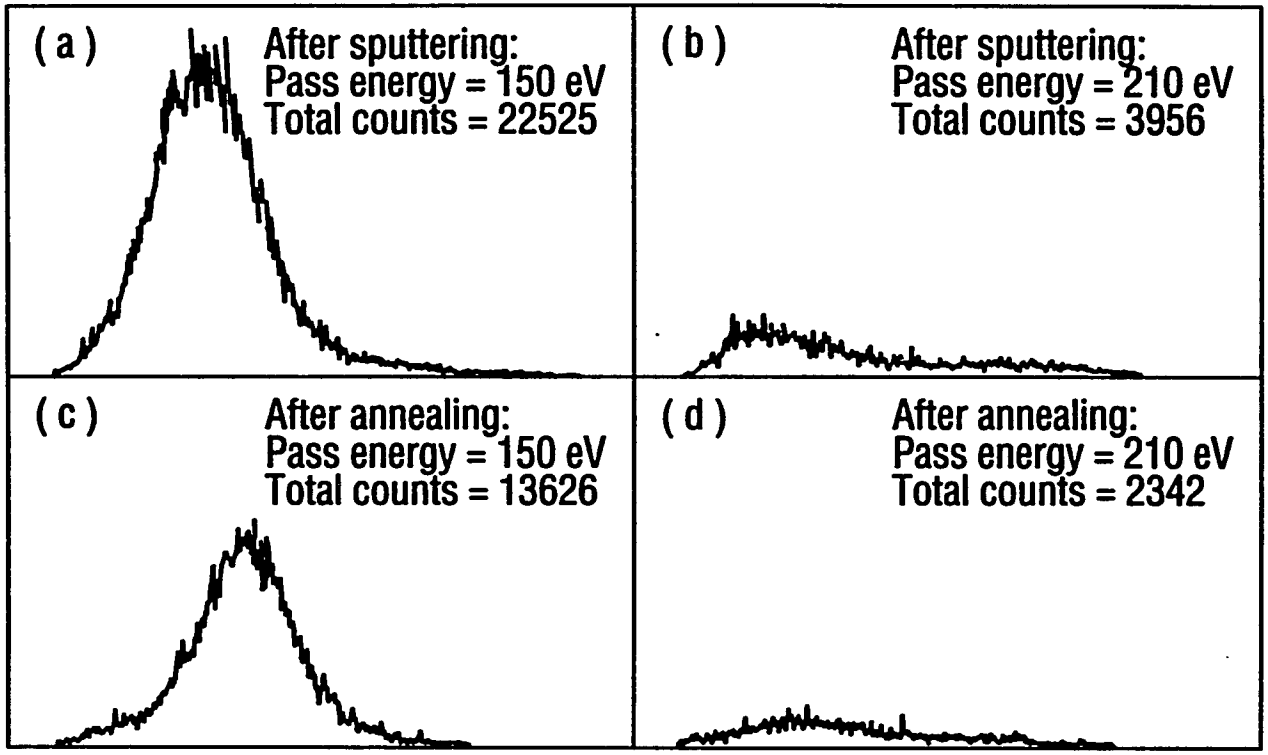

Fig.4.11 The PAES spectra for KCl(100) surface after sputtering(a,b) and annealing(c,d). (a,c) are taken at pass energy 150 eV, (b,d) are taken at pass energy 210 eV.

the K Auger electron energy. We have discussed in section 4.3 that PAES is possibly due to positrons in an anion band for a clean sample. It is believed that the detection of K LMM 240 eV Auger electrons after sputtering is related to surface defects which changes the relative electronic configuration of positrons with respect to the cation element (e.g., changes in the charge state), introducing finite potassium core electron annihilation probabilities. The weak intensity and the spread of the K LMM Auger electron peak make it difficult to monitor the K Auger signal totally independent of the Cl signal. Thus it is the Cl Auger signal that is given the most attention, though one example of monitoring the K LMM Auger signal will be shown later.

It would be useful at this point to estimate the contribution of real Cl Auger signal apart from other systematic effects. Estimate in subsection 4.4.1 shows that sample charging or K Auger signal contribution contribute $\sim$ 16% to the "measured" Cl signal. Since the increase in the "measured" Auger intensity after sputtering is about 90% as compared to well-annealed sample in fig.4.11. Cl LMM 181 eV Auger electrons are increased by about 74% after the ion sputtering.

Simultaneous measurement of positron annihilation γ-ray energy spectrum is also carried. No systematic o-Ps effects are observable for given positron incident energies at different surface conditions. Ortho-Ps formation is seen to be dependent on the incident energy of the positrons (fig.4.6), which is considered to be mostly taking place in near-surface regions. Thus o-Ps fraction may not be sensitive towards the top surface conditions. The fact that little Ps signal change is observed shows that PAES technique is only sampling a few outmost layers. It also indicates that the amount of damage in our experiment does not affect the electronic structure of the near surface region very much, which is possibly the reason that the fraction of Ps before and after sputtering is essentially unchanged.

It is found that PAES signal decreases as the ion sputtering energy increases.

For positron incident energy between 40-100 eV, the Auger signal intensity at 2 keV sputtering energy is reduced by 40-60% as compared with 400 eV sputtering energy case. This may possibly mean that a) the surface defects is related to bulk defects diffusion back to the surface. Defects created by 2 keV ions will be located farther away from the surface and thus having less chance to diffuse back to the surface; and/or b) more ion energy will be dissipated in the near-surface region instead of the very surface layers, so there is less damage in the most sensitive region of PAES. It is also found that higher incident energy positrons will have a larger percentage decrease in PAES signal for the two ion sputtering energies. This is attributed to the possible more efficient sub-surface trapping for higher incident energy positrons, which will reduce the number of positrons coming back to the surface and contributing to PAES signal.

The above measurements suggest the high surface sensitivity of PAES measurement considering the low energy of the probing positrons and the sputtering ions. Though the quantitative evaluation of the sensitive region of PAES is difficulty to obtain due to the lack of the knowledge for the low energy ions and positrons of interest, it will at least be comparable to EAES. The EAES sensitive region is defined by the IMFP of the Auger electrons, which for Cl LMM 181 eV electron is $\sim$ 8Å.

To discuss the possible positron trapping sites on the KCl surface, it would be necessary to look into the microscopic defects generation process in insulators under ion bombardment as well as the possible trapping sites for positrons on the surface.

There are two types of defect-creating process (Itoh, 1976) in KCl, one due to the nuclear elastic collision displacing lattice ions, and the other electronic excitation mediated defects production through, e.g., exciton diffusing to and decay

at the surface. The nuclear process would be important for heavier projectile or smaller incident energies. Under the present experimental conditions, the elastic displacement should be more dominant.

Microscopically, ion bombardment will erode the surfaces producing pits. This pits consist of steps and terraces of various lengths that expand on annealing. These local redistribution of atomic configurations will induce changes in electronic configuration which will modify the positron trapping and annihilation environments subsequently. Apart from the direct damage of the surface , the ion beam induced bulk defects (vacancy, interstials and their complexes) may also induce surface defects. For example, as discussed previously, formation of surface kinks can be as a result of the formation of charged defects in the bulk such as cation or anion vacancies (Short et al, 1972). Kinks are the atomically "vacant" sites (see, e.g., Köymen et al, 1987) on a stepped surface which will be attractive to positrons. Another note is that though halogen atoms are found to be preferentially ejected during ion sputtering through mass spectrometry measurement (Itoh, 1976), we still observe an increased Cl LMM PAES signal. This does not necessarily indicate that there is an increment of Cl species on the surface, since positrons will selectively chose their preferred annihilation site.

The annealing behavior of the surface defects can also be studied through PAES measurement. The time-dependent Cl LMM Auger electron intensity is as shown in fig.4.12. The sample is sputtered at 400 eV for 10 minutes. Measurement starts about 10 minutes after the sputtering at temperature 200°C. We have fitted it to an exponential (The solid curve) $C_1 \exp(-t/\tau) + C_2$. The obtained time constant τ for the annealing is $\sim$ 39(3) minutes (noting that τ obtained here does not include the 10 minutes of waiting time, neither will the time constants obtained below

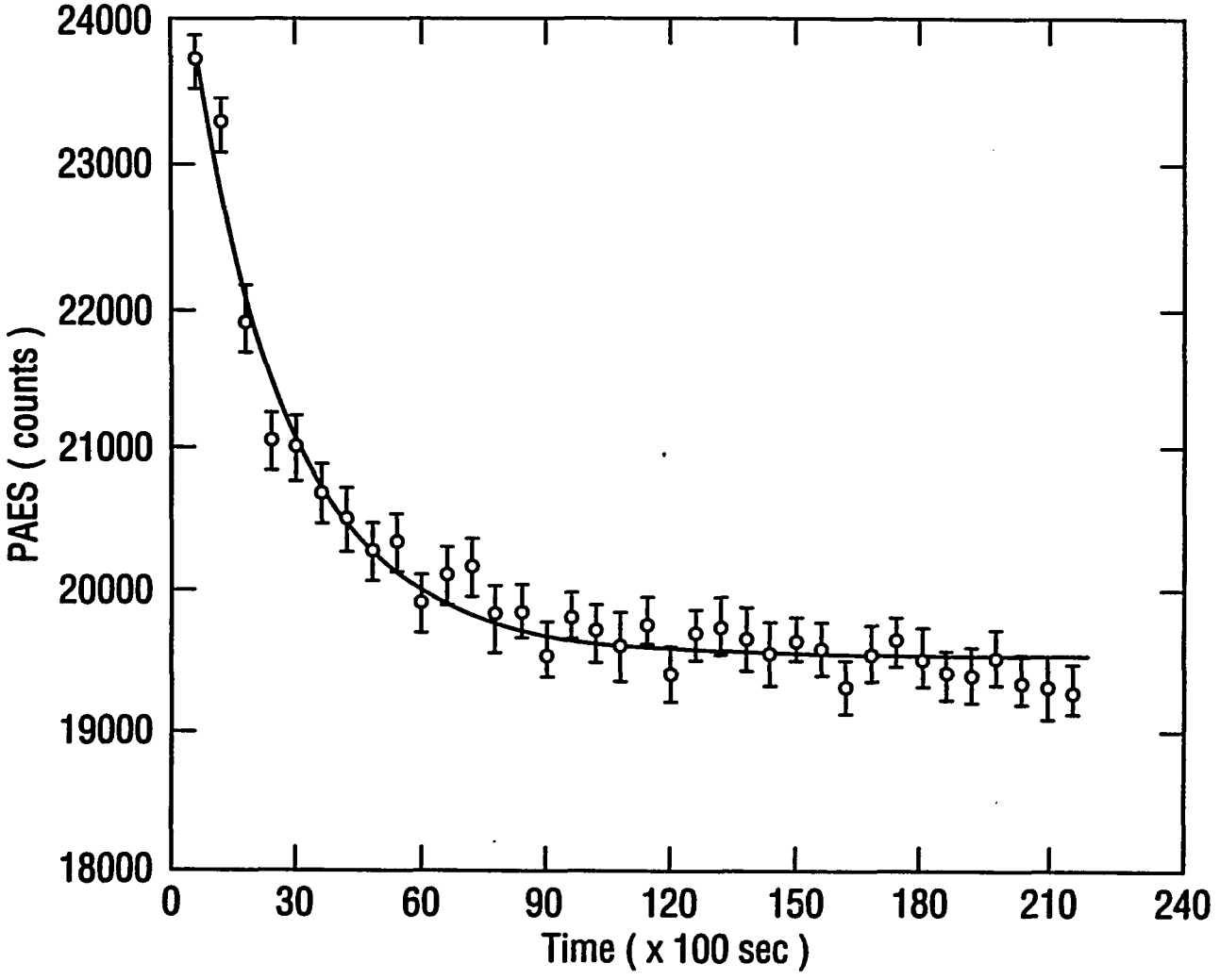

Fig.4.12 The time-dependent Cl LMM 181 eV PAES intensity after the sample is sputtered by 400 eV Ar^+ ions.

do). $C_2/(C_1 + C_2)$ would be representative of the ratio of PAES signal of a clean sample vs that of a sputtered sample. We note here that at longer times, the Auger intensity shows little time dependence. Though the positron beam intensity is also reducing with time due to the evaporation of the Ne, its rate will be too slow to have observable effects in fig.4.12. It can thus be concluded from fig.4.12 that there is indeed no observable beam damage on the KCl surface related to positrons. PAES is also carried after the sample is heated for more than 20 hours. It is found that the positron beam does not generate any time-dependent Auger signals, thus confirming the non-destructive nature of PAES technique. In case of EAES, time-dependent characteristics of the surface have long been found due to electron induced damage such as surface metallization (Itoh, 1976).

Fig.4.13 shows another set of data for a sample sputtered at 2 keV for 8 minutes with a measurement temperature 220°C. Fig.4.13a is the counts within the energy window of [150,210 eV] for Cl LMM PAES signal; while fig.4.13b is the counts of the spectrum with pass energy 210 eV. The spectrum in 4.13b should consist of K LMM PAES signal and a constant background. We have fitted the above exponential expression for both fig.4.13a and 4.13b. The time constant in 4.13a is 160(50) minutes which is much larger than the obtained τ for fig.4.12. This increased time constant is possibly related to the larger sputtering energy in the present case. This will generate defects farther away from the surface thus taking longer time to anneal out. A time constant of 26(2) minutes is found for 4.13b which characterizes the decaying of K (LMM) Auger electrons. The large difference in the time constants should reflect that the K(LMM) Auger electrons associated defects decaying is not totally the same process as that is governing the Cl(LMM) Auger electrons. So there can be more than one kind of defects present in this case.

The temperature dependence of the Cl Auger signal intensity is shown in

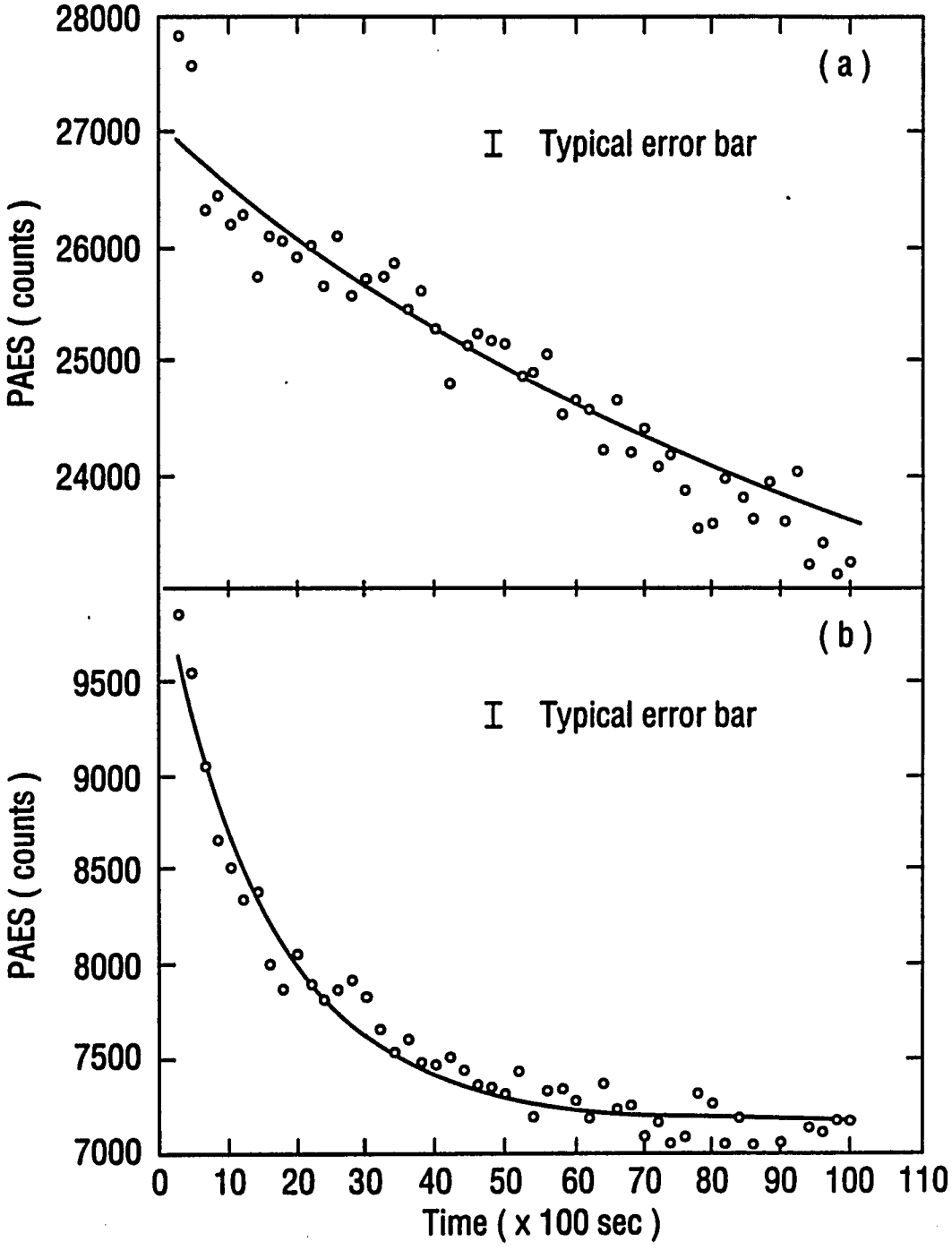

Fig.4.13 a) The time-dependent Cl LMM 181 eV PAES intensity after the sample is sputtered by 2 keV Ar^+ ions. b) The time-dependent counts from the spectrum corresponding to 210 eV pass energy after the sample is sputtered by 2 keV Ar^+ ions, it characterizes the annealing of K LMM 240 eV Auger signal related defects. Measurements are carried at 220 °C.

fig.4.14. PAES measurement is carried for three annealing cycles with temperature increasing, decreasing and increasing again. The sputtering is done at 400eV energy for 10 minutes, and necessary waiting time is spent at each temperature before the data acquisition begins. An interesting property is that there always exists a desorption-like feature after sputtering for the first annealing cycle. The transition temperature is around 230°C . The second (temperature decreasing) and the third cycle(temperature increasing) of the annealing process have PAES counts close to each other indicating the near completion of the annealing process.

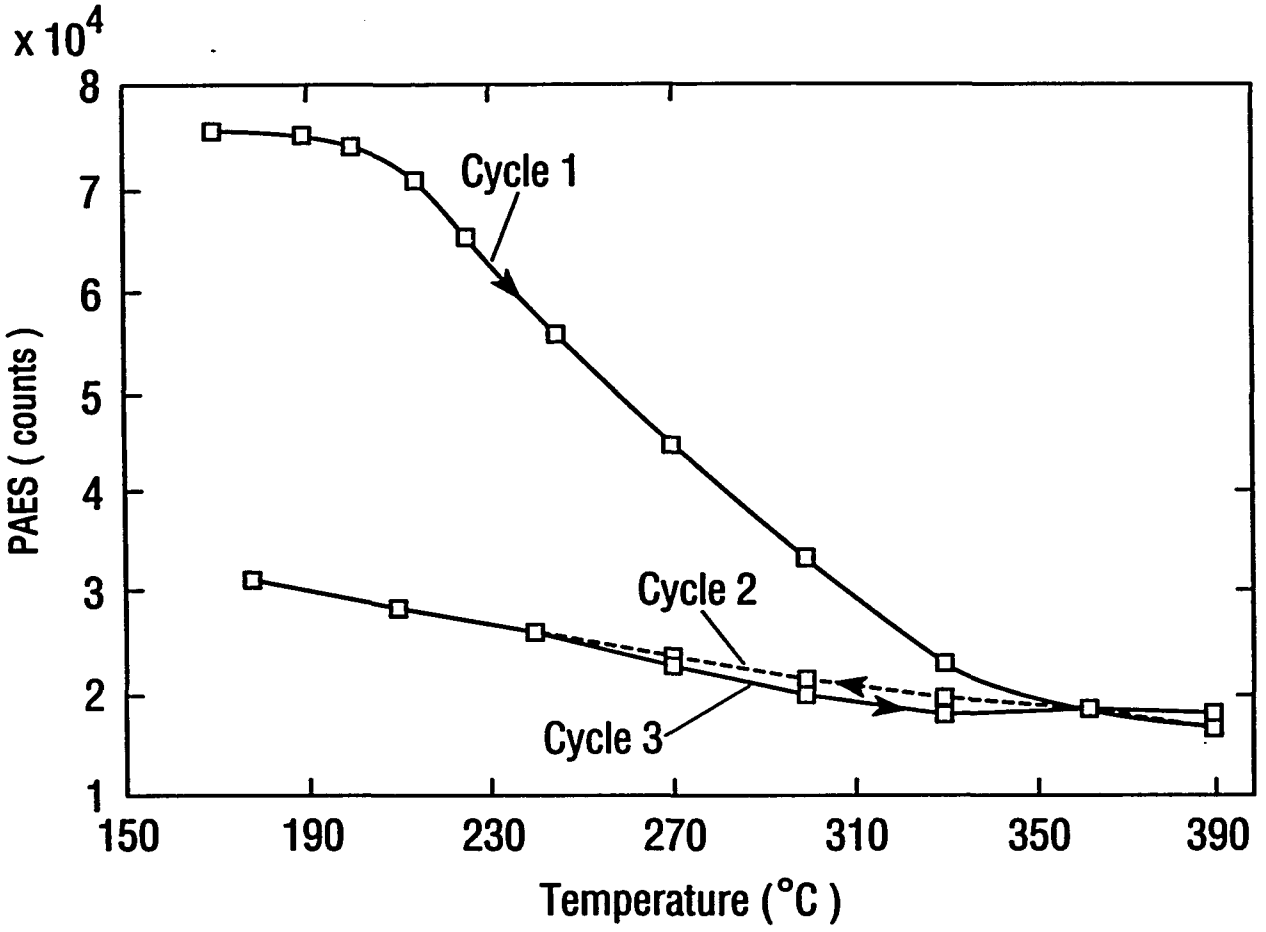

Fig.4.14 The temperature-dependent Cl LMM 181 eV PAES signal after the sample is sputtered by 400 eV Ar^+ ions.

Chapter 5
SUMMARY

In the present thesis research, we have carried studies of the positron transport in solids and its interaction with surfaces.

Our efforts in studying positron transport in solids are centered around the proper modelling of epithermal positron transport behaviors in the solids, and the possible slow positron techniques for studying positron transport behaviors in systems which may otherwise be difficult to evaluate with conventional means.

The modelling of thermal and epithermal positron transport in solids is one of the first efforts in this field. A two-stream and two-level model is explicitly developed and solved there, and a two-stream and many-level model formulation is also shown. Epithermal positron transport is considered in addition to the thermal positrons. It thus presented with us a more complete picture of positron slowing down and transport in solids. The usual implantation-diffusion model is replaced by the more complete implantation-thermalization-diffusion model. Quantitative information may then be obtained on positron transport and positron-surface interactions (e.g., Soininen et al, 1989; Britton et al, 1989). Analysis from our model justified the positron diffusion data analysis technique adopted by Huomo et al (1989). It also provided results agreeing with some preliminary experimental measurement of epithermal positron reemissions (Fischer, 1986; Nielsen, 1987). Further, application of our developed model towards cases such as a metal bilayer system points out to the possibilities of utilizing epithermal positrons in studying surfaces and interfaces. The present model is applicable to the study of thin metal films by

the reemitted positron spectroscopy (e..g., Gidley and Frieze, 1988), from which the positron work function, mean free path, and thermalization rate can be deduced. However, it should be remarked that the present model is unable to obtain the detailed energy distributions of the epithermal positrons, nor the the temperature dependence of the epithermal positron behaviors. The model itself is essentially phenomenological, a more *ab initia* approach will have to be adopted in achieving these capabilities.

Experimentally, we have employed two techniques for studying the positron transport behaviors. By using a MOS structure, positron mobility in thermally grown SiO_2 is evaluated with Doppler broadening measurement. The sandwiched structure of the sample presents high sensitivity of this measurement towards the small positron mobilities in insulators. In fact, with this technique, the measurable positron mobility is four orders of magnitude smaller than the positron mobilities in Si or Ge. The quantitative assessment of positron mobility in the SiO_2 is interesting because it may help other positron studies of the MOS structures (Leung et al, 1991). On the other hand, positron mobility in SiO_2 can be characteristic the oxide conditions due to the indicated positron sensitivity towards the oxide defects. Another technique, the positron annihilation γ-ray energy centroid shift measurement, is applied towards the positron transport in the Si near-surface region buried below the Al and the SiO_2 overlayers. This technique is predominantly probing annihilating positrons in drift motion in a electric field. The agreement between the observed centroid shifts and the simple diffusion model adopted there provides with us the understanding of the underlying physical processes. This understanding is important for the possible application of the positron annihilation γ-ray centroid shift technique in studying the interface properties.

The other important theme of the present thesis is positron-surface interactions

with emphasis on the positron trapping into the surface potentials. First of all, we have pointed out that the thermal positron reflection by the surface potential is more substantial than predicated by a simple potential step model (Nieminen and Oliva, 1980). The potential well effect will reduce the positron transmission through the surface potential by an order of magnitude or more. Positrons will have to approach the surface many times to participate the surface escape processes. With this multiple-encounter picture, we may interpret the measured positron internal surface reflection coefficients more physically. The anomalous observation of the non-vanishing PAES signal at Ge(100) surface at high temperatures (Soininen et al, 1991) is also suggested to be associated with this strong reflection. In another effort, the excited Rydberg surface states associated with the long range nature of the positron-surface image potential are considered for the first time. Electron-hole, as well as phonon excitations in absorbing the energies released by positron localization into the surface potentials are studied. One-phonon excitation, which may have comparable cross section to that of electron-hole excitations at low temperatures, is found to be important under suitable conditions. This conclusion provides the theoretical basis for the observation of a possible enhanced surface trapping into the Ag(111) surface at low temperatures (Kong et al, 1991).

Experimentally, the positron annihilation induced Auger electron spectroscopy (PAES) is utilized in studying an ionic insulator surface: KCl(100). The energy-dependent and temperature-dependent measurements of the PAES revealed that the Auger electrons are most possibly due to subsurface positrons bound to the Cl ions. This conclusion mainly resulted from the observed zero positron energy threshold for producing the PAES on KCl(100) surface and the analysis of the positron trapping mechanisms. The temperature-dependent PAES measurement reveals a thermal activated process which we have suggested as related to the hopping transport of

positrons bound to the Cl ions. Cu evaporation results indicated no inconsistency with the above suggested picture.

In another study, PAES technique is also examined for its non-destructiveness and surface sensitivity in serving as a surface probe for insulators. By measuring the non-equilibrium defects created by ion-sputtering of KCl(100) surface, PAES is shown to be not causing additional damage to the sample as other charged-particle surface probes may do due to the associated current and energy. It is thus promising to apply the PAES for evaluating the fragile or insulating surfaces. In case Ps fraction can be of additional useful parameter, PAES in the field of surface study could provide information on both the surface chemistry and electronic structure changes non-destructively. We have recently proposed the positron annihilation induced Auger electron microscopes (PAEM) technique (Kong, 1991) which can be very important in revealing surface properties unavailable with other means. It should also be noted that the advantage that positron is attracted to defects may also be its disadvantage. Since this would mean a selective trapping and annihilation site for positrons which could complicate the data interpretation. The needs for the existence of substantial PAES signal usually requires positron surface trapping centers exist in the surface studied and core annihilation rate there have to be reasonable.

In conclusion, the present thesis study provided new understandings and developments of the positron solid state physics. Positron technique is rapidly becoming a reality during a short lifetime since the discovery of positrons. With the future availability of more intense positron beams as well as the more advanced positron techniques, positron will sure be developed into an important probe unique and complementary to other existing means.

REFERENCES

Ashcroft, N.W., and N.D. Mermin, **Solid State Physics**, Holt, Rinehart and Winston, Philadelphia, 1976.

Baker, J., N.B. Chilton, P.G. Coleman in **Positron Beams for Solids and Surfaces**, AIP Conference Proceedings 218, edited by P.J. Schultz, G.R. Massoumi, P.J. Simpson, American Institute of Physics, New York, 1991.

Beck, G., Rev. Sci. Instr., **47**, (1976), 849.

Beling, C.D., R.I. Simpson, M. Charlton, F.M. Jacobson, T.C. Griffith, P. Moriarty and S. Fung, Appl. Phys., **A42**, (1987), 111.

Bergersen, B., E. Pajanne, Appl. Phys., 4, (1974), 25.

Bergersen, B., E. Pajanne, P. Kubica, M.J. Stott, and C.H. Hodges, Solid State Comm. **15**, (1974), 1377.

Bernasconi, J., E. Cartier and P. Pfluger, Phys. Rev. B38, (1988), 12567.

Brandt, W., and R. Paulin, Phys. Rev. **B15**, (1977), 2511.

Brandt, W., in **Positron Solid State Physics**, edited by W. Brandt and A. Dupasquier, North-Holland, Amsterdam, 1983.

Brandes, G.R., K.F. Canter, A.P. Mills, Jr., Phys. Rev. Lett., **61**, (1988), 488.

Brandes, G.R., Phys. Rev. **B43**, (1991), 10111.

Brandes, G.R., K.F. Canter, A.P. Mills, Jr., Phys. Rev. **B43**, (1991), 10103.

Britton, D.T., P.C. Rice-Evans and J.H. Evans, Phil. Mag. Lett., **57**, (1988), 165.

Britton, D.T., and Rice-Evans, P.C., Phys. Stat. Sol., **B147**, (1988), 89.

Britton, D.T., P.A. Huttunen, J. Mäkinen, E. Soininen, and A. Vehanen, Phys. Rev. Lett., **62**, (1989) 2413.

Candy, B.H., Rev. Sci. Instr., **56**, (1985), 183.

Canter, K.F., P.G. Coleman, T.C. Griffith, and G.R. Heyland, J.Phys. **B5**, (1972), L167.

Canter, K.F., A.P. Mills and S. Berko, Phys. Rev. Lett., **33**, (1974), 7.

Canter, K.F., in **Positron Beams for Solids and Surfaces**, AIP Conference Proceedings 218, edited by P.J. Schultz, G.R. Massoumi, P.J. Simpson, American Institute of Physics, New York, 1991.

Chandrasekhar, S., **Radiative Transfer**, Clarendon Press, Oxford, England, 1950.

Chantry, C.H., A.V. Phelps and G.J. Schultz, Phys. Rev., 152, (1966), 81.

Chen, Y.C., K.G. Lynn and B. Nielsen, Phys. Rev., B**37** (1988), 3105.

Cheery, Ph.D Thesis of Princeton University, unpublished, (1958).

Chu, S., A.P. Mills, Jr., and C.A. Myrray, Phys. Rev. B**23**, 2060.

Dannefear, S., S. Kupca, B.G. Hogg, and D.P. Kerr, Phys. Rev., B**22**, (1980), 6135.

DeBenedetti, S., C.E. Cowan, and W.R., Konneker, Phys. Rev., **76**, (1949), 440.

Dupasquier, A., in **Positron Solid State Physics**, edited by W. Brandt and A. Dupasquier, North-Holland, Amsterdam, 1983.

Eldrup, M., A. Vehanen, P.J. Schultz and K.G. Lynn, Phys. Rev., B**32**, (1985), 7048.

Ernst, L., Surf. Sci., **176**, (1986), L825.

Feldman, L.C., and J.W.Mayer, **Fundamentals of Surface and Thin Film Analysis**, North-Holland, Amsterdam, 1986

Fischer, D.A., K.G. Lynn and W.E. Frieze, Phys. Rev. B**33**, (1986), 4479.

Fischer, D.A., unpublished results, (1986).

Gidley, D.W., and W.E. Frieze, Phys. Rev. Lett. **60**, (1988), 1193.

Gullikson, E.G., A.P. Mills, Jr., Phys. Rev. Lett. **57** (1986) 1828.

Gullikson, E.G. and A.P. Mills, Jr., and C.A. Murray, Phys. Rev. B**38**, (1988), 1705.

Hodges, C.H., Phys. Rev. Lett., **25**, (1970), 284.

Hodges, C.H., M. Stott, Solid State Commun., **12**, (1973), 1153.

Horsky, T.N. G.R. Brandes, K.F. Canter, P.H. Lippel, and A.P. Mills Jr., Phys. Rev., B40, (1989), 7898.

Howell, R.H., I.J. Rosenberg, and M.J. Fluss, Phys. Rev. B34, (1986), 3069.

Howell, R.H., I.J. Rosenberg, P. Meyer, and M.J. Fluss, Phys. Rev. B35, (1987), 4555.

Hughes, R.C., Phys. Rev. Lett., 30, (1973), 1333.

Hughes, R.C., Appl. Phys. Lett., 26, (1975), 436.

Hughes, R.C., Phys. Rev., B15, (1977),2012.

Huomo, H., A. Vehanen, M.D. Bentzon and P. Hautojarvi, Phys. Rev. B 35, (1987), 8252.

Huomo, H., E. Soininen and A. Vehanen, Appl. Phys., A49, (1989), 647.

Hutchins, S.M., P.G. Coleman, R.J. Stone and R.N. West, J. Phys., E19, (1986), 282.

Ikari, H., and K. Fujiwara, p.617 in **Positron Annihilation** , edited by R.R. Hasiguti and K. Fujiwara, Aoba Aramaki, Sendai 980, Japan, 1979.

Ito, Shin, Sakae Shimizu, Tatsumi Kawaratani, and Ken-ichi Kubota, Phys. Rev., A22, (1980), 407.

Itoh, N., Nucl. Instrum. and Meth. 132, (1976), 201.

Jackson, J.D., **Classical Electrodynamics**, John Wiley & Sons, Inc., (1975).

James, F. and Roos, M., MINUIT CERN program library, D506, (1983).

Jaynes, IEEE. Tran., Proc., 70, (1982), 939.

Jennings, P., Surf. Sci., 198, (1988), 180.

Jensen, K.O., and A. Weiss, Phys. Rev. B41, (1990), 3928.

Jorch, H.H., unpublished results, (1981).

Khatri, R., M. Charlton, P. Sferlazzo, K.G. Lynn, A.P. Mills, Jr., and L.O. Roellig, Appl. Phys. Lett. 57, (1990), 2374.

Knoll, G.F., **Radiation Detection and Measurement**, John Wiley & Sons, New York, 1979.

Kögel, p.383 in **Positron Annihilation** , edited by R.R. Hasiguti and K. Fujiwara, Aoba Aramaki, Sendai 980, Japan, 1979.

Kong, Y., and K.G. Lynn, Phys. Rev. B41, (1990), 6179 and 6185.

Kong, Y., R.M. Nieminen, P.A. Huttunen, A.Vehanen, J. Makinen, in **Positron Beams for Solids and Surfaces**, AIP Conference Proceedings 218, edited by P.J. Schultz, G.R. Massoumi, P.J. Simpson, American Institute of Physics, New York, 1991.

Kong, Y., and K.G. Lynn, Nucl. Instr. and Meth., A**302**, (1991), 145.

Kong, Y., unpublished, (1991).

Köymen, A.R., D.W. Gidley and T.W. Capehart, Phys.Rev. B**35**, (1987), 1034

Kubica, P., and A. T. Stewart, Phys. Rev. Lett. **34**, (1977), 852.

Laermans, C., A. Vanelstraete, D. Segers, M. Dorikens, L. Dorikens-Vanpraet, J. Cornelis, A. Vanden Bosch, p.863 in **Positron Annihilation**, edited by L. Dorikens-Vanpraet, Singapore,World Scientific, 1989.

Law, J., and Hogan, D., Nucl.Instr. and Meth., B**5**, (1984), 67.

Lax, M., Phys. Rev, **119**, (1960), 1502.

Lei, C., M.S. Thesis, Univ. Texas at Arlington, unpublished, (1988).

Lei, C., D. Mehl, A.R. Köymen, F. Gotwald, M. Jibaly and A. Weiss, Rev. Sci. Instr., **60**, (1988), 3656.

Leung, T.C., Z.A. Weinberg, P. Asoka-Kumar, B. Nielsen, G.W. Rubloff and K.G. Lynn, unpublished, (1991).

Lieu, R., R.B. Hicks, C.J. Bland, J. Phys., A**20**, (1987), 2379.

Lynn, K.G., Phys. Rev. Lett., **43**, (1979), 391.

Lynn, K.G., Phys. Rev. Lett., 44(1980) 1330.

Lynn, K.G., and H. Lutz, Rev. Sci. Instrum. **51**, (1980), 977.

Lynn, K.G., in **Positron Solid State Physics**, edited by W. Brandt, and A. Dupasquier, North-Holland, Amsterdam, 1983.

Lynn, K.G., W.E. Frieze, and P.J. Schultz, Phys. Rev. Lett. **52** (1984) 1137.

Lynn, K.G., A.P. Mills, Jr., R.N. West, S. Berko, K.F. Canter, and L.O. Roellig, Phys. Rev. Lett., **54**, (1985), 1702.

Lynn, K.G., T. McKay and B. Nielsen, Phys. Rev. B36, (1987), 7107.

Lynn, K.G., B. Nielsen and D.O. Welch, Can. J. Phys.,**67**, (1989),818.

Lynn, K.G., E. Gramsch, S.G. Usmar and P. Sferlazzo, Appl. Phys. Lett., **55**, (1989), 87.

Lynn, K.G., M. McKeown, private communication, (1990).

Luhr-Tanck, W., Th. Kurschat and Th. Hohenkamp, Phys. Rev. B31, (1985), 6994.

MacKenzie,I.K., in **Positron Solid State Physics**, edited by W. Brandt and A. Dupasquier, North-Holland, Amsterdam, 1983.

Madanski, L., and F. Rasetti, Phys. Rev., **79**, (1950), 397.

Mahan, G.D., J. Appl. Phys. **58**, (1985), 2242.

Manninen, M., and R.M. Nieminen, Appl. Phys. A**26**, (1981), 93.

Manuel, A.A., in **Positron Solid State Physics**, edited by W. Brandt and A. Dupasquier, North-Holland, Amsterdam, 1983.

Mayer, R., D. Baker, A. Schwab and A. Weiss, Rev. Sci. Instrum. **61**, (1990) 42.

Mayer, R., A. Schwab and A. Weiss, Phys. Rev. B**42**, (1990),1881.

Mehl, D., A.R. Köymen, K.O. Jensen, F.G. Gotwald and A. Weiss, Phys. Rev., B**41**, (1990), 799.

McMullen, T. and M. Stott, Phys. Rev. B**34**, (1987), 8985.

Mills, A.P., Jr., and L. Pfeiffer, Phys. Lett. 63A, (1977), 118.

Mills, A.P., Jr., Phys. Rev. Lett.,**41** (1978) 1828.

Mills, A.P., Jr., P.M. Platzman, B. Brown, Phys. Rev. Lett., **41** (1978) 1076;

Mills, A.P., Jr., and C.A. Murray, Appl. Phys. **21**,(1980) 323.

Mills, A.P., Jr., and R. Wilson, Phys. Rev. **A26**, (1982), 490.

Mills, A.P., Jr., and W.S. Crane, Phys. Rev. Lett **53**, (1984), 2165.

Mills, A.P., Jr., and W.S. Crane, Phys. Rev. lett., **31**, (1985), 593.

Mills, A.P., Jr., in **Positron Studies of Solids, Surfaces, and Atoms**, edited by A.P. Mills, Jr., W.S. Crane and K.F. Canter, World Scientific, 1985.

Mills, A.P., Jr., and E.M. Gullikson, Appl. Phys. Lett., **49**, (1986), 1121.

Mills, A.P., Jr., E.D. Shaw, R.J. Chichester and D.M. Zuckerman, Phys. Rev. **B40**, (1989), 8616.

Mills, A.P., Jr., E.D. Shaw, M. Leventhal, P.M. Platzman, R.J. Chichester, D.M. Zuckerman, T. Martin, R. Bruinsma and R.R. Lee, Phys. Rev. Lett., **66**, (1991), 735.

Nieminen, R.M., and J. Oliva, Phys. Rev. **B26**, (1980), 2226.

Nieminen, R.M., in **Positron Solid State Physics**, edited by W. Brandt and A. Dupasquier, North-Holland, Amsterdam, 1983.

Neilson, D., R.M. Nieminen, and J. Szymanski, Phys. Rev. **B33**, (1986), 1567.

Nielsen, B., K.G. Lynn, A. Vehanen, P.J. Schultz, Phys. Rev. **B32**, (1985), 2296.

Nielsen, B., K.G. Lynn and Y.C. Chen, Phys. Rev. Lett. **57**, (1986), 1789.

Nielsen, B., K.G. Lynn, Y.C. Chen and D.O. Welch, Appl. Phys. Lett., **51**, (1987), 1022.

Nielsen, B., unpunlished data, (1987).

Nielsen, B., K.G. Lynn, D.O. Welch, T.C. Leung, G.W. Rubloff, Phys. Rev. **B40**, (1989), 1434.

Nuramagambetov, S.B., in **Positron Annihilation**, edited by P.C. Jain, R.M. Singru and K.P. Gopinathan, World Scientific, 1985.

Pantano, C.G., and T.E. Madey, Appl. Surf. Sci., **7**, (1981), 115.

Perkins, A., and J.P. Carbotte, Phys.Rev., **B1**, (1970), 101.

Palmberg, P.M., and T.N. Rhodin, J. Phys. Chem. Solids, **29**,(1968), 1917.

Press,W.H., B.P. Flannery, S.A. Teukolsky, W.T. Vetterling, **Numerical Recipes**, Cambridge University Press, 1986.

Puska, M., and M.M. Manninen, J. Phys., **F17**, (1986), 2235.

Puska, M., C. Corbel and R.M. Nieminen, Phys. Rev., **B41**, (1990), 9980.

Puska, M., Private commiuncation, (1991).

Rubloff, G.W., J. Vac. Sci. Technol. **A8**, (1990), 1857.

Saarinen, K., P. Hautojarvi, A. Vehanen, R. Kruse, and G. Dblubek, Phys. Rev., **B39**, (1989),5287.

Schaffer, J.P., and Jones, P.L., J. Phys., **F16**, (1986), 1885.

Schödlbauer, D., G. Kögel, P. Sperr, and W. Triftshäuser, Phys. Status. Solidi., **A102**, (1987), 549.

Schultz, P.J., K.G. Lynn, and B. Nielsen, Phys. Rev. **B32**, (1985), 1369.

Schultz, P.J., and K.G. Lynn, Rev. Mod. Phys. **60**, (1988), 701.

Schultz, P.J., E. Tandberg, K.G. Lynn, B. Nielsen, T.E¿ Jackman, M.W. Denhoff, and G.C. Aers, Phys. Rev. Lett., **61**, (1988), 187.

Schut, H., A. van Veen, B. Nielsen and K.G. Lynn, unpublished, (1988).

Sferlazzo, P., S. Berko, K.F. Canter, Phys. Rev., **B32**, (1985), 6067.

Short, D.W., R.A. Rapp and J.P. Hirth, J. Chem. Phys., **57**, (1972), 1381.

Singh, M., S.Y. Tang, and O.L. Chow, Phys. Rev., **B39**, (1989), 16394.

Soininen, E., H. Huomo, J. Mäkinen, A. Vehanen and P. Hautojarvi, Phys. Rev., **B41**, (1990), 6227.

Sonninen, E., A. Schwab and K.G.Lynn, Phys. Rev. B43, (1991), 10051.

Sueoka, O., and S. Koide, Jap. J. Phys. Soc., 41, (1976), 116.

Sze, S.M., **Physics of Semiconductor Devices**, New York, John Wiley & Sons, Inc., 1981.

Tong, B.Y., Phys. Rev. B5, (1972), 1436.

Tuomisaari, M., R.H. Howell, T. McMullen, Phys. Rev. B40 (1989), 2060

Uedono, A., S. Tanigawa, Y. Ohji, Phys.Lett., 133A, (1988), 82.

Valkealahti, A., and R.M. Nieminen, Appl. Phys., A35, (1984), 51.

Valkealahti,A., Ph.D. Thesis of University of Jyväskylä, unpublished, (1988).

Vehanen, A., K. Saarinen, P. Hautojärvi, and H. Huomo, Phys. Rev. B35, (1987), 4606.

Weiss, A., R. Mayer, M. Jibaly, C. Lei, D. Mehl, K.G. Lynn, Phys. Rev. Lett. 61, (1988), 2245.

Weiss, A., in **Positron Beams for Solids and Surfaces**, AIP Conference Proceedings 218, edited by P.J. Schultz, G.R. Massoumi, P.J. Simpson, American Institute of Physics, New York, 1991.

West, R., Adv. Phys., 22, (1973), 263.

Welton-Cook, M.R., and M. Prutton, Surf. Sci. 64, (1977), 633.

Wilson, R.J., Phys. Rev., B27, (1983), 6974.

Zhigunov, V.P., T.P. Kostkina and A.A. Spiridonov, Nucl. Instr. and Meth., A273, (1988), 362.